

ABSTRACT

Cavity Ring Down and Thermal Lens Techniques Applied to Vibrational Spectroscopy of Gases and Liquids

Parashu Ram Nyaupane, Ph.D.

Mentor: Carlos E. Manzanares, Ph.D.

Infrared (IR) and near-infrared (NIR) region gas temperature sensors have been used in the past because of its non-intrusive character and fast time response. In this dissertation cavity ring down (CRD) absorption of oxygen around the region 760 nm has been used to measure the temperature of flowing air in an open optical cavity. This sensor could be a convenient method for measuring the temperature at the input (cold air) and output (hot air) after cooling the blades of a gas turbine. The results could contribute to improvements in turbine blade cooling designs. Additionally, it could be helpful for high temperature measurement in harsh conditions like flames, boilers, and industrial pyrolysis ovens as well as remote sensing.

We are interested in experiments that simulate the liquid methane and ethane lakes on Titan which is around the temperature of 94 K. Our specific goal is to quantify the solubility of unsaturated hydrocarbons in liquid ethane and methane. However, it is rather complicated to do so because of the low temperatures, low solubility and solvent effects. So, it is wise to do the experiments at higher temperature and test the suitability of the

techniques. In these projects, we were trying to explore if our existing laboratory techniques were sensitive enough to obtain the solubility of unsaturated hydrocarbons in liquid ethane. First, we studied the thermal lens spectroscopy (TLS) of the ($\Delta\nu = 6$) C-H overtone of benzene and naphthalene in hexane and CCl_4 at room temperature.

Cavity Ring Down and Thermal Lens Techniques Applied to Vibrational Spectroscopy of Gases
and Liquids

by

Parashu Ram Nyaupane, M.Sc., B.Sc.

A Dissertation

Approved by the Department of Chemistry and Biochemistry

Patrick Farmer, Ph.D., Chairperson

Submitted to the Graduate Faculty of
Baylor University in Partial Fulfillment of the
Requirements for the Degree
of
Doctor of Philosophy

Approved by the Dissertation Committee

Carlos E. Manzanares, Ph.D., Chairperson

Darrin J. Bellert, Ph.D.

Kevin L. Shuford, Ph.D.

Touradj Solouki, Ph.D.

Lesley M. Wright, Ph.D.

Accepted by the Graduate School

August 2017

J. Larry Lyon, Ph.D., Dean

Copyright © 2017 by Parashu Ram Nyaupane

All rights reserved

TABLE OF CONTENTS

LIST OF FIGURES	VIII
LIST OF TABLES	XII
ACKNOWLEDGMENTS	XIII
DEDICATION.....	XV
CHAPTER ONE	1
1.1 Phase-Shift Cavity Ring Down Spectroscopy (PS-CRDS)	1
1.1.1 Conditions for CRD Signal.....	5
1.1.2 Beer-Lambert Behavior	6
1.1.3 Optical Cavity	6
1.1.4 Cavity Modes	8
1.1.5 Temperature Sensors for Flowing Gas	9
1.1.6 Gas Turbine.....	10
1.1.7 NIR Absorption of Oxygen (the A-band)	12
1.1.8 Molecular Constants of Oxygen for NIR Transition	14
1.1.9 Calculation of Temperature	16
1.2 PS-CRD Spectroscopy of Oxygen in Air as a Temperature Sensor	18
1.2.1 Experimental Setup.....	18
1.2.2 Open Path Optical Cavity	19
1.2.3 Calibration of Thermocouple Sensor	20
1.2.4 Temperature Measurements of Flow air with Sensor	23
1.2.5 Cleaning of Optics	23
1.2.6 Alignment of Pump Laser Beam into a Laser Cavity	24
1.2.7 Alignment of a Laser Beam into an Open Path Cavity.....	24
1.2.8 Phase Shift Angle Measurements	25
1.3 Phase Shift Cavity Ring Down Spectroscopy of Oxygen in Flowing Air.....	27
1.3.1 Validation of the Developed Method with Simulated Result	43
1.3.2 Comparison with other Method	43
1.4 Conclusions and Research Outlook	49
CHAPTER TWO	51
2.1 Thermal Lens Spectroscopy (TLS).....	51
2.1.1 Thermal Lens Effect	51
2.1.2 Thermal Lens Signal.....	52
2.1.3 Laser Beams Configurations on TLS.....	53
2.2 Experimental Method and Procedure	54
2.2.1 Concentric Alignment of the Excitation and Probe Laser Beam.....	57

2.2.2	Complete Blocking of the Excitation Laser	57
2.2.3	Observation of TLS Signal on Oscilloscope	57
2.2.4	Normalization of TLS Signal	58
2.2.5	Signal to Noise Ratio Improvement	58
2.2.6	Acquisition of the Spectra	59
2.2.7	Experimental Shutdown	61
2.3	Thermal Lens Signal of the ($\Delta\nu = 6$) C-H Vibrational Overtone of C ₆ H ₆	61
2.3.1	Solvent Enhancement Factor	65
2.3.2	Comparison of Experimental TLS Signal with Calculated Signal	68
2.3.3	Two Color Excitation Model	72
2.3.4	Electronic Transition of Benzene in Hexane	79
2.3.5	Experiment with 586 nm Probe Laser.....	80
2.4	Thermal Lens Signal of the ($\Delta\nu = 6$) C-H Vibrational Overtone of C ₁₀ H ₈	84
2.5	Conclusion	91
2.6	Optical Saturation in Thermal Lens Spectroscopy	92
2.7	Saturation on TLS of ($\Delta\nu = 6$) C-H Overtone of C ₆ H ₆ , C ₆ H ₅ Cl, C ₆ H ₄ Cl ₂	93
2.8	Conclusions and Research Outlook	105
CHAPTER THREE		106
3.1	C-H Infrared Absorption and Solubility of Hydrocarbons	106
3.1.1	Cryo-spectroscopy and its Importance.....	108
3.2	Fourier Transform Infrared (FTIR) Spectroscopy	109
3.2.1	Spectrophotometer Description	109
3.2.2	Cryostat, Sample Cell and Vacuum Chamber	109
3.2.3	Cryostat Operation	110
3.2.4	Collecting the Data	112
3.2.5	Experimental Shutdown.....	113
3.2.6	Calculation of Mole Fraction.....	113
3.3	C-H Infrared Absorption of 2-methyl-2-butene.....	114
3.4	C-H Infrared Absorption of Propyne	120
3.5	Interpretation of Data with Thermodynamic Frame work	122
3.5.1	PC-SAFT Model	123
3.5.2	Regular Solution Theory.....	125
3.6	Comparison with Literature Study.....	127
3.7	Conclusion	129
APPENDICES		130
APPENDIX A		131
A.1	Remote Control and Data Acquisition Systems.....	131
A.2	Computer Hardware.....	131
A.3	PS-CRD LabVIEW Software Programs	131
A.4	TLS LabVIEW Software Programs	137
A.4.1	Lock-in Amplifier Interface (Get Volts.VI).....	137
A.4.2	Motor Control (Motor Cont.VI).....	138

A.4.3	Spectrum Display (Graph.VI).....	139
A.4.4	Spectrum Acquisition (Main.VI)	140
APPENDIX B		142
B.1	List of Variables.....	142
REFERENCES		145

LIST OF FIGURES

Figure 1. PS-CRD diagram.....	2
Figure 2. PS-CRD signal (top), Reference signal (bottom).....	3
Figure 3. $\tan(\Theta)$ versus Θ graph.....	4
Figure 4. Stable optical cavity with mirror placed $r < d < 2r$	7
Figure 5. Stable optical cavity with mirror placed $0 < d < 2r$	7
Figure 6. Potential energy diagram of O ₂ molecule.....	13
Figure 7. Experimental setup of the CRD spectrometer.....	18
Figure 8. Open-path (no windows) optical cavity.....	20
Figure 9. Calibration of the thermocouple sensor for the experimental temperature determination	22
Figure 10. Reference phase shift angle measurement.....	25
Figure 11. The A-band of oxygen in static air with designation of the ^P P branch at 298 K	28
Figure 12. Flow series of the A-band of oxygen in air at 298 K	30
Figure 13. Boltzmann plot of the ^P P branch of the A-band of oxygen in flow air at 298 K	32
Figure 14. Flow series of the A-band of oxygen at 321 K.....	34
Figure 15. Boltzmann plot of the ^P P branch of the A-band of oxygen in flow air at 321 K	36
Figure 16. Flow series of the A-band of oxygen at 359 K.....	38
Figure 17. Boltzmann plot of the ^P P branch of the A-band of oxygen in flow air at 359 K	40
Figure 18. PGOPHER simulated spectrum of the A-band of oxygen at 298 K.....	44

Figure 19. Boltzmann plot of the P^P branch of a simulated A-band of oxygen at 298 K	45
Figure 20. Plot of the ratio of intensity of P17 and P2 transitions of the A-band of oxygen versus temperatures	47
Figure 21. Plot of ratio of the integrated area of the P17 and P2 transitions of the A-band of oxygen versus temperatures	48
Figure 22. Formation of the thermal lens in the sample	52
Figure 23. Pump and probe beam configuration on mode -mismatched dual beam TLS technique	54
Figure 24. Experimental setup of the thermal lens spectrometer.....	56
Figure 25. T L spectra of the C-H overtone ($\Delta\nu = 6$) of benzene solutions In CCl_4 with various compositions by volume at 295 K	63
Figure 26. TL spectra of the C-H vibrational overtone ($\Delta\nu = 6$) of benzene solutions in $n-C_6H_{14}$ with various compositions by volume at 295 K	64
Figure 27. Numerical calculation of the solvent enhancement factor (g) as a function of the composition of benzene (x_2) in $n-C_6H_{14}$ and CCl_4	67
Figure 28. Comparison of predicted thermal lens signal with the experimental thermal lens signal as a function of the composition of benzene in CCl_4	71
Figure 29. Normalized experimental thermal lens signal as a function of composition of benzene in $n-C_6H_{14}$ at 295 K.....	75
Figure 30. Normalized experimental thermal lens signal as a function of low composition of benzene in $n-C_6H_{14}$ at 295 K.....	76
Figure 31. Normalized experimental thermal lens signal as a function of composition of benzene in CCl_4 at 295 K.....	77
Figure 32. Normalized experimental thermal lens signal as a function of low composition of benzene in CCl_4 at 295 K.....	78
Figure 33. Ultraviolet spectrum of the secondary band of benzene in $n-C_6H_{14}$	79
Figure 34. Concentration series of the TLS signal of the fifth ($\Delta\nu = 6$) C-H overtone of benzene in $n-C_6H_{14}$ with 568 nm probe laser	81

Figure 35. Comparison of normalized TLS signal of the fifth ($\Delta\nu = 6$) C-H overtone transition of benzene with two different probe lasers as a function of the composition by volume in C_6H_6 - n - C_6H_{14} solutions	83
Figure 36. Thermal lens spectra of the C-H vibrational overtone ($\Delta\nu = 6$) of naphthalene solutions in n - C_6H_{14} with 488 nm probe laser.....	85
Figure 37. Thermal lens spectra of the C-H vibrational overtone ($\Delta\nu = 6$) of naphthalene solutions in n - C_6H_{14} at 295 K with 568 nm probe laser	86
Figure 38. Comparison of normalized TLS signal of the fifth ($\Delta\nu = 6$) C-H overtone transition of naphthalene with two different probe lasers as a function of the concentration of in $C_{10}H_8$ - n - C_6H_{14} solutions at 295 K.....	89
Figure 39. Ultraviolet spectrum of the naphthalene (210-350 nm) in n - C_6H_{14}	90
Figure 40. Thermal lens signal of ($\Delta\nu = 6$) C-H overtone spectrum of chlorobenzene at various pump power at 295 K	94
Figure 41. Thermal lens signal of ($\Delta\nu = 6$) C-H overtone spectrum of O-dichlorobenzene at various pump power at 295 K	95
Figure 42. Pump power versus maximum absorbance value on TLS signal of ($\Delta\nu = 6$) overtone transition of chlorobenzene at 298 K	97
Figure 43. Pump power versus maximum absorbance value on TLS signal of ($\Delta\nu = 6$) overtone transition of O-dichlorobenzene at 298 K	98
Figure 44. Optical saturation on TLS spectrum of ($\Delta\nu = 6$) C-H overtone transition of benzene with various excitation laser powers	100
Figure 45. Various degree of optical saturation on TLS spectrum of ($\Delta\nu = 6$) C-H overtone transition of chlorobenzene with various excitation laser powers ..	101
Figure 46. Plot of height of the Lamb dip on saturated TLS spectrum of ($\Delta\nu = 6$) C-H overtone transition of benzene versus excitation laser power.....	103
Figure 47. Plot of height of the Lamb dip on saturated TLS spectrum of ($\Delta\nu = 6$) C-H overtone transition of chlorobenzene versus excitation laser power	104
Figure 48. Schematics of the cryostat, sample cell and vacuum chamber used in FT experiments	111
Figure 49. Pressure series of spectral band of C-H fundamental transition of 2-methyl-2-butene in gas phase at 298 K	115

Figure 50. Plot of integrated area of spectral band of C-H fundamental transition of 2-methyl-2-butene versus pressure at 298 K.....	116
Figure 51. Concentration series of spectral band of C-H fundamental transition of 2- methyl-2-butene solutions in liquefied argon at 100 K.....	118
Figure 52. Plot of integrated absorbance of spectral band of C-H fundamental transition of 2-methyl-2-butene solution in liquefied argon versus mole fraction (ppm) at 100 K	119
Figure 53. Concentration series of spectral band of C-H fundamental transition of methyl-acetylene solutions in liquefied argon at 100 K	121
Figure 54. Plot of integrated absorbance of spectral band of C-H fundamental transition of methyl acetylene solution in liquefied argon versus mole fraction (ppm) at 100 K.....	122
Figure A.1 Measurement panel wiring diagram	133
Figure A.2 DAQ movement of the motor VI.....	133
Figure A.3 Delay time VI	134
Figure A.4 Pscrd 830 Snap VI	135
Figure A.5 Pscrd 830 Asking data VI.....	135
Figure A.6 Acquire data point and calculated absorption VI	136
Figure A.7 Stop data collection VI	136
Figure A.8 TLS writing data VI.....	137
Figure A.9 TLS Reading data VI.....	138
Figure A.10 TLS motor control VI	138
Figure A.11 Graph VI.....	139
Figure A.12 Spectra acquisition main VI	140
Figure A.13 Pause time VI.....	141
Figure A.14 Global display VI.....	141

LIST OF TABLES

Table 1. Mode spacing calculations.....	8
Table 2. Vibrational and rotational constants for ($X^3\Sigma_g^-$) and ($b^1\Sigma_g^+$) of oxygen	15
Table 3. Molecular constants of oxygen ($X^3\Sigma_g^- v'' = 0$)	15
Table 4. Data for the calibration of thermocouple sensor.....	21
Table 5. Parameters for the optimization of CRD signal.....	26
Table 6. Relative intensity and energy of the P^3P branch of the A- band of oxygen in flow air at 298 K	31
Table 7. Relative intensity and energy of the P^3P branch of the A- band of oxygen in flow air at 321 K	35
Table 8. Relative intensity and energy of the P^3P branch of the A- band of oxygen in flow air at 359 K	39
Table 9. Accuracy of temperature sensor	42
Table 10. Ratio of the intensity/integrated area of P17 and P2 transitions of the A-band of oxygen at various temperatures.....	46
Table 11. Parameters for optimization of TLS signal.....	60
Table 12. Thermo-physical property of liquid C ₆ H ₆ , CCl ₄ , and n-C ₆ H ₁₄ at 295 K.....	68
Table 13. Integrated area of the TLS signal of the fifth ($\Delta\nu = 6$) C-H overtone of benzene in CCl ₄	69
Table 14. Integrated area of the TLS signal of the fifth ($\Delta\nu = 6$) C-H overtone of benzene in n-C ₆ H ₁₄	70
Table 15. Integrated area of the TLS signal of the fifth ($\Delta\nu = 6$) C-H overtone of benzene in n-C ₆ H ₁₄ with 568 nm probe laser.....	82
Table 16. Integrated area of the TLS signal of the fifth ($\Delta\nu = 6$) C-H overtone transition of naphthalene solutions in n-C ₆ H ₁₄ with 488 nm probe laser	87

Table 17. Integrated area of the TLS signal of the fifth ($\Delta\nu = 6$) C-H overtone transition of naphthalene solutions in n-C ₆ H ₁₄ with 568 nm probe laser	88
Table 18. Thermal lens signal amplitude at the region of maximum absorption of chlorobenzene at several pump powers.....	96
Table 19. Thermal lens signal amplitude at the region of maximum absorption of O-dichlorobenzene at several pump powers	96
Table 20. Height and width of Lamb dip on various degree of saturated TLS signal of pure benzene.....	99
Table 21. Height and width of Lamb dip on various degree of saturated TLS signal of chlorobenzene.....	102
Table 22. Combination of instrumental parameters for FTIR Spectrometer	109
Table 23. Integrated area of absorbance of spectral band of C-H fundamental transition of 2-methyl-2-butene at 298 K	116
Table 24. Integrated area of absorbance of spectral band of C-H fundamental transition of 2-methyl-2-butene solutions in liquefied argon at 100 K	119
Table 25. Integrated area of absorbance of spectral band of C-H fundamental transition of methyl-acetylene solutions in liquefied argon at 100 K	120
Table 26. Individual PC-SAFT parameters of compounds.....	124
Table 27. Individual PC-SAFT parameters and derived interaction parameters from experimental solubility at 100 K	124
Table 28. Molar volumes (V_i) and solubility parameters (δ_i)	126
Table 29. Interaction parameters (l_{12}) calculated from experimental solubility	127
Table 30. Experimental solubilities of the unsaturated hydrocarbons in cryogenic liquid	128

ACKNOWLEDGMENTS

I would like to express my deepest gratitude to my mentor, Dr. Carlos E. Manzanares, for his unwavering support, encouragement and mentorship throughout this journey. I could not imagine this odyssey without his guidance and persistent help.

I am grateful to my committee members: Dr. Darrin J. Bellert, Dr. Kevin L. Shuford, Dr. Touradj Solouki, and Lesley M. Wright for their valuable insights and suggestions on my work. Special thanks to Dr. Bellert for his encouragement and suggestions during my entire graduate school period. He would always be seen as a second mentor to me. Also, special thanks to Dr. Shuford for his undaunting support and encouragement, not only for my graduate school challenges but also my job-hunting hurdles.

I would like to thank our Graduate Program Director, Dr. Charles M. Garner, for helping me adapt as a member of the Baylor Graduate family. I really appreciate him for being there always. Special thanks to my previous and current research group members: Dr. David Camejo, Marlon Diaz, Ann Barton and Ashley Diaz for their support. Also, I would like to acknowledge Chris Jaska for his help in laser technicalities.

Finally, this accomplishment would not be possible without the financial support I enjoyed from the Chemistry and Biochemistry Department, chaired by Dr. Patrick Farmer. Also, I would like to thank Baylor Graduate School for financial support and several travel awards. Additionally, I would like to acknowledge the Robert A. Welch Foundation for funding my research.

DEDICATION

To my entire family, especially my maternal grandmother. Grand ma you are the one who advocated for a better education and breaking the traditional way of learning.

CHAPTER ONE

1.1 Phase Shift Cavity Ring Down Spectroscopy (PS-CRDS)

Cavity ring down (CRD) spectroscopy is a highly sensitive laser absorption technique in which an optical path length can be achieved in the range of 1-100 km. It comprises of a laser source, an optical cavity, and a detector to measure the light from the optical cavity. There are two main ways of doing cavity ring down spectroscopy. It can be performed with pulsed or continuous light sources. The sensitivity of the technique does not depend on the intensity of the light. The pioneers of the CRD technique are Herbelin et al and Anderson et al. [1-3]. They measured the reflectivity of the surface of a mirror by measuring the time spent by the laser beam inside the optical cavity while it goes in the back and forth process. The ring down time was measured with a phase shift angle measurement [2]. In 1984, Anderson et al. [3] measured the reflectivity of a mirror by looking at the exponential decay of intensity of light. The CRD spectroscopy has been applied mostly to gas samples but can be applied to liquid samples [4-8]. It has been used in various environmental studies like plasma chemistry [9-14], supersonic expansion [15-18], kinetic study for transient species, radicals [19-24], molecular ions [25,26] and very weak vibrational overtone studies [27-29]. Additionally, it has been used in analytical applications such as trace gas detection [30-34], water pollution [35], aerosol pollutants [36,37].

The two most common detection methods in CRD spectroscopy are exponential and phase shift (PS) method. In this project, we only discuss the principle behind the phase shift cavity ring down (PS-CRD) technique. This technique was used by Engeln et al. [38]

with continuous wave lasers in 1996 to measure the absorption of O₂. In this technique, the lifetime of a photon from a continuous wave laser in a high-finesse optical cavity is determined by measuring the phase-shift angle between the modulated input and output light that passes through the optical cavity. The phase shift angle is related to the ring down time by the equation [39].

$$\tan\theta = 2\pi f \tau \quad (1)$$

Where, θ is the phase shift angle, f is the modulated frequency, and τ is the ring down time. In Figure 1, a modulated beam from continuous wave (CW) tunable laser is injected in the optical cavity [40].

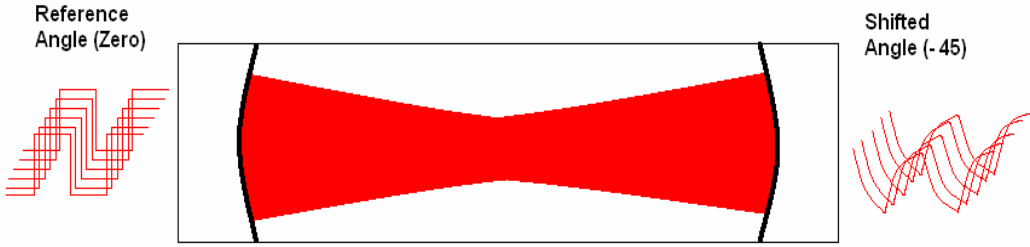


Figure 1. PS-CRD diagram

An electro-optic modulator is used to create a square modulation frequency shape. The laser emerging out of the cavity produces an “on/off” pattern that translates into a filling/emptying of the cavity [40]. This resembles a shark fin. In this phenomenon, the positive slope is interpreted as building up the light inside the cavity, and the negative slope indicates light leaking out of the cavity. The phase shift angle (θ) is monitored on the negative slope of the exiting wave. Figure 2 shows a diagram of the phase shift, with the square reference signal entering to the cavity (bottom) and phase shift signal detected after the beam traverses the cavity (top).

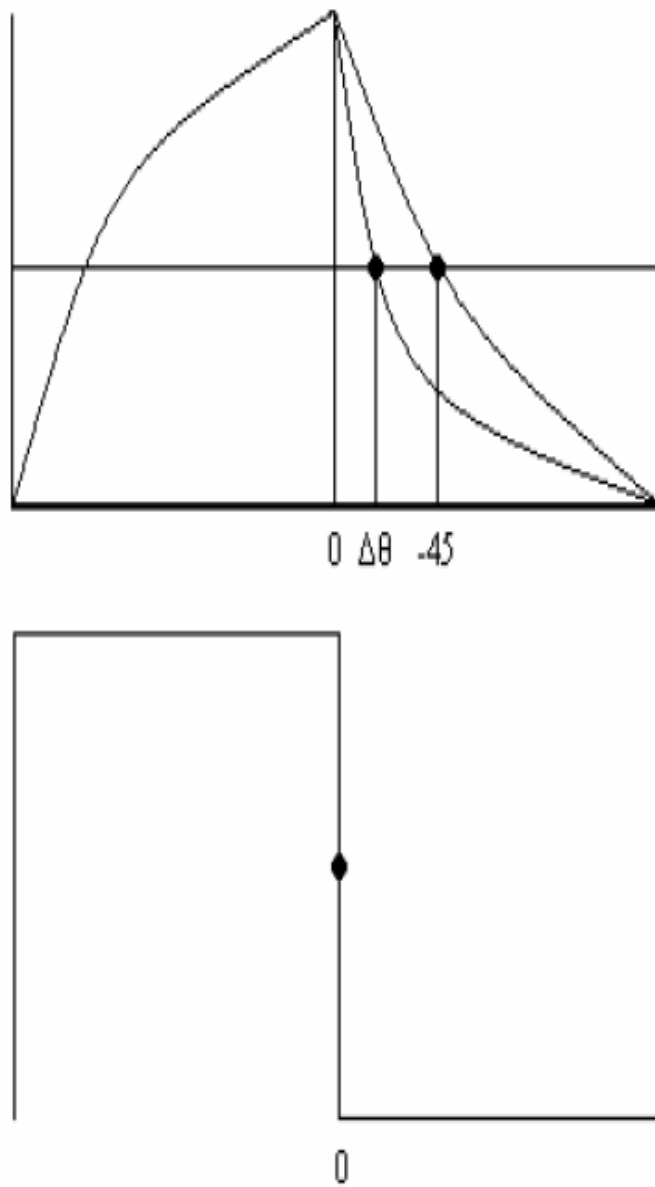


Figure 2. PS-CRD signal (top), Reference signal (bottom)

The cavity is aligned to get the PS-CRD signal with a phase shift angle of -45° when the cavity is empty. The $\tan\theta$ function is shown in Figure 3. In the graph, the boxed area shows fair linearity from -45° to 0 degrees. The angles greater than -45° are avoided because of the non-linear response of the function at other angles.

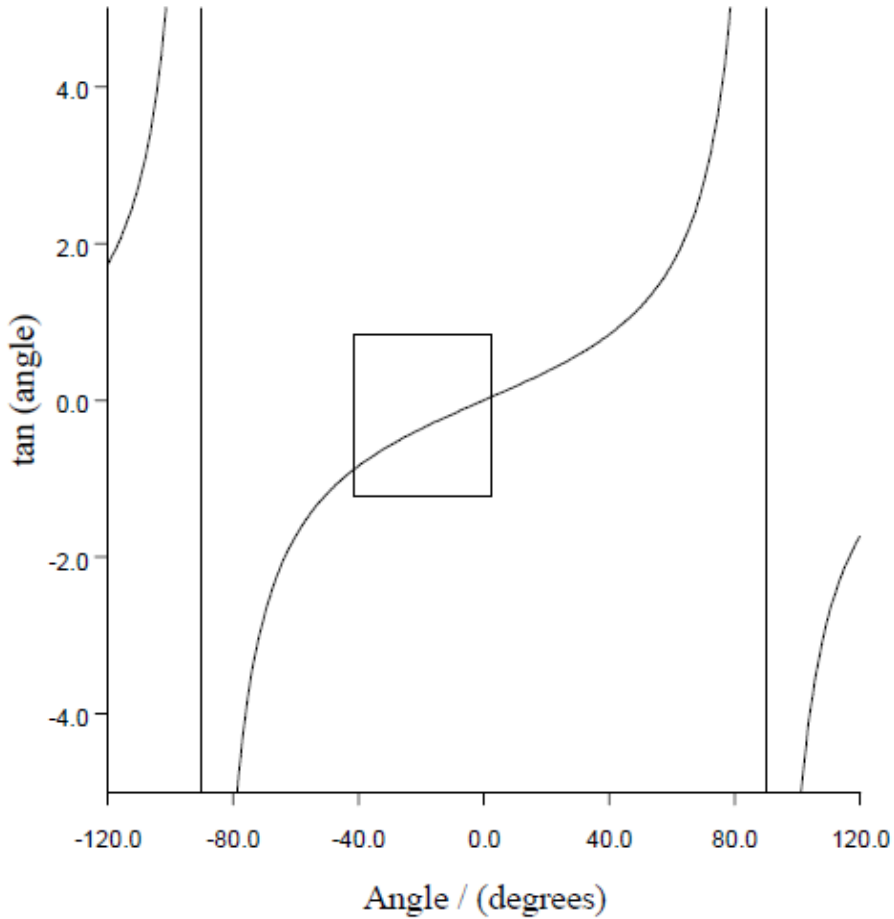


Figure 3. $\tan(\theta)$ vs Θ graph

The optical path length inside the cavity is determined from the product ($\tau \times c$) of ring down time τ and speed of light c . In our case, for most of the experiments, the optical path length was approximately 3.9 km, with a decay time constant being around $13 \mu\text{s}$. The decay time of an empty cavity (τ_0) that is a function of the wavenumber (σ) is related to the distance between the mirrors and their reflectivity by the equation:

$$\frac{1}{\tau_0(\sigma)} = \frac{c(1-R)}{L} \quad (2)$$

where L is the distance between the two mirrors, c is the speed of light, and R is the reflectivity of the mirrors. Similarly, the decay time of a cavity filled with the sample is given by the equation:

$$\frac{1}{\tau(\sigma)} = c \left[\frac{(1-R)}{L} + \alpha(\sigma) \right] \quad (3)$$

where $\alpha(\sigma)$ is the absorption coefficient of the sample as a function of the wavenumber. The absorption of the sample is calculated by the subtraction of inverse of the decay time of empty cavity ($1/\tau_0$) from the inverse of the decay time of the cavity filled with the sample ($1/\tau$). Equation 4 represents the absorption signal of the sample in an optical cavity.

$$\alpha(\sigma) = \frac{1}{c} \left[\left(\frac{1}{\tau(\sigma)} \right) - \left(\frac{1}{\tau_0(\sigma)} \right) \right] \quad (4)$$

Similarly, the observed signal for an open cavity is [39]:

$$\frac{1}{c\tau(\sigma)} = \alpha(\sigma) + \frac{1-R}{L} + \alpha_{scatt} \quad (5)$$

The absorption $\left(\frac{1}{c\tau(\sigma)} \right)$ includes background cavity losses that, in this case, are represented by the reflectivity of the mirrors (R) and presence of air (α_{scatt}). For an open cavity, the reflectivity of the mirrors and the scattering of the light only affect the absorption baseline. The measured absorption is plotted as a function of wavenumber (cm^{-1}) to obtain the absorption spectrum of the sample.

1.1.1 Conditions for CRD Signal

To obtain the CRD signal with high optical path length, some conditions are needed to be met. One of the necessary conditions is that the Beer–Lambert behavior should be followed for a single pass of light through the cavity. Also, the interference effects between the longitudinal and transverse modes of the cavity must be minimized.

1.1.2 Beer-Lambert Behavior

In order to follow the Beer-Lambert behavior, the widths of the absorption spectral lines have to be greater than the linewidth of the laser within the cavity. In that case, when the laser is tuned to the central frequency of the absorption line, all the frequencies contained within the laser are attenuated only by absorption [41].

1.1.3 Optical Cavity

The second important condition required for CRD signal is stable and non-focal optical cavity. An optical cavity with two mirrors is considered geometrically stable when the light is refocused within the cavity after successive reflections from highly reflective mirrors. During reflection, optical energy is contained or trapped within the cavity. The stable optical cavity formation depends upon the g-parameters of the mirror and optical cavity. [42]. Specifically,

$$0 \leq g_1 g_2 \leq 1 \quad (6)$$

where g_1 and g_2 are defined as:

$$g_1 = \left(1 - \frac{L}{r_1}\right) \quad (7)$$

$$g_2 = \left(1 - \frac{L}{r_2}\right) \quad (8)$$

where L is the distance between the two mirrors and r_1 and r_2 are the radii of curvatures of the mirrors. The non-confocal cavity system introduces some mechanical flexibility on the alignment of mirrors in the cavity. Because of this property, the mirrors can move slightly while retaining a proper alignment with respect to each other. However, if the mirrors are positioned at each other's focal length, any mechanical disturbance can result in a loss of the alignment. This approach can be defined by using the following relationship:

$$r < d < 2r \quad (9)$$

$$0 < d < 2r \quad (10)$$

where, d is the distance between the mirrors and r is equal to their radius of curvature, assuming $r = r_1 = r_2$. Figures 4 and 5 show two different configurations for a stable optical cavity system with mirrors placed inside and outside the radius of curvatures respectively. The cavity mode can be made very dense, especially when the d/r ratio is chosen to be an irrational number [38].

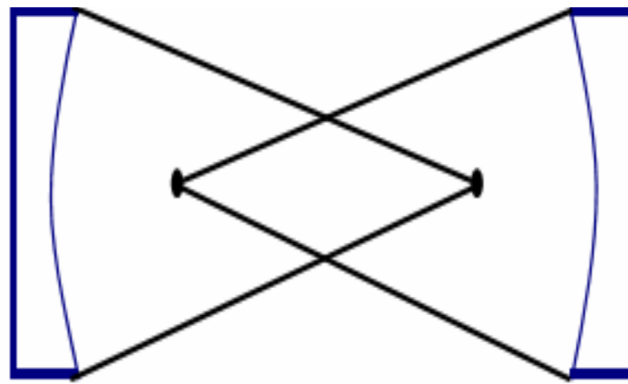


Figure 4. Stable optical cavity with mirror placed $r < d < 2r$

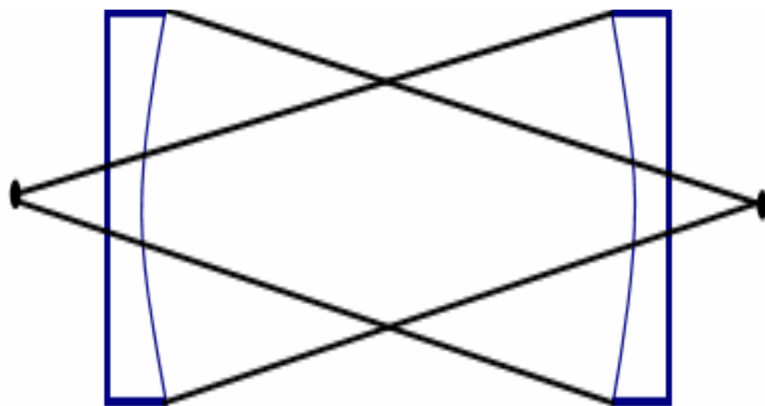


Figure 5. Stable optical cavity with mirror placed $0 < d < 2r$

1.1.4 Cavity Modes

Another important condition that must be considered for CRD is the structure of optical cavity otherwise it might cause several problems. When laser light is injected into an optical cavity, different modes of light are formed. Longitudinal or axial modes determine the resonant oscillation frequencies that satisfy the wavelength requirements of the cavity along a given optical path [42]. The longitudinal mode frequencies within an optical system are important considerations for a continuous scanning system like a CRD instrument. If the frequency spacing of the longitudinal modes of the cavity (the cavity free spectral range, FSR) exceeds the width of the spectral features being studied, then the light of the appropriate frequency for excitation of certain spectral lines will not be injected into the cavity and thus the absorption features will be absent from the resultant spectrum. The comparison of the mode spacing with laser line width determines how an optical cavity will respond to a scanning CRD system [43,44]. The frequency spacing ($\Delta\nu$) of longitudinal cavity modes (FSR) is defined as:

$$\Delta\nu = \frac{c}{2L} \quad (11)$$

Where, c and L are the speed of the light and length of the cavity, respectively. Table 1 presents the laser resolutions versus longitudinal mode spacing.

Table 1. Mode Spacing Calculations

Cell length(cm)	Ti: Sapphire Resolution (cm ⁻¹)	Longitudinal Mode Spacing (MHz)	Longitudinal Mode Spacing (cm ⁻¹)
43.5	0.17	345	0.0115

As shown in the table, the mode spacing is much smaller than our laser resolution, which provides an overlapping multi-mode configuration. This is the reason why we can make continuous scanning possible.

1.1.5 Temperature Sensor for Flowing Gas

The accurate measurement of the temperature of air or any flowing gas is challenging and complicated [45]. Its measurement in harsh environments like firing chambers of boilers, combustion chambers of various engines, and other industrial devices is of great practical importance for a variety of needs and applications [46]. In order to meet these needs, the industry has developed a large number of sensors and devices such as thermometers, thermocouples, chemical, thermodynamic and optical methods for various tasks based on the precision required and the error allowed [47, 48]. In recent years, high temperatures have been acquired by gas temperature sensors based on absorption spectroscopic techniques [49]. Such techniques offer significant opportunities and advantages for the evaluation of various flow field parameters such as temperature, pressure, velocity and density because of their high sensitivity, high spectral resolution, fast time response, robustness and non-intrusive character [50]. There are various literature reports on temperature measurements of the exhaust gases from combustion and other industrial processes [49]. Literature review indicated that most research was initially limited to the ultraviolet (UV) range. Some researchers have determined the gas temperature from the measurement of two wavelength UV absorptions [51-53]. A. Fateev and S. Clausen [54] evaluated the flowing gas temperature from the absorption band of the NO ($A\ ^2\Sigma^+ \leftarrow X\ ^2\Pi$) in the 211-238 nm spectral range. J. B. Jeffries et al. used UV absorption of CO₂ for the temperature diagnostics of hydrocarbon combustion [55].

Due to revolutionary development of lasers and optics, gas temperature sensors now extend to the near and mid-IR regions. Fourier transform infrared spectroscopy (FTIR) [56-58], laser induced fluorescence (LIF) [59, 60], intra cavity laser Induced spectroscopy (ICLAS) [61], and cavity ring down spectroscopy (CRDS) [62] are commonly used techniques in the IR region. In order to evaluate the temperature, the spectroscopic data of simple gaseous molecules like CO [63], CO₂ [64] H₂O vapor [65, 66], O₂ [67], N₂ [68] and radicals such as OH [62], CH [69], NH₂ [70] have been used. These molecules are desirable since they are possible products in the flame, combustion chambers, or exhaust gases of the various types of engines. Recently, T. Werblinski and his coworkers measured the temperature profile of a flame by using the time-domain-based super continuum absorption spectroscopic technique [71]. They measured the broadband H₂O absorption in the spectral range 1340-1485 nm and compared it with the simulated spectrum to get the temperature of a flame. More recently, A. Fomin et al [72] reported a Fiber Laser Intracavity Absorption Spectroscopy (FLICAS) method for the simultaneous measurement of CO and CO₂ concentrations and temperature in the flow system.

However, there is little information in the literature on the determination of temperatures involving flowing air near the blades of gas turbines; this consideration is of prime importance for blade cooling technology.

1.1.6 Gas Turbine

Gas turbines are a type of internal combustion engine that increase the efficiency in power generation using fossil fuels. Gas turbines have been the primary engines for aircraft propulsion for decades. They are also quickly becoming the engine of choice for electrical power generation, because of the increased thermal efficiency of the engine. They

have direct impact on industrialized societies around the world. The power production of these engines can increase directly by increasing the operating temperature. So far, the operating temperature of the turbine rises up to 2000 K; however, the turbine blades and vanes are not able to bear such a high temperature. In order to avoid melting of the blades and vanes under the extreme heat loads, different blade cooling technologies have been used such as film cooling. In this method, the thin film of cooling air flows through the blades and vanes of the turbine [73,74], which helps to keep the blades and vanes cool and prevent them from melting. When implementing advanced cooling technology into the turbine blades and vanes, it is necessary to have an accurate prediction of the coolant to mainstream flow interaction around the airfoils; if the predicted metal temperature is off by only 30 K the life of the component is reduced by half. Therefore, engine designers require accurate and highly resolved temperature measurements of both the airfoil wall and the air temperature surrounding the blades and vanes. This coolant to mainstream interaction is modeled in the laboratory to match non-dimensional blowing ratios and density ratios with the actual engines. By measuring the temperature of the cooling air before and after its interaction with the blades, an initial knowledge of the heat transfer and blade temperature will be developed. This will lead to a more fundamental understanding of how these flows mix in highly turbulent environments. These measurements are usually coupled with parallel experiments such as surface temperature measurements and velocity distributions within the flow to fully characterize mass, momentum, and energy transport in highly turbulent flows [75-78].

With these considerations in mind, we decided to use the absorption of oxygen molecule to measure the temperature of flowing air passing through a glass tube inside an

optical cavity. The temperature is obtained from the NIR absorption of oxygen (the A-band) using the phase shift cavity ring down (PS-CRD) technique. In the future, the same method (if successful) could be used to measure the temperature of the cooling air before and after its interaction with the blades in a small laboratory turbine.

1.1.7 NIR Absorption of Oxygen (the A-band ($0 \leftarrow 0$) Transition)

Molecular oxygen is a paramagnetic molecule with an even number of electrons [79]. According to Mulliken the ground electronic state is $X^3\Sigma_g^-$. The lowest energy singlet excited states $^1\Delta_g$ and $^1\Sigma_g$ lie at 7882 cm^{-1} and 13121 cm^{-1} respectively above the ground state [80]. Figure 6 shows a potential energy diagram of two low-lying electronic states of O₂ molecule. The transitions from the ground state to these excited states are electric dipole and spin forbidden transitions.

However, very weak transitions occur due to a change in the magnetic dipole moment. The three different transitions from the ground state to the second singlet state ($b^1\Sigma_g^+ \leftarrow X^3\Sigma_g^-$) are ($0 \leftarrow 0$), ($1 \leftarrow 0$) and ($2 \leftarrow 0$) transitions which are called A, B and γ -bands of O₂ respectively [81]. These transitions are responsible for the red atmospheric bands of oxygen. According to the Frank Condon principle the intensity of these transitions decrease in the order from $A > B > \gamma$ -bands.

The rotational quantum numbers for the ground state ($X^3\Sigma_g^-$) are designated as the rotational angular momentum (N) and the total angular momentum (J) that is the sum of the rotational (N) and spin (S) angular momentum. The ground state is split into three levels corresponding to $J''=N'', N''+1$, and $N''-1$ with only odd values of N'' are allowed.

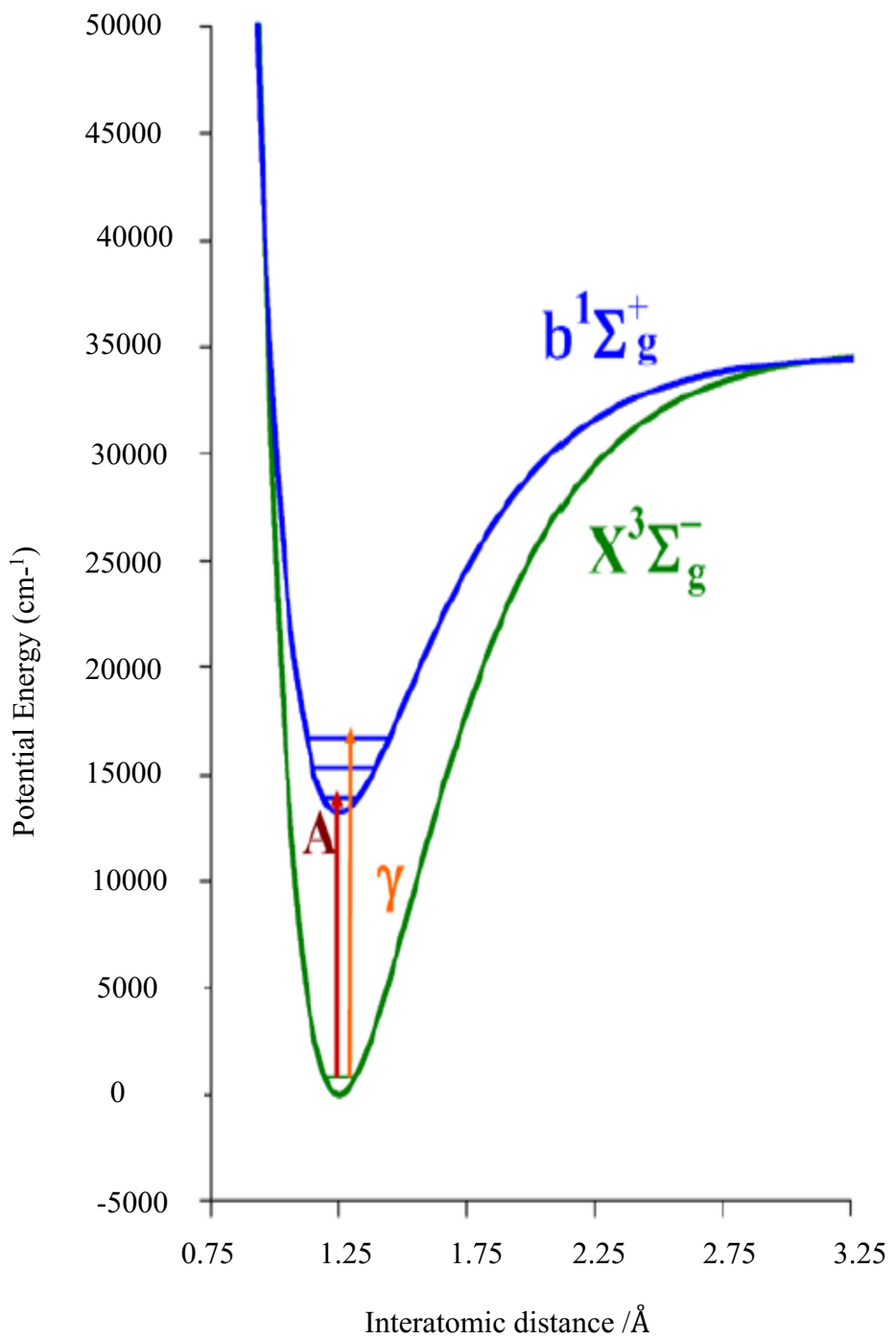


Figure 6. Potential energy diagram of O_2

The upper electronic state ($b\ ^1\Sigma_g^+$) which has zero spin, is composed of single states with $J' = K'$, where only even values of N' are allowed. The transition from ground state to excited state results in four different branches i.e. ${}^P P$ ($\Delta J = -1, \Delta N = -1$), ${}^R R$ ($\Delta J = 1, \Delta N = +1$), ${}^P Q$ ($\Delta J = 0, \Delta N = -1$) and ${}^R Q$ ($\Delta J = 0, \Delta N = +1$).

There are several reasons why we decided to use the oxygen absorption to measure the temperature of flowing air: (1) oxygen is uniformly distributed in the atmosphere with a known mixing ratio, (2) the A- transition is very weak and as a result, there is no chance of saturation effect for a long path length, (3) the spectral window is largely free from the other molecular spectral interferences and (4) it is sensitive to the temperature changes.

In our laboratory, the CRD technique at low and high temperatures has been developed to measure very weak absorptions of molecules relevant to planetary atmospheres [82, 83]. We are able to perform experiments at temperatures at 77 K to 2000 K. In this particular experiment we are mainly focused on temperatures in the range from 298 K to 373 K because this is the range of temperatures covered by the small laboratory turbine. More recently, we have constructed an open-path cell inside a furnace to cover temperature up to 1873 K.

1.1.8 Molecular Constants of Oxygen for the A-band Transition

There have been several literature studies on the A- band of oxygen [49,66,67] and its molecular constants have been reported. Table 2 presents some of the molecular constants like spin-orbit coupling (H), spin – spin coupling (λ) and spin-rotation constant (γ) for the ground state ($X\ ^3\Sigma_g^-$, $v = 0$). The vibrational and rotational constants for ($X\ ^3\Sigma_g^-$) and excited ($b\ ^1\Sigma_g^+$) electronic states of oxygen are also presented on Table 3.

Table 2. Molecular Constants of Oxygen ($X^3\Sigma_g^-$, $v'' = 0$)

Constants	cm^{-1}
H_o	1.2675×10^{-12}
λ_D	1.9661×10^{-6}
λ_H	1.0441×10^{-11}
γ_D	-8.1790×10^{-9}
γ_H	-5.237×10^{-14}

For the transition ($b^1\Sigma_g^+ \leftarrow X^3\Sigma_g^-$), the band origin can be calculated by using following equation:

$$E(v) = T_e + \omega_e (v+1/2) - \omega_e \chi_e (v+1/2)^2 + \omega_e \gamma_e (v+1/2)^3 + \omega_e z_e (v+1/2)^4 \quad (12)$$

Where, T_e , is the electronic energy, ω_e is harmonic frequency, χ_e , γ_e , z_e are the anharmonicities and v is vibrational quantum number.

Table 3. Vibrational and Rotational Constants for ($X^3\Sigma_g^-$) and ($b^1\Sigma_g^+$) of Oxygen

State	T_e	ω_e	$\omega_e \chi_e$	$\omega_e \gamma_e$	B_e	α_e	D_e	Transit
$X^3\Sigma_g^-$	0	1580.19	11.98	0.047	1.4377	0.0159	4.839×10^{-6}	
$b^1\Sigma_g^+$	13195.1	1432.77	10.00	----	1.40037	0.01820	5.351×10^{-6}	$b \leftrightarrow X$

For $(b \ ^1\Sigma_g^+)$ $v' = 0$, $E(0) = 13907.98 \text{ cm}^{-1}$ and for $(X \ ^3\Sigma_g^-)$ $v'' = 0$, $E(0) = 787.11 \text{ cm}^{-1}$. The band origin for this transition $b \ ^1\Sigma_g^+(v' = 0) - X \ ^3\Sigma_g^-(v'' = 0)$ is then $13907.98 - 787.11 = 13120.87 \text{ cm}^{-1}$. A similar process is required for the rotational constant; B_v and the centrifugal distortion constant, D_v . The equations are similar:

$$B_v = B_e - \alpha_e(v + 1/2) + \gamma_e(v + 1/2)^2 + \dots \quad (13)$$

$$D_v = D_e - \beta_e(v + 1/2) + \dots \quad (14)$$

Where α_e , γ_e , β_e are vibrational constants. For $(b \ ^1\Sigma_g^+)$ $v' = 0$, $B_0 = 1.39127 \text{ cm}^{-1}$ and $D_0 = D_e = 5.351 \times 10^{-6} \text{ cm}^{-1}$.

1.1.9 Calculation of Temperature from A-band of Oxygen

In this experiment, the temperature of the flowing air was calculated by measuring the rotational temperature of the O_2 molecule. As with other diatomic molecules, molecular temperature for O_2 can be determined by using the frequency at peak absorption and rotational line intensities of the A-band. The intensity of a rotational transition at a given temperature is given by an equation [79]:

$$I_{\text{abs}} = \frac{C_{\text{abs}} * \sigma}{Q_r} (J' + J'' + 1) e^{-B'' J'' (J'' + 1) hc/kT} \quad (15)$$

Where, I_{abs} is the absorption intensity, σ is the frequency at peak absorption, Q_r is the rotational partition function, C_{abs} is a constant depending on the change of the dipole moment and the total population of the molecules in the initial vibrational level, B'' is the rotational constant of ground state of the transition, k is the Boltzmann constant, and J'' and J' are the rotational quantum numbers in the lower and upper states respectively. The rearrangement of an equation 15 leads to an equation that reproduces the temperature is [79]:

$$\ln \left(\frac{I_{\text{abs}}}{(\sigma * (J' + J'' + 1))} \right) = \ln \left(\frac{C_{\text{abs}}}{Q_r} \right) - \frac{F_{J''}}{kT} \quad (16)$$

Where, the factor $\frac{C_{\text{abs}}}{Q_r}$ is nearly constant. The rotational temperature is calculated from the slope of the natural logarithm of the absorption intensity for each ${}^P P$ branch versus the energy of lower state ($F_{J''}$) which is given by the equation [79]:

$$F_{J''} = B'' J'' (J'' + 1) + 2\lambda - \gamma \quad (17)$$

where, rotational constant of ground state $B'' = 1.4377 \text{ cm}^{-1}$, $\lambda = 1.984 \text{ cm}^{-1}$ is the spin-spin coupling, $\gamma = -0.084 \text{ cm}^{-1}$ is the spin-rotation interaction constant.

To obtain the relative intensity of the rotational branches of the A-band of oxygen, a base line correction of the spectrum was made with OMNIC (Thermo Scientific software available in the FT-IR spectrophotometer as an interface) and followed by normalization of the signal. The normalization is carried out by dividing the absorption values for all the points with the maximum value of absorption which results in a spectrum with an absorbance value range from zero to one unit of magnitude.

Once the signal is normalized, the relative intensity of the rotational branches of the spectrum is obtained. Here the focus is only on ${}^P P$ branches of the spectrum but not on R branches. The reason behind it is that the R branch is not resolved in our spectra. The Boltzmann plot of $\ln \left(\frac{I_{\text{abs}}}{(\sigma * (J' + J'' + 1))} \right)$ versus $F_{J''}$ (Eq. 16) is linear with a slope $-\frac{1}{kT}$ and has a unit of cm. The temperature is calculated by taking the inverse of the slope and multiplying by $1.43879 \text{ K/cm}^{-1}$.

1.2 Phase Shift Cavity Ring Down Spectroscopy (PS-CRDS) as a Temperature Sensor

1.2.1 Experimental Setup

The experimental setup for the optical temperature sensor is depicted in Figure 7. A Ti-Sapphire laser (Coherent 899 ring laser) is pumped by a solid state, frequency doubled Neodymium-Yttrium vanadium oxide (Nd-YVO₄) laser (Coherent Verdi). The pump laser provides a single wavelength (532 nm) with a power of 5W. The spectral range of the Ti-Sapphire laser is from (720 -825) nm. Wavelength tuning of the Ti-Sapphire laser (0.17cm^{-1} band width) is obtained by using a birefringent filter controlled with micrometer and driven by a stepper motor.

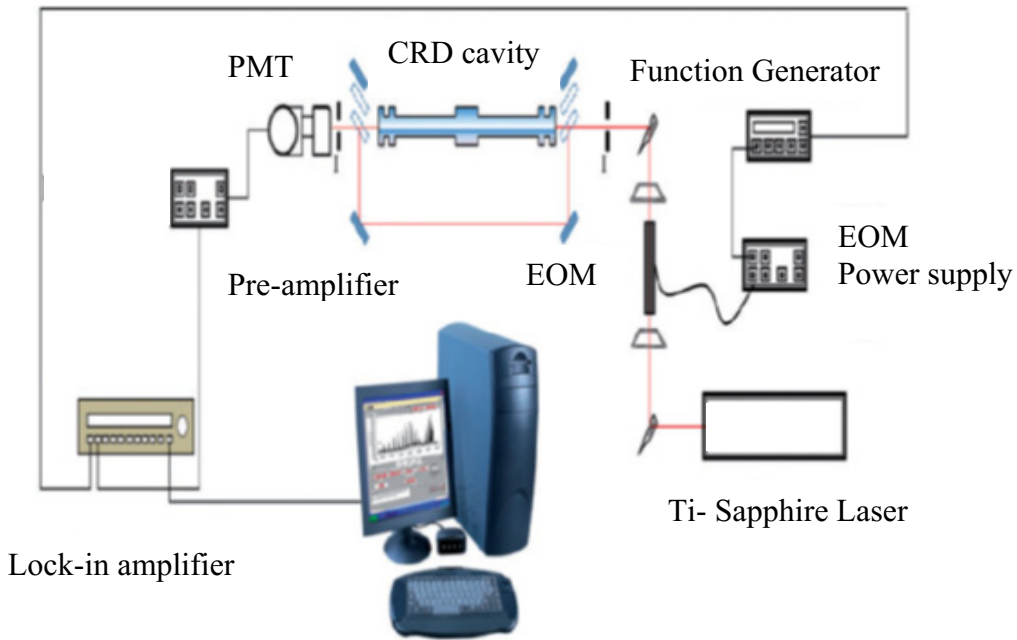


Figure 7. Experimental setup of the PS-CRD spectrometer [39]

The stepper motor is controlled with the LabVIEW software (National Instruments, version 13.0.1). The micrometer position is calibrated with the output wavelength of the laser. The laser beam coming out of the Ti-Sapphire laser is modulated by an electro-optic

modulator (Conoptics, 350-50) which is driven by a Stanford Research System (SRS model DS335) frequency generator. The modulated beam is a square wave, usually within 10–23 kHz frequency range. The beam is injected on-axis in to the optical cavity after passing through a lens. The beam is aligned inside a cavity in such a way that it gets reflected back and forth many times and increases the optical path length 3.9 km. The beam coming out of the optical cavity is detected with a Photomultiplier tube (PMT) which is powered by a high voltage power supply. The signal from the detector is now sent to a low-noise preamplifier (SRS model 560) for signal conditioning. After that, the signal is locked by a lock-in amplifier (SRS model 830) in reference with the signal coming from the function generator, and it measures the phase shift angle of the signal leaking out of the cavity.

In order to measure the phase shift angle of the light leaking out of the cavity, at first the cavity bypass is locked by lock-in amplifier with reference signal from the function generation and obtain the phase shift angle zero by pressing the phase button presents on the front panel of the lock-in amplifier. After that, the signal from the cavity is locked in and the phase-shift angle is measured with respect to the zero phase angle of the bypass laser beam. At the end, the values of the phase shift angles and signal voltages are sent to the computer via GPIB interface where they are processed by a LabVIEW program which was written specifically for this system.

1.2.2 Open Path Optical Cavity

An open path (no optical windows) optical cavity was constructed and used for temperature measurement of flowing air as shown in Figure 8. The open cavity is very useful at high temperatures and avoids the risk of damaging the highly reflective mirrors. The optical cavity consists of two highly reflective mirrors; M₁ and M₂ (Los Gatos

Research, 99.997%) which are mounted parallel to each other and separated by a distance of 93 cm. A hollow glass tube with 63 cm length and 3.2 cm inner diameter was placed in between the mirrors. The tube has a central valve for the air flow injection. N₂ gas from the laboratory supply flows around the two mirrors as a buffer gas, which helps the mirrors keep clean, avoids the risk of damage from the hot air flow and removes the atmospheric oxygen outside the glass tube.

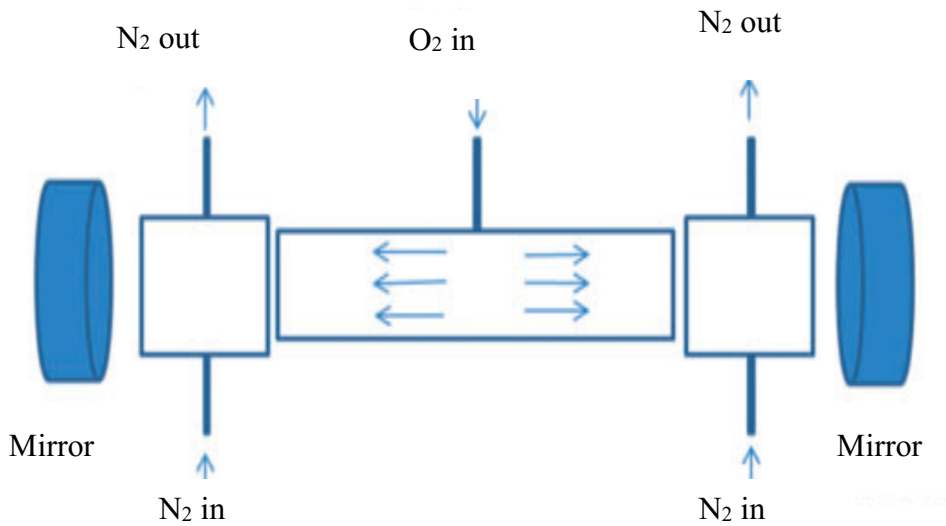


Figure 8. Open-path (no windows) optical cavity

1.2.3 Calibration of Thermocouple Sensor

Water was heated at several temperatures and both a thermocouple and thermometer were inserted into heated water. The simultaneous measurement of voltage and temperature of heated water was obtained. In order to measure the voltage, the thermocouple was connected with MICRONTA AUTO RANGE DIGITAL MULTIMETER. Table 4 presents the voltage reading at several temperatures. Figure 9 shows a plot of voltage versus temperature ($^{\circ}\text{C}$) which acts as a calibration curve.

Table 4. Data for the Calibration of Thermocouple

Multimeter (volts)	Thermometer ($^{\circ}$ C)
0	20.5
0.1	30
0.4	35
0.6	40
0.9	45
1.1	50
1.3	55
1.5	60
1.7	65
2.0	70
2.2	75
2.3	80
2.5	85
2.7	90
3.1	98

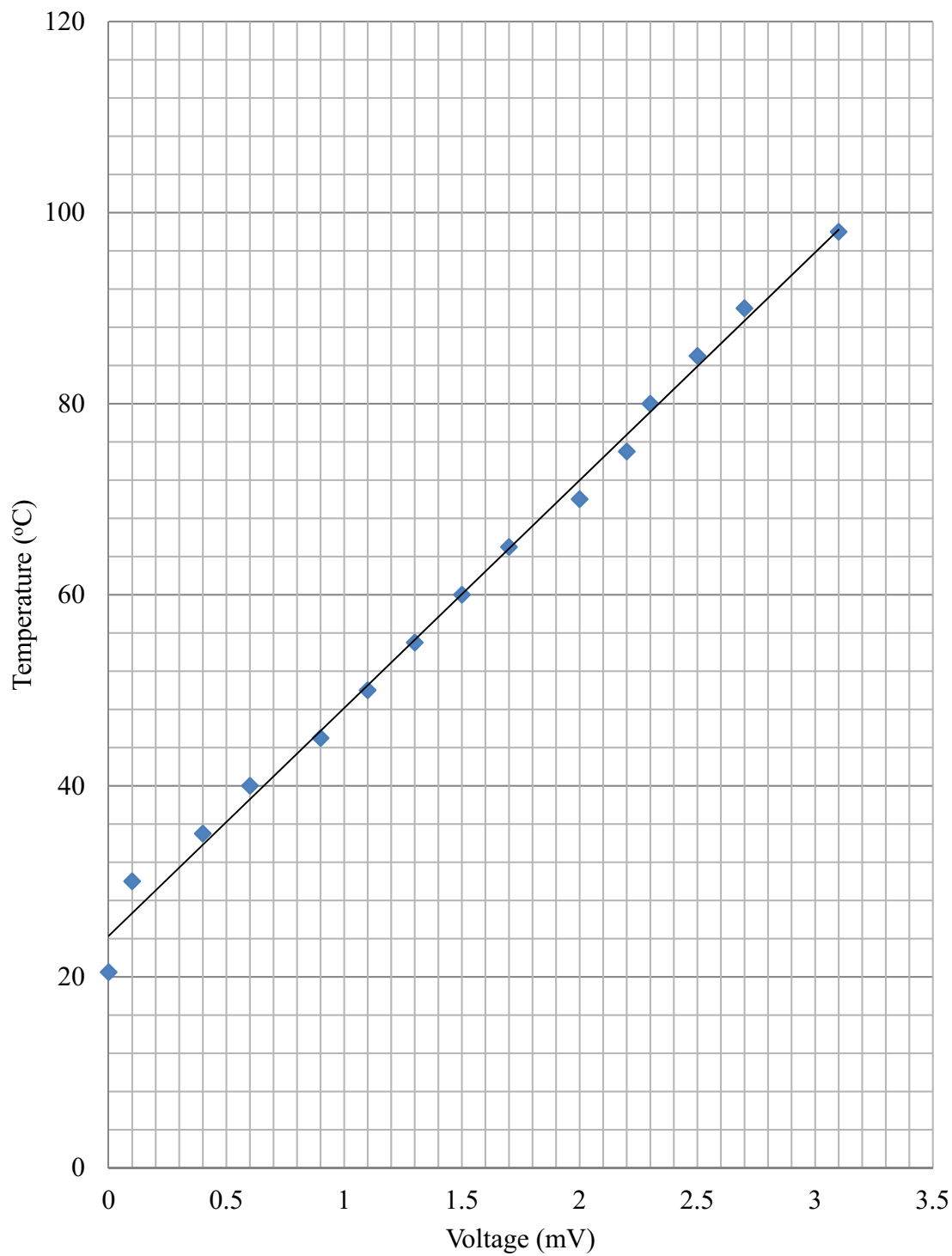


Figure 9. Calibration of thermocouple for the experimental temperature determination

1.2.4 Temperature Measurement of the Flow Air with Thermocouple Sensor

The calibrated thermocouple sensor was inserted into the hollow glass tube which was located in between the two mirrors of an optical open cavity and wrapped with heating tape. To make the tube hot, the heating tape was plugged into a high voltage supply. A particular temperature was obtained by adjusting a power controller meter scale and waiting at least 30 minutes to get the stable voltage reading. An air tank valve was opened, and air flow was passed through a heated copper coil to produce the flow of preheated air. Now the preheated air is injected into a heating tube through its central valve.

The constant flow of air was maintained with a flow meter. The voltage reading was obtained with the multimeter, and the calibration curve was used to measure the temperature of the air flow. The observed temperature is denoted as experimental temperature. To increase the temperature of the flow air, we increased the value of meter scale on the high voltage power supply. In this project, we performed experiments up to 100°C. We were able to get the experimental temperatures of the hot air by using the calibration curve as shown in Figure 9.

1.2.5 Cleaning of Optics

The process of cleaning of the optics is considered as an initial step in the experimental procedure. This begins with blowing of the nitrogen gas to remove the dust particles on the surface of the optics. After that, spectroscopic grade acetone, methanol, or a combination with Berkshire Lensx® 90 cleanroom wipes are used to clean the optics. Sometimes, if the optics is really dirty, optical soap can be used.

1.2.6 Alignment of the Pump Laser Beam in to a Laser Cavity

The process of cleaning of optics is followed by alignment of the laser beam inside the optical cavity. In order to align a beam into a cavity, first a solid state, frequency doubled neodymium-yttrium vanadium oxide (Nd-YVO₄) laser (Coherent Verdi) providing a single wavelength (532 nm) which acts as a pump laser is turned on at a maximum power of 5W. The pump beam gets into a Ti-Sapphire laser (Coherent 899 ring laser, linewidth 0.17 cm⁻¹) cavity. The micrometer connected to the birefringent filter was rotated and stayed at the place of maximum florescence of the Ti-Sapphire crystal. The pump beam was aligned inside the laser cavity by following the laser manual. The power meter was placed in the path of the output of the laser, and optimization of the power was obtained by using the various outer control knobs.

1.2.7 Alignment of a Laser Beam in to an Open Path Optical Cavity

The laser beam was injected into a CRD optical cavity through the center of the mounted front mirror holder. The light emerging out through the center of the rear mirror holder was aligned to the shutter of the photomultiplier detector which was mounted on the translational stage and operated at 1000 V power. After that, the rear mirror was put back into the holder and mounted. The back reflection from the rear mirror was overlapped with the injected laser beam by using the controls on the mount. An iris was placed at the center of the cavity which helps to overlap the reflected beam. The shutter of the photomultiplier tube detector (PMT) was then opened which allowed us to maximize the intensity of the square signal on the oscilloscope by moving the PMT in small increments on x, y and z directions. After that, the front mirror was placed similar to the rear mirror, and the CRD signal was optimized by using the controls on the front mirror mount. Finally, the hollow

glass tube was placed between the mirrors. The beam was passed exactly through the center of the tube, and the intensity of the signal on the oscilloscope was not affected.

1.2.8 Phase Shift Angle Measurement

For the measurement of the phase shift angle, the position of the micrometer which is connected with birefringent filter was fixed at the spectral region where oxygen in air has no absorption. Figure 10 depicts the phase shift angle measurement. The modulated laser beam is divided into two parts by using a beam splitter. One part of the beam is injected in to the cavity and the other part of the beam (bypass) is used as a reference beam.

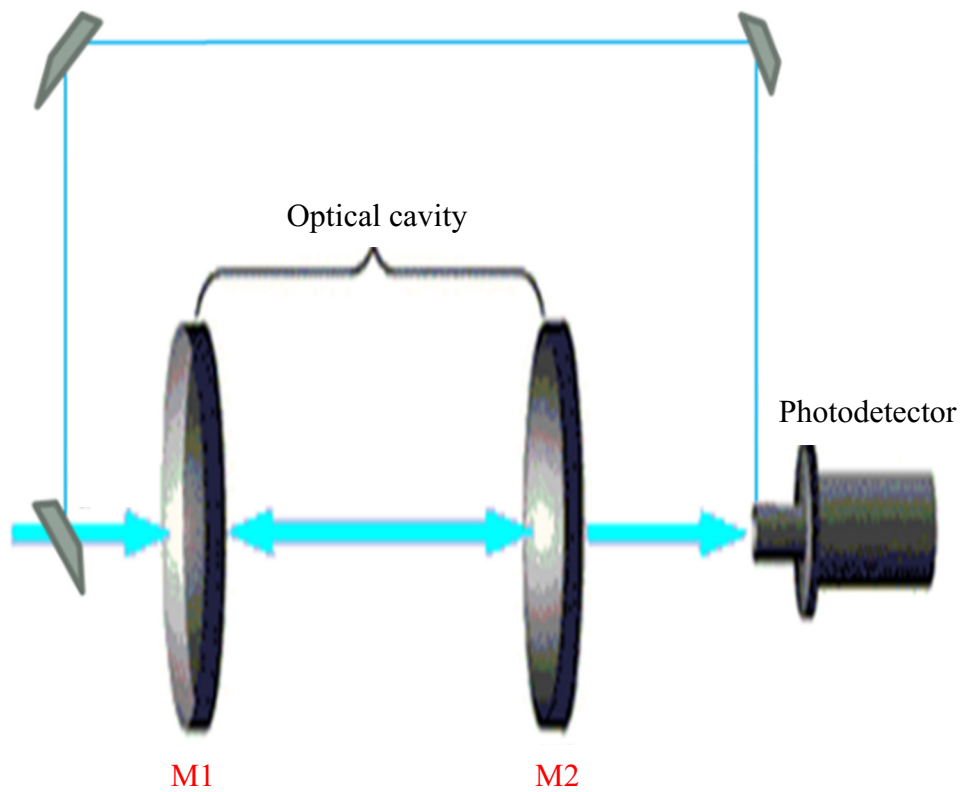


Figure 10. Reference phase shift angle measurement

At first, the bypass of the cavity was aligned with the PMT detector by using the diverting mirror. The signal from the detector was connected to the lock-in amplifier through the preamplifier. In the lock-in amplifier, the bypass signal was locked-in with reference square signal coming from the function generator. A zero-phase shift angle of the bypass signal was obtained. After that, the diverting mirror was removed and the signal from the cavity was directed to the detector. Finally, the cavity output signal was locked-in by the Lock-in amplifier. At this point, the lock-in amplifier measured the phase shift angle of the cavity output signal with respect to zero phase shift angle of the bypass.

The phase shift angle was affected by the change in temperature. we always maintained the phase shift angle close to -45° by changing the frequency. For the strong and narrow laser beam, the phase shift angle was not affected by the flow rate of air.

After that, the micrometer was moved and placed at the initial position of the spectral range of A-band of oxygen. The micrometer was then connected with the shaft of a stepper motor with a belt. Finally, the scans were made by using the LabVIEW program and spectral data were obtained. The spectral signals were optimized by applying the optimum values for various instrumental parameters which are listed in Table 5.

Table 5. Parameters for the Optimization of CRD Signal

Frequency (kHz)	Sensitivity (mV)	Time constant (s)	Gain	Slope (dB)	Wait (s)	Flow rate (Lit/min)
10-22	2-200	3	20-100	12-18	0-0.3	0-15

1.3 Phase Shift Cavity Ring-Down Spectroscopy of Oxygen in Flowing Air

For temperatures above 295 K, a hollow glass cylindrical tube without windows has been inserted inside an optical cavity to measure the temperature of air flowing through the tube. The cavity consists of two highly reflective mirrors which are mounted parallel to each other and separated by a distance of 93 cm. In this experiment, air is passed through a heated tube. The temperature of the air flowing through the tube is determined by measuring the intensity of the oxygen absorption as a function of the wavenumber.

The A-band of oxygen is measured between 298 K and 373 K, with several air flow rates. To obtain the temperature, the energy of the lower rotational state for seven selected rotational transitions is linearly fitted to a logarithmic function that contains the relative intensity of the rotational transition, the initial and final rotational quantum numbers, and the energy of the transition (Eq. 16).

Accuracy of the temperature measurement is determined by comparing the calculated temperature from the spectra with the temperature obtained from a calibrated thermocouple inserted at the center of the tube.

This flowing air temperature sensor will be used to measure the temperatures of cooling air at the input (cold air) and output (hot air) after cooling the blades of a laboratory gas turbine. The results could contribute to improvements in turbine blade cooling design.

Figure 11 shows the A-band of oxygen in the static air at 298 K. Because of the low resolution of the laser (0.17 cm^{-1}), four branch (${}^P\text{P}$, ${}^R\text{R}$, ${}^P\text{Q}$, ${}^R\text{Q}$) were not completely resolved. However, we do the assignment of the partially resolved ${}^P\text{P}$ and ${}^P\text{Q}$ branch of the spectrum of the A- band of oxygen. As shown in Figure 11 only the ${}^P\text{P}$ branch was assigned and its intensity measured for the temperature determination.

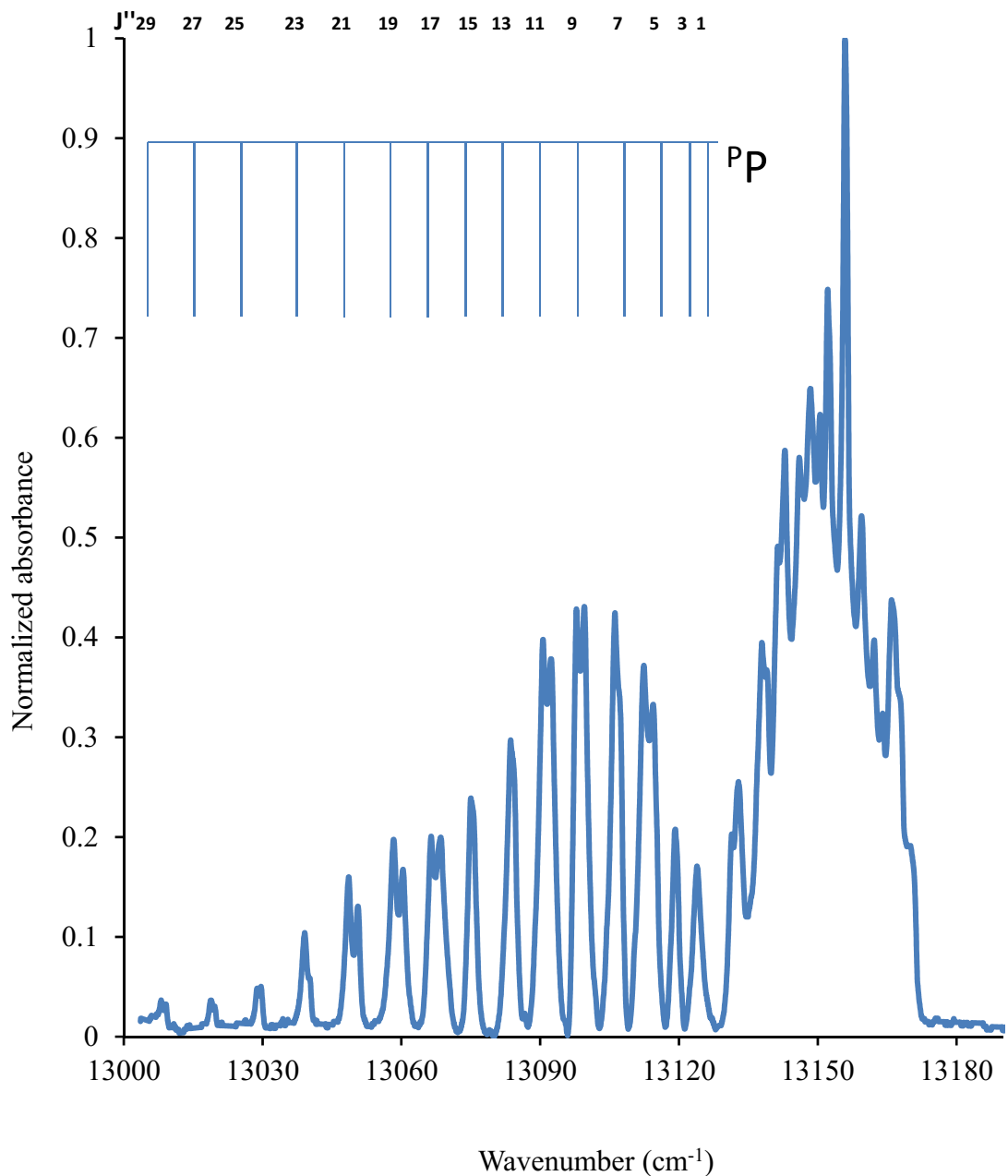


Figure 11. Normalization of the A-band of oxygen with designation of ${}^P\text{P}$ branch

Air Flow at 298 K

We performed several experiments at specified temperatures with different flows of air. Figure 12 shows the flow series of the A-band of oxygen in air at temperature 298K. The spectra are obtained with zero (static) flow rates to a maximum of 15 L/min. Table 6 presents the relative intensity and energy of the 3P transitions of the A-band of oxygen in different flows of air at temperature 298 K. Here we noticed that because of the scattering effects, the overall intensities show a small decrease as the flow rate increases. However, the temperature measurement does not depend on the air flow rate. After baseline correction and normalization of the signal, the distribution of intensities is similar at a particular temperature.

The normalization is carried out by dividing the absorption value of every point with the highest value of absorption. Once the corrections were made, the signals were treated as several measurements at a given temperature regardless of the flow rate and we obtained the average relative intensity of the 3P transitions. The temperature of O₂ was determined by using the position and rotational line intensities of the A-band. For high resolution spectra, there are equations (equation 15 and 16) to describe the intensity of individual lines as a function of the energy of the initial rotational transitions [79,84]. These equations (equation 15 and 16) take into account the spin-orbit interaction of the ground state of O₂ and reproduce the intensities measured at high resolution. For our low-resolution spectra, it is not important to reproduce the actual intensity of the individual lines, and only the relative intensities are important to calculate the temperature. For this reason, several spectra at the same temperature were normalized with respect to the highest peak of each spectrum.

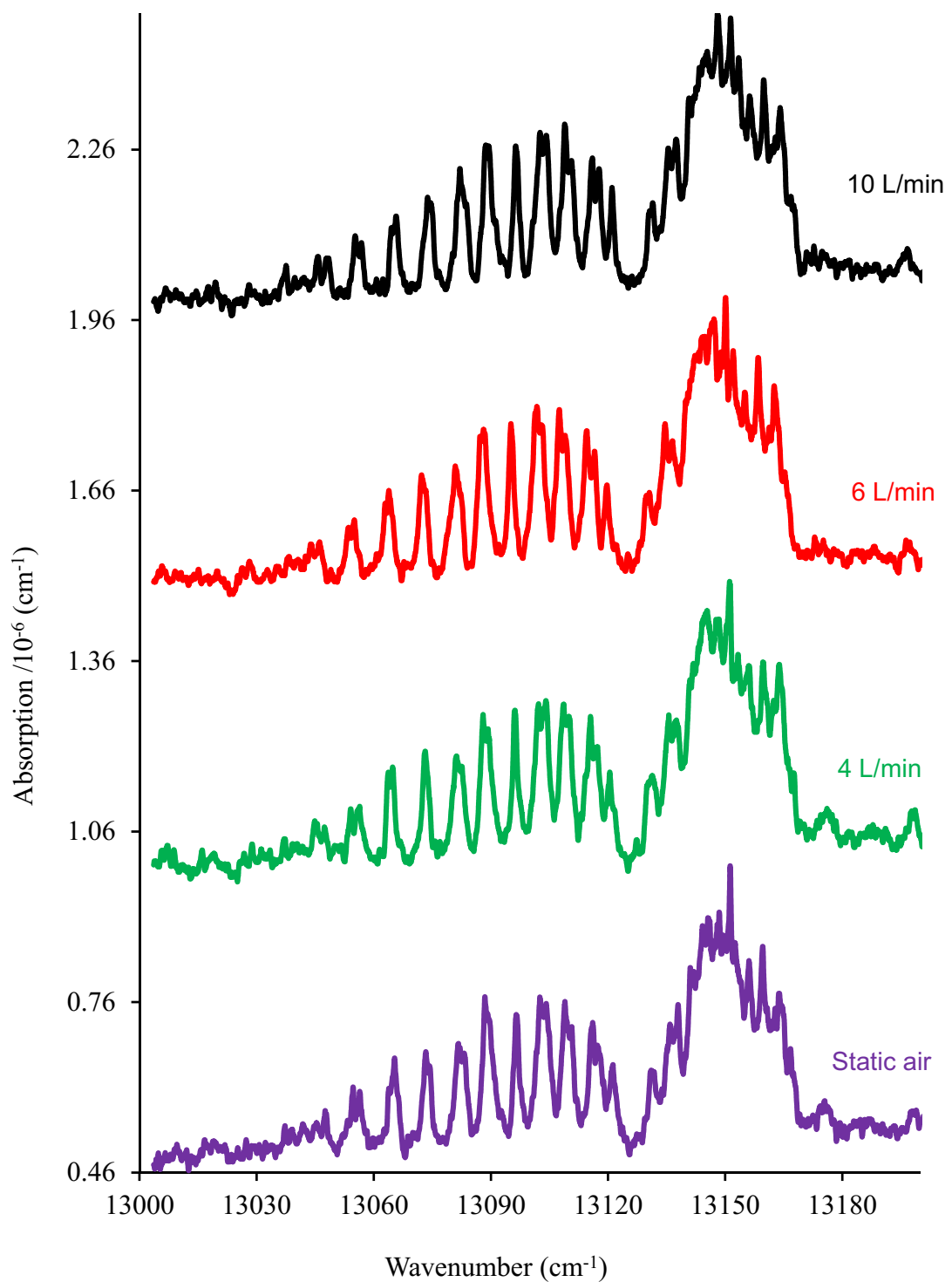


Figure 12. Flow series of the A-band of oxygen in air at 298 K

Table 6. Relative Intensity of the ^PP Branch of the A-band of Oxygen
at 298 K with Several Air Flow Values

^PP	Intensity at different air flow (L/min)					$\ln(\text{int.}/\sigma*(J''+J'+1))$	$B.J''(J''+1) + 2\lambda - \gamma$
J''	0	4	6	10	Avg.		
1	0.057	0.077	0.103	0.119	0.089	-24.3203	6.8518
3	0.068	0.166	0.203	0.19	0.1565	-24.8541	21.2288
5	0.147	0.178	0.225	0.216	0.1915	-25.1625	47.1074
7	0.175	0.208	0.258	0.247	0.222	-25.3508	84.4876
9	0.19	0.213	0.222	0.222	0.212	-25.6488	133.3694
11	0.17	0.231	0.222	0.233	0.124	-25.8384	193.7528
13	0.133	0.148	0.19	0.203	0.1685	-26.2439	265.6378
15	0.099	0.181	0.155	0.15	0.1463	-26.528	349.0244
17	0.075	0.133	0.097	0.113	0.1045	-26.9887	443.9126
19	0.07	0.076	0.075	0.073	0.0735	-27.4511	550.3024
21	0.054	0.045	0.022	0.042	0.0108	-28.1402	668.1938

The only transition considered are the 3P transitions that correspond to absorptions from the ground state's rotational quantum number $J''=N''=1, 3, 5, 7\dots$; with final states $J'=0, 2, 4, 6\dots$ respectively. Figure 13 is the plot of $\ln(\text{abs.int}/\sigma^*(J''+J'+1))$ versus $B.J''(J''+1) + 2\lambda\gamma$ for the A-band of oxygen in air flow at 298 K. We observed a straight line with a slope of -0.0048 cm. The calculated temperature is 299 K which is obtained from the product of the inverse of the slope with $1.43879 \text{ K/cm}^{-1}$.

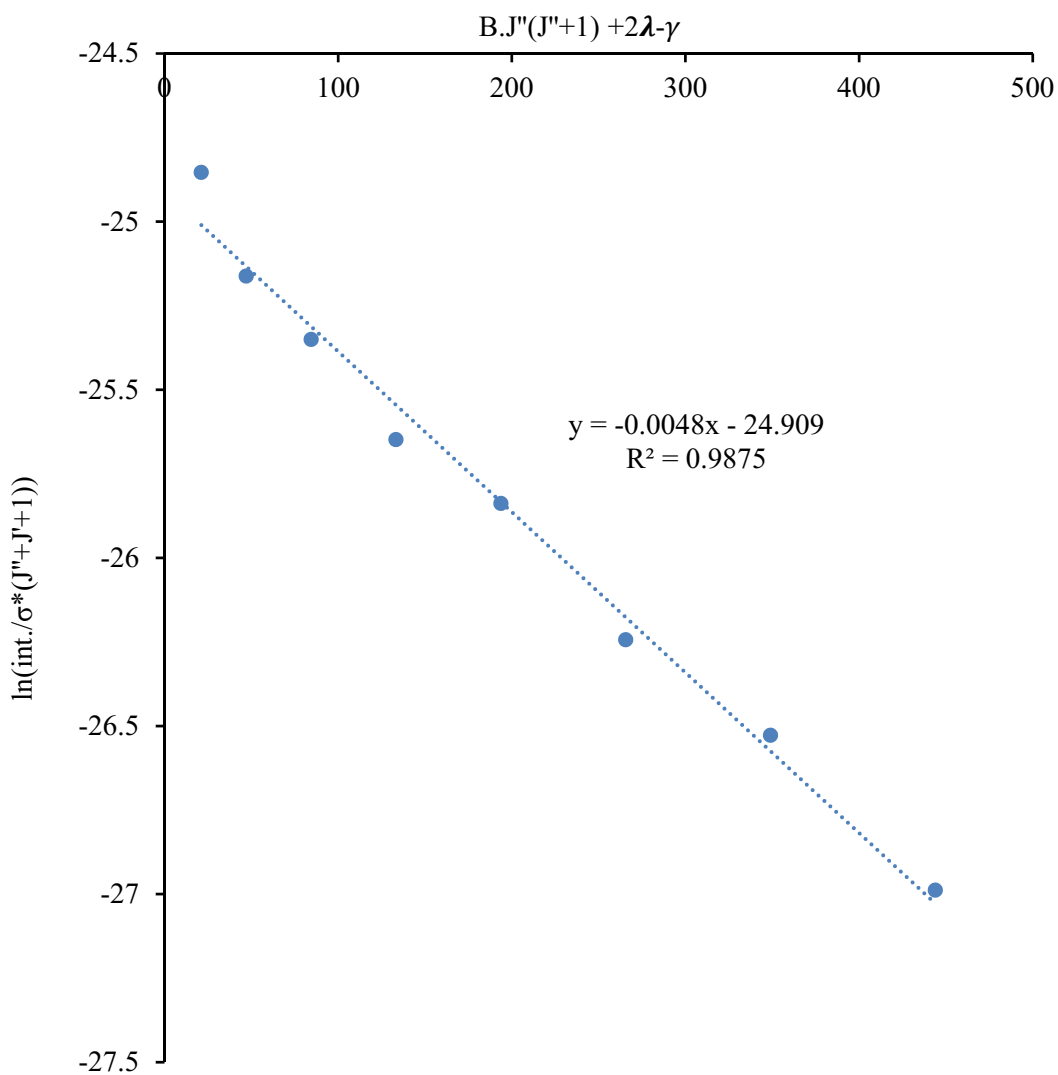


Figure 13. Plot of $\ln[\text{int. } / \sigma^* (J'+J'' + 1)]$ versus $BJ''(J'' + 1) + 2\lambda\gamma$ of the A-band of oxygen in air flows at 298 K

Air Flow at 321 K

We also performed several experiments with different flow rates of air at 321 K. Figure 14 shows the flow series of the A-band of oxygen in air at 321 K. The spectra are obtained with a minimum flow of 6 L/min to maximum of 15 L/min. Because of the scattering effect, the overall intensity of the spectrum decreases with increase in air flow rate. Table 7 shows the relative intensity and energy of the ${}^P P$ branch of the spectra. After the normalization, the spectra at different air flows were treated as several measurements for a particular temperature.

At this temperature (321 K), the intensity of the molecules shifted towards the lower energy side in comparison to the spectra at room temperature. The shifting of the intensity distribution is explained with the Boltzmann distribution law.

Figure 15 shows the plot of $\ln \left(\frac{I_{\text{abs}}}{(\sigma^*(J'+J''+1)} \right)$ versus $F_{J''}$ (from equation 16) of the A-band of oxygen in air flow at 321 K. The plot produces a straight line with a slope of -0.0044 and reflects the temperature 326 K. The calculated temperature agreed ± 8 K with the experimental temperature. To obtain the plot, we included the ${}^P P$ transitions of the A-band of oxygen originating from $J'' = N'' = 5, 7, 9, 11, 15, 17$ and 19. The transitions were selected because they are more intense, are more sensitive to the temperature change, and gave a linear plot. The points corresponding to $J''=1$ and 3 deviates from the straight line. Inclusion of these points in the plot does not affect the calculated temperature but increase the uncertainty. Each experimental point in the plot is the average of the peak value obtained for several normalized spectra.

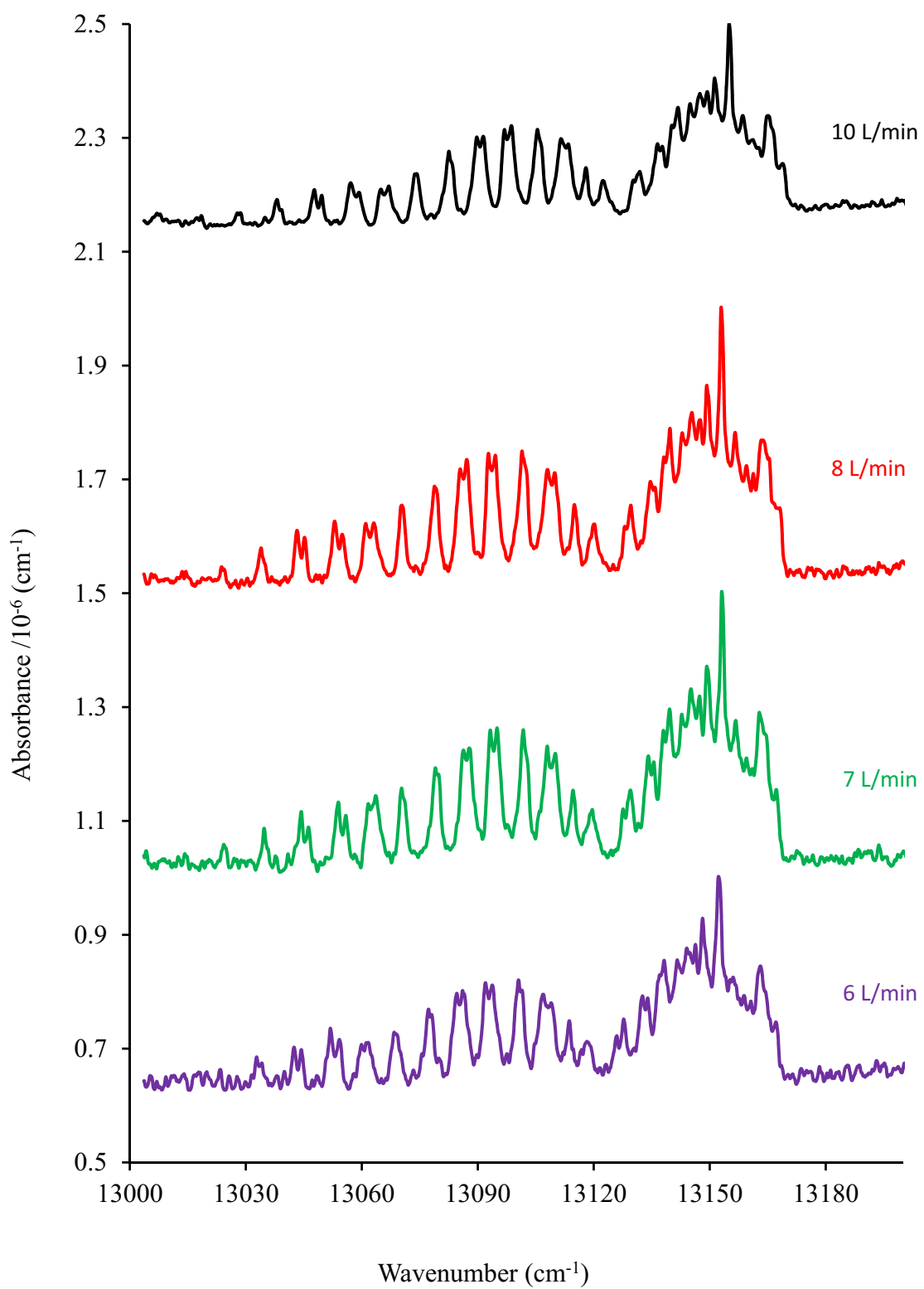


Figure 14. Flow series of the A-band of oxygen at 321 K

Table 7. Relative Intensity of the 3P Branch of the A-band of Oxygen
at 321 K with Several Air Flow Values

J''	6	7	8	10	Avg.	$\ln(\text{int.}/\sigma*(J''+J'+1))$	$B.J''(J''+1) + 2\lambda - \gamma$
1	0.052	0.05	0.041	0.03	0.04325	-25.1097	6.8518
3	0.057	0.07	0.049	0.049	0.05625	-25.9451	21.2288
5	0.123	0.156	0.099	0.107	0.12125	-25.6874	47.1074
7	0.163	0.178	0.122	0.121	0.146	-25.8376	84.4876
9	0.168	0.182	0.128	0.135	0.15325	-26.0398	133.3694
11	0.153	0.166	0.128	0.128	0.14375	-26.3039	193.7528
13	0.127	0.137	0.102	0.111	0.11925	-26.6572	265.6378
15	0.106	0.107	0.08	0.078	0.09275	-27.051	349.0244
17	0.077	0.103	0.066	0.056	0.0755	-27.3814	443.9126
19	0.074	0.09	0.065	0.045	0.0685	-27.5892	550.3024
21	0.053	0.08	0.044	0.05	0.05675	-27.8768	668.1938

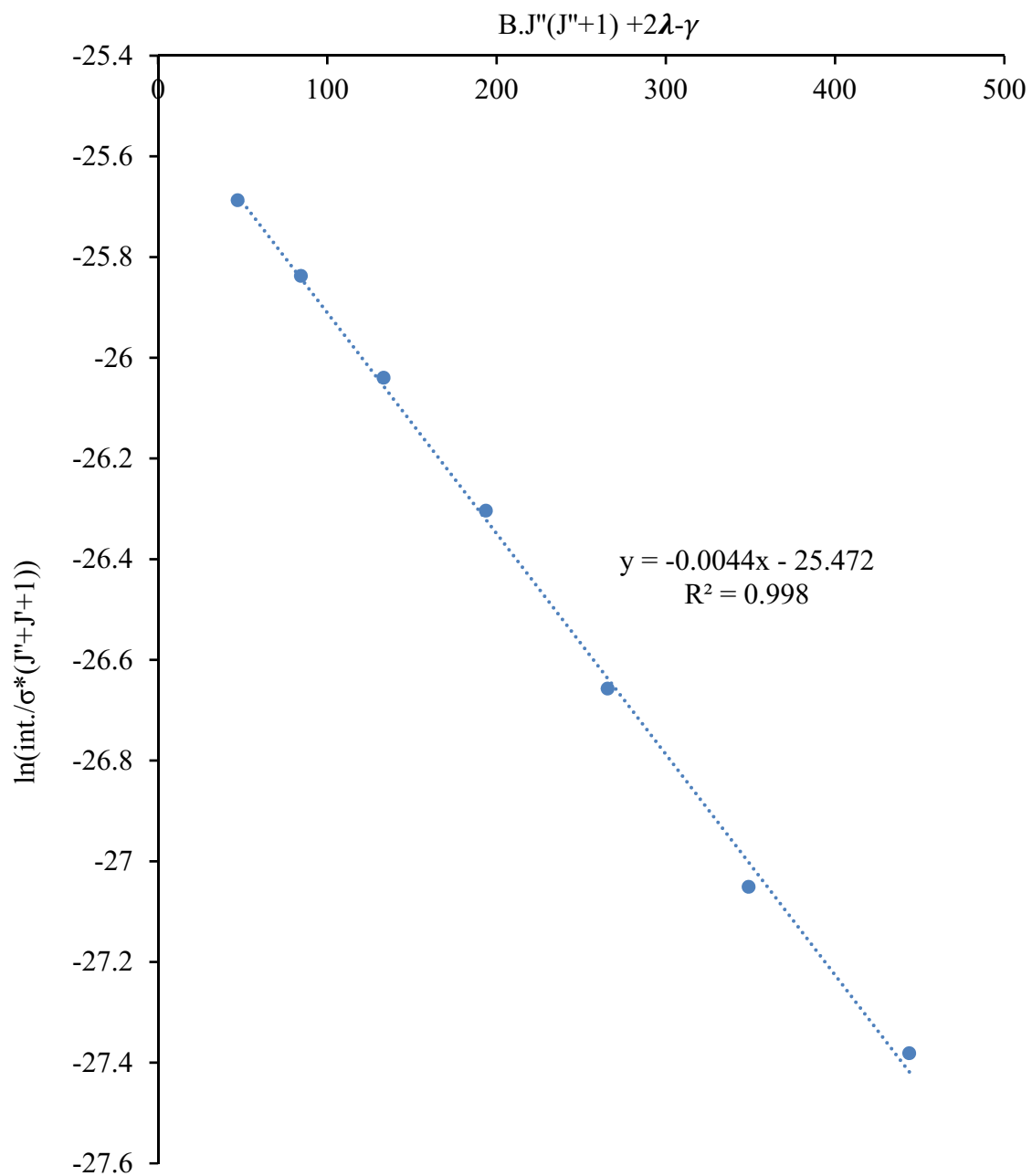


Figure 15. Plot of $\ln [\text{int.} / \sigma^* (J'' + J' + 1)]$ versus $B.J''(J'' + 1) + 2\lambda - \gamma$ of the A-band of oxygen in air flows at 321 K

Flow Series at 359 K

We repeated the same experiments at a temperature of 359 K. Figure 16 depicts the flow series of the A-band of oxygen in air at temperature 359 K. The spectra are obtained with several flow rates from 6 L/min to 15 L/min. Table 8 presents the relative intensity and energy of the 3P branch of the A-band of oxygen at different flow rates. The intensity of molecules in these spectra shifted more towards the lower energy side than in the spectra at 321 K (fig. 14).

Figure 17, represents the plot of $\ln \left(\frac{I_{\text{abs}}}{(\sigma^*(J'+J''+))} \right)$ versus $F_{J''}$ (from equation 16) of the A-band of oxygen in air flow at 359 K. In this plot, we obtained a straight line with a slope of 0.004 cm and the calculated temperature was 359 K. The calculated temperature agreed ± 11 K with the experimental temperature measured with a thermocouple sensor. At this temperature also, we included the 3P transitions originating from $J'' = N'' = 5, 7, 9, 11, 15, 17$ and 19. The transitions were selected because they are more intense, are more sensitive to the temperature change, and gave a linear plot.

The points corresponding to $J'' = 1$ and 3 deviate from the straight line. Inclusion of these points in the plot does not affect the calculated temperature but increase the uncertainty in the measurement. Each experimental point in the plot is the average of the peak value obtained for four normalized spectra.

Previously, Y. Perez Delgado in our laboratory obtained the spectral data of the A-band of oxygen at cryogenic temperatures. She used a 45 cm long optical cavity attached to a low temperature cryostat for the measurements. The static cell and mirrors of the optical cavity are all inside a vacuum chamber at the same temperature of the cryostat.

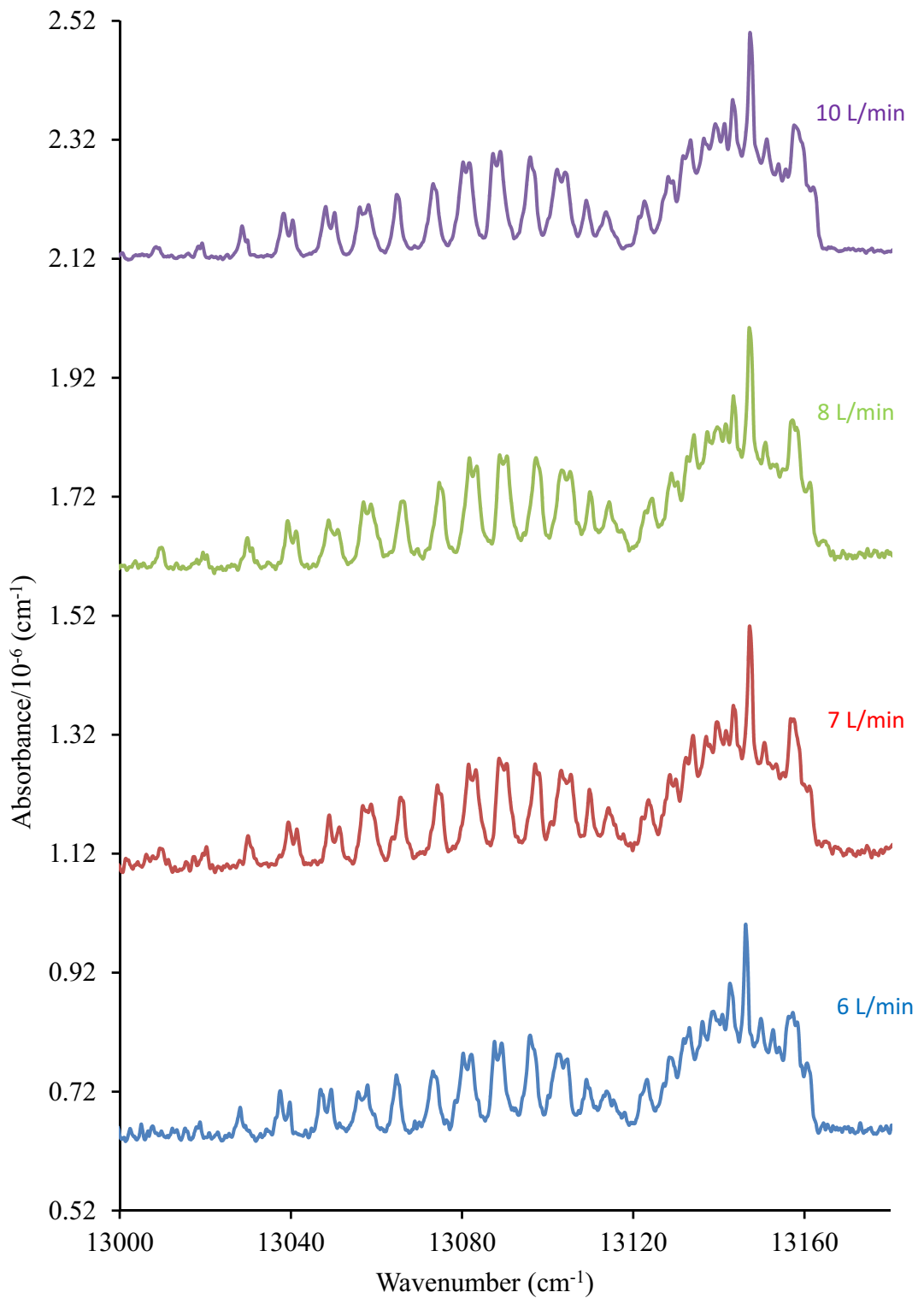


Figure 16. Flow series of the A-band of oxygen at 359 K

Table 8. Relative Intensity of the 3P Branch of the A- band of Oxygen
at 359 K with Several Air Flow Values

3P	Intensity at different air flow (L/min)					$\ln(\text{int.}/\sigma^*(J''+J'+1))$	$B.J''(J''+1) + 2\lambda - \gamma$
J''	6	7	8	10	Avg.		
1	0.023	0.038	0.041	0.03	0.033	-25.215	6.8518
3	0.051	0.072	0.064	0.05	0.05925	-25.728	21.2288
5	0.095	0.11	0.105	0.1	0.1025	-25.6902	47.1074
7	0.126	0.124	0.133	0.129	0.128	-25.804	84.4876
9	0.128	0.136	0.142	0.134	0.135	-26.0014	133.3694
11	0.121	0.136	0.151	0.133	0.13525	-26.1997	193.7528
13	0.093	0.112	0.122	0.1	0.10675	-26.6029	265.6378
15	0.088	0.097	0.086	0.088	0.08975	-26.9188	349.0244
17	0.057	0.088	0.093	0.071	0.07725	-27.1934	443.9126
19	0.064	0.071	0.067	0.073	0.06875	-27.4203	550.3024
21	0.067	0.065	0.067	0.063	0.0655	-27.5681	668.1938

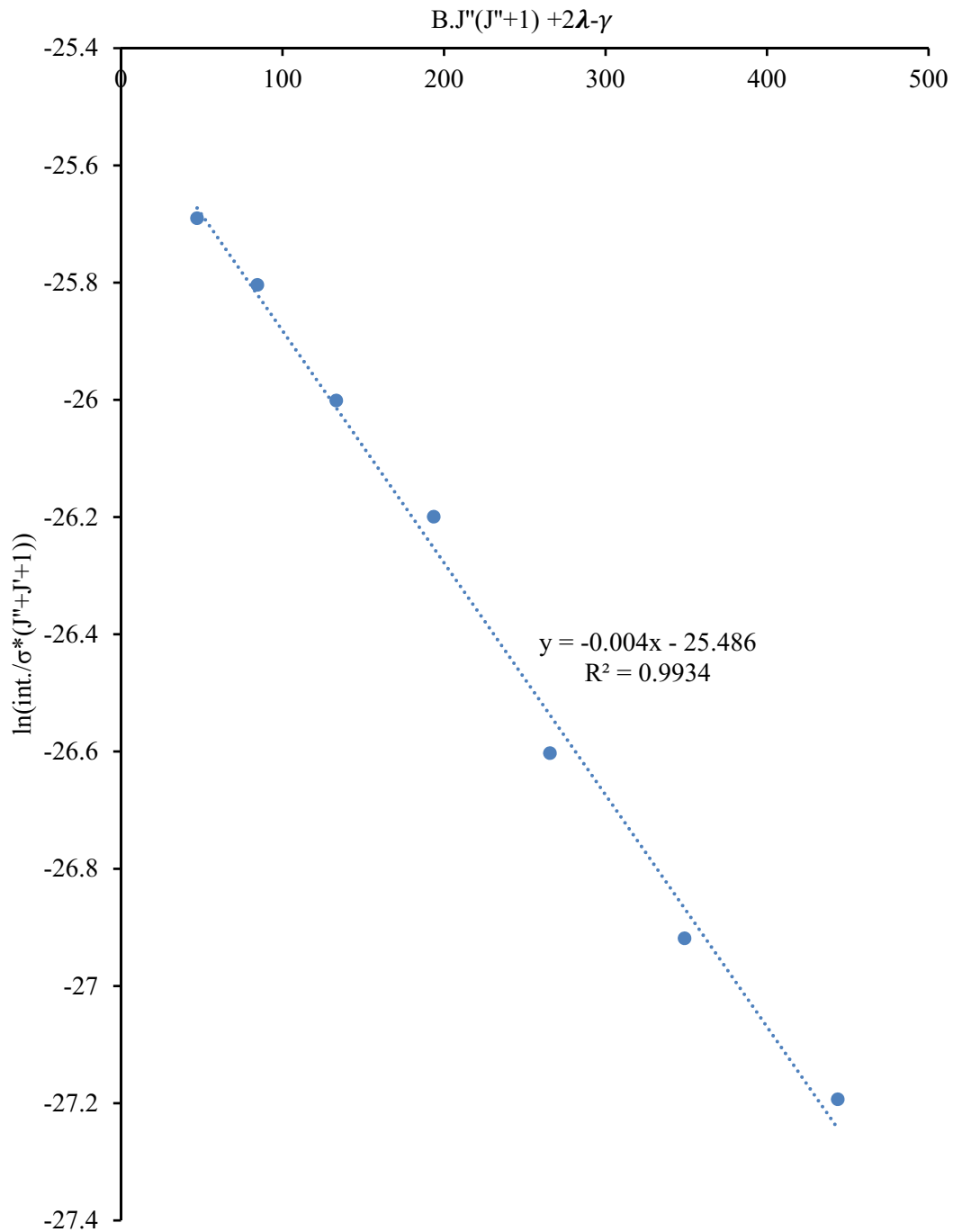


Figure 17. Plot of $\ln [\text{int}/\sigma^*(J'+J''+1)]$ versus $BJ''(J''+1) + 2\lambda \cdot \gamma$ of the A-band of oxygen in air flows at 359 K

The vacuum chamber insulates the optical cavity and the cold head of the cryostat from the environment. The cell temperature can be changed between 10 K and 295 K. For sample cooling an international Cryogenics controlled temperature cryostat model 31-4000 system was used. The cell was connected to the external gas handling system through a small section of stainless steel tubing. The cell temperature was controlled with a scientific Instruments model 9650 temperature controller and indicator.

In this dissertation, we have applied our method to analyze the spectral data of the A-band of oxygen at cryogenic temperatures. The cryogenic spectral data were obtained with pure oxygen. The calculated temperatures agreed with the experimental temperature measured by the sensor.

Table 9 shows the number of spectra used to obtain an average intensity (# Peaks averaged), the slope of the line, and the intercept are presented with standard deviations and the R^2 values. The calculated temperatures are shown with their respective standard deviations. The maximum error is 6% at 88 K and the minimum is 2% at 301 K. If the first two points corresponding to $J'' = 1$ and 3 are included in the fit for temperatures higher than 301 K the slope produces the same calculated temperature but the error increases because the points deviate above and below the line, respectively. The first two points were not included in the fit for temperatures higher than 301 K. The most common spectroscopic method of temperature determination in the literature [85-87] is the ratio of measured absorbance of two rotationally resolved transitions. Usually the two transitions are selected based on absorption strength, spectral isolation, and temperature sensitivity to maximize the accuracy of temperature determinations. For the low-resolution spectra obtained in this investigation, the use of two absorptions bands did not give consistent results even after

computer deconvolution of the selected bands. As shown before, the selection of the same seven maximum values of the ${}^3\text{P}$ transitions gave consistent and accurate results for the range of temperatures measured.

Table 9. Accuracy of the Temperature Sensor

Average peaks (n)	Slope/ 10^{-3} cm	Intercept	R^2	Calculated temperature (K)	Measured temperature (K)
6	$-(16.4 \pm 0.8)$	$-(24.32 \pm 0.09)$	0.9896	88 ± 5	90
4	$-(9.62 \pm 0.54)$	$-(24.60 \pm 0.12)$	0.9779	150 ± 8	150
7	$-(4.78 \pm 0.09)$	$-(25.47 \pm 0.02)$	0.9980	301 ± 6	298
6	$-(4.40 \pm 0.10)$	$-(25.58 \pm 0.03)$	0.9973	327 ± 8	321
2	$-(4.12 \pm 0.12)$	$-(25.62 \pm 0.03)$	0.9957	348 ± 11	356
1	$-(3.76 \pm 0.15)$	$-(25.67 \pm 0.04)$	0.9914	386 ± 15	383

1.3.1 Validation of the Developed Method with Simulated Result

The optical sensor that we established in our laboratory for the measurement of temperature in flows of air was also validated with the simulated result. We obtained the simulated spectrum of the A-band of oxygen at several different temperatures. The figure 18 is one of the example of PHOPHER [88] simulated A-band of oxygen at 298K. Table 2 and Table 3 present the constants that we applied for the simulation. Normally, the temperature of the sample is calculated by overlapping the experimental spectrum with the simulated spectrum. However, in this project we validated the temperature sensor with simulated results in a different way. We applied a same method that we employed for the experimental spectrum to extract the temperature. We obtained the relative intensity of ${}^P P$ branch after the base line correction and normalization of the signal. Similar to the experimental results, the temperature is calculated from the slope of the Boltzmann plot (equation 16). Figure 19 shows the calculation of temperature of oxygen from the simulated spectrum at 298 K. The calculated temperature, determined from the slope of a straight line of the plot is $\sim 294 \pm 4$ K which is in agreement with the simulated temperature and helps to further validate our method.

1.3.2 Comparison with Another Method

Basically, the two-line thermometry (selection of two different transitions) has been used for the calculation of temperature from the high-resolution spectrum [86,87]. P. Maco and P. Veis [89] measured the gas temperature in an oxygen plasma from the intensity ratio of the maxima of R-branch and P-branch. It seems like this method is easier to calculate the temperature of the air. However, it has some difficulties, including the necessity of getting the actual instrumental function of a spectral device.

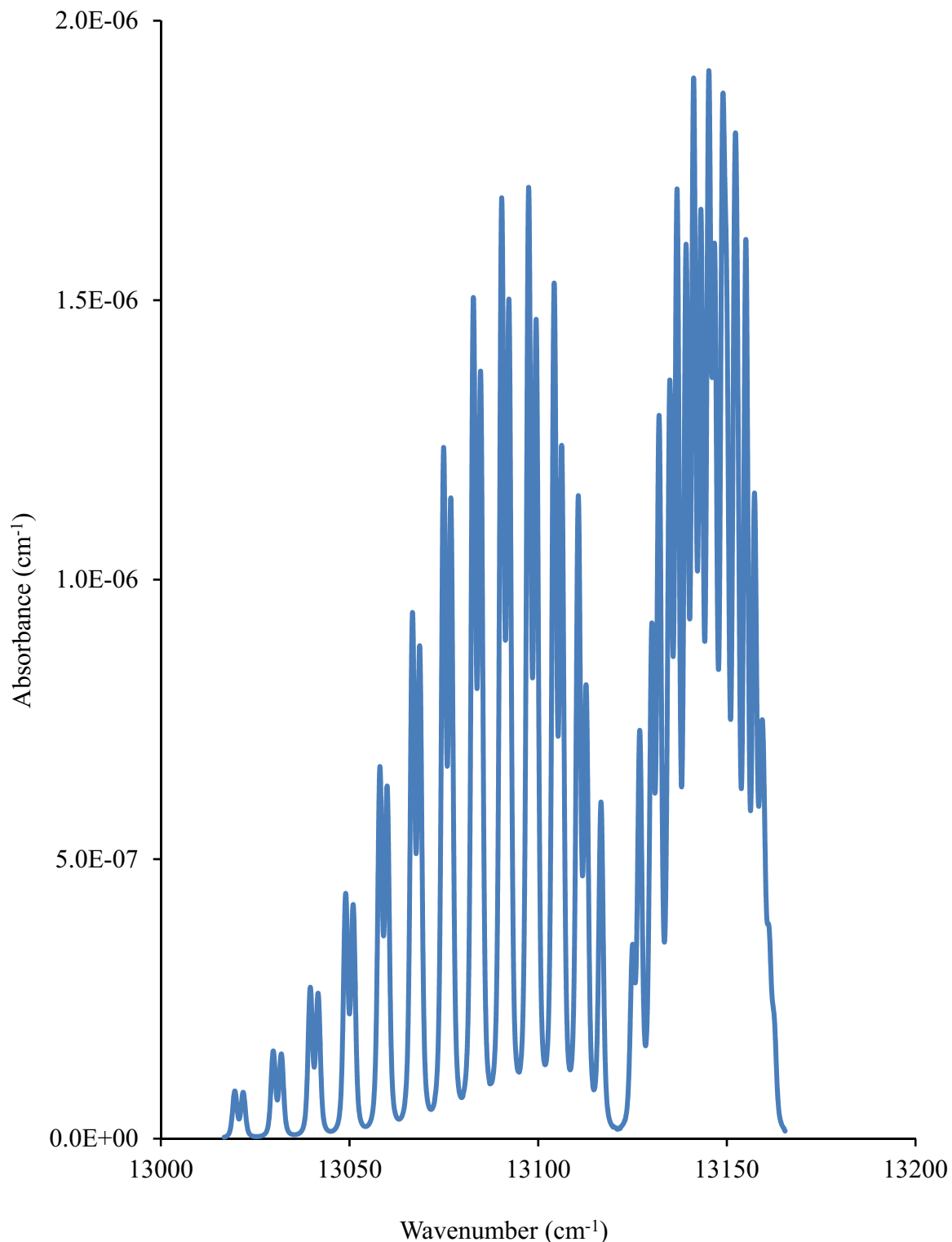


Figure 18. PGOPHER simulated spectrum of the A-band of oxygen at 298 K

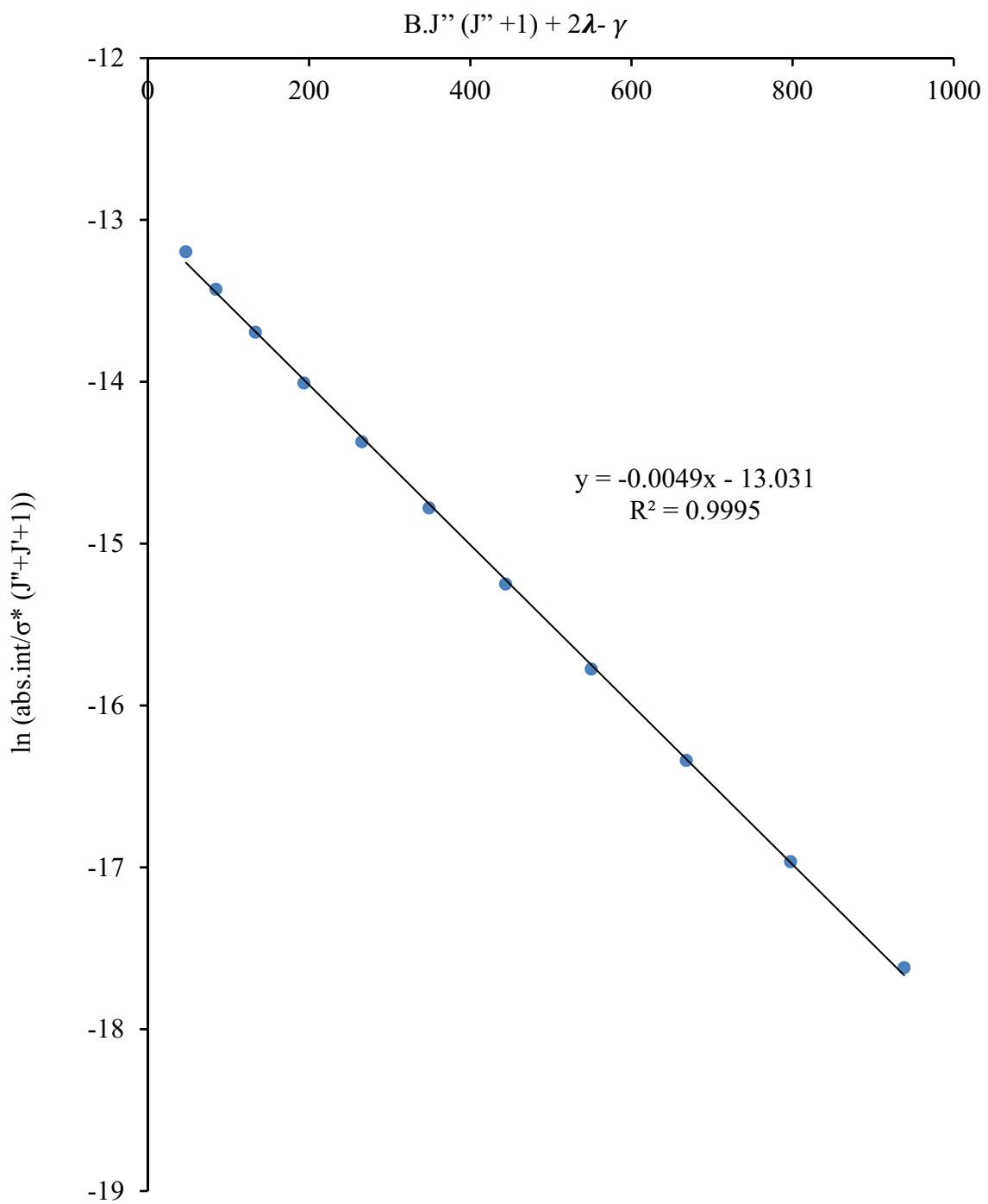


Figure 19. Calculation of temperature from the simulated spectrum of the A-band of oxygen at 298 K

They considered only two rotational transitions which might not be sufficient information to acquire the overall distribution of the molecule for the calculation of the temperature. This technique would not be the good temperature sensor at very high temperature and high flow system. They only applied their method at very low gas pressure and did not provide any information at high flow. Their results at very high temperature did not agree with simulated results. However, in our method, we used at least seven rotational transitions which could provide more information about the overall distribution of the molecule for the determination of the temperature. In addition, we performed experiments at high temperature with several different air flows. The results show that this method would be a good method for the flow system. In our low-resolution spectrum, R branch transitions are not resolved, and therefore, we could not use the maximum of R branch. However, we have tried to use two-line thermometry for the measurement of the temperature of the flowing air. We measured the ratio of intensity/integrated area of the P17 and P2 transitions for different temperatures. Table 10 presents their ratio in normalized spectra of the A-band of oxygen at several temperatures.

Table 10. The Ratio of Intensity/ Int. Area of the P17 and P2 transitions of the A-band of Oxygen at Various Temperatures

Intensity ratio (P17/P2)	Ratio of int. area (P17/P2)	Temperature (K)
1.1781	2.2797	298
1.4289	2.3197	321
1.4531	-	333
1.7244	2.3853	359

Similarly, figures 20 and 21 show the plots of temperature versus ratio. The plots show that the ratio increases linearly with increase in temperature. The curves agree with the nature of the curve obtained by P. Maco and P. Veis. We could use those curves as a calibration curve to obtain the temperature.

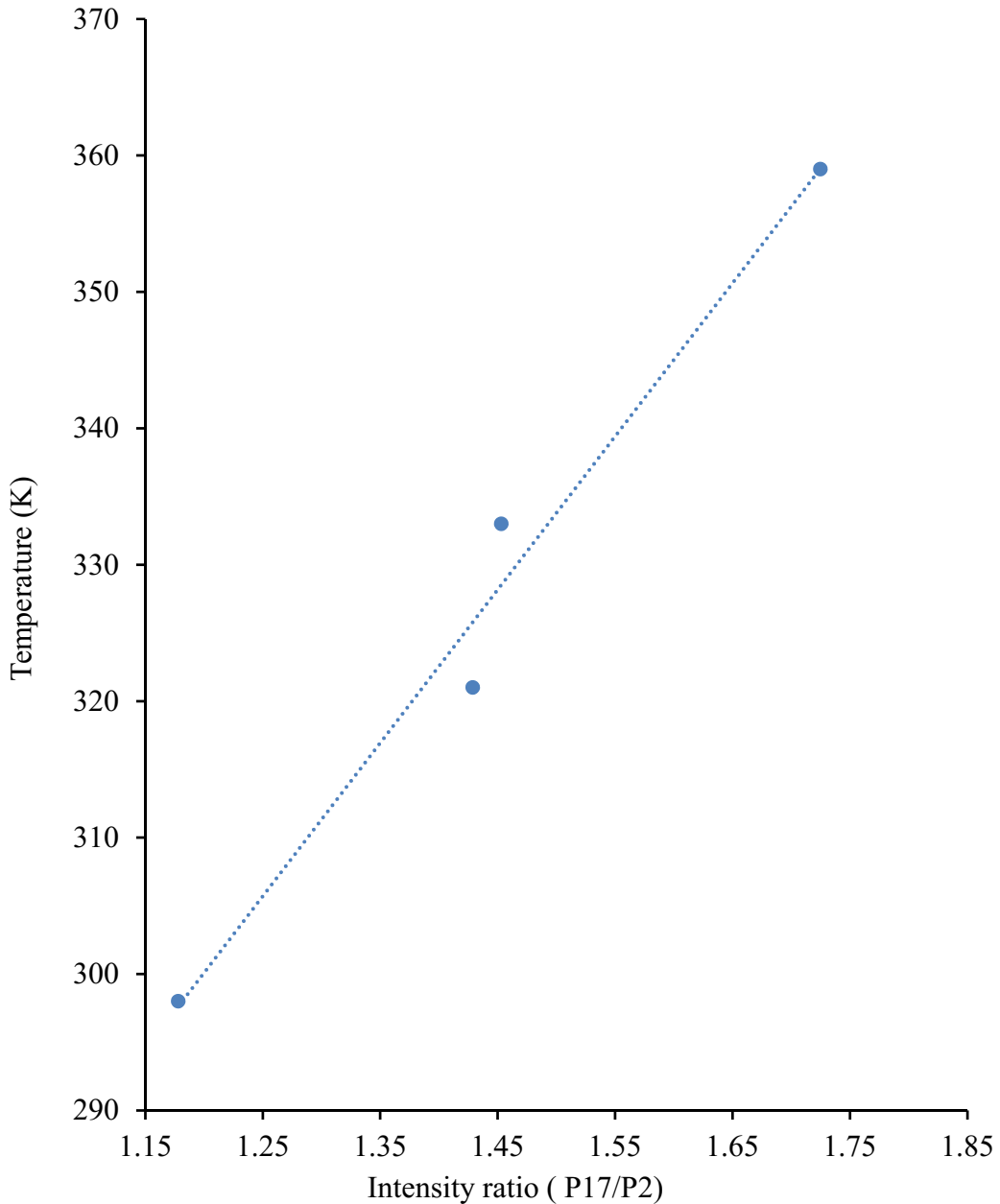


Figure 20. Plot of the ratio of intensity of the P17 and P2 versus temperature

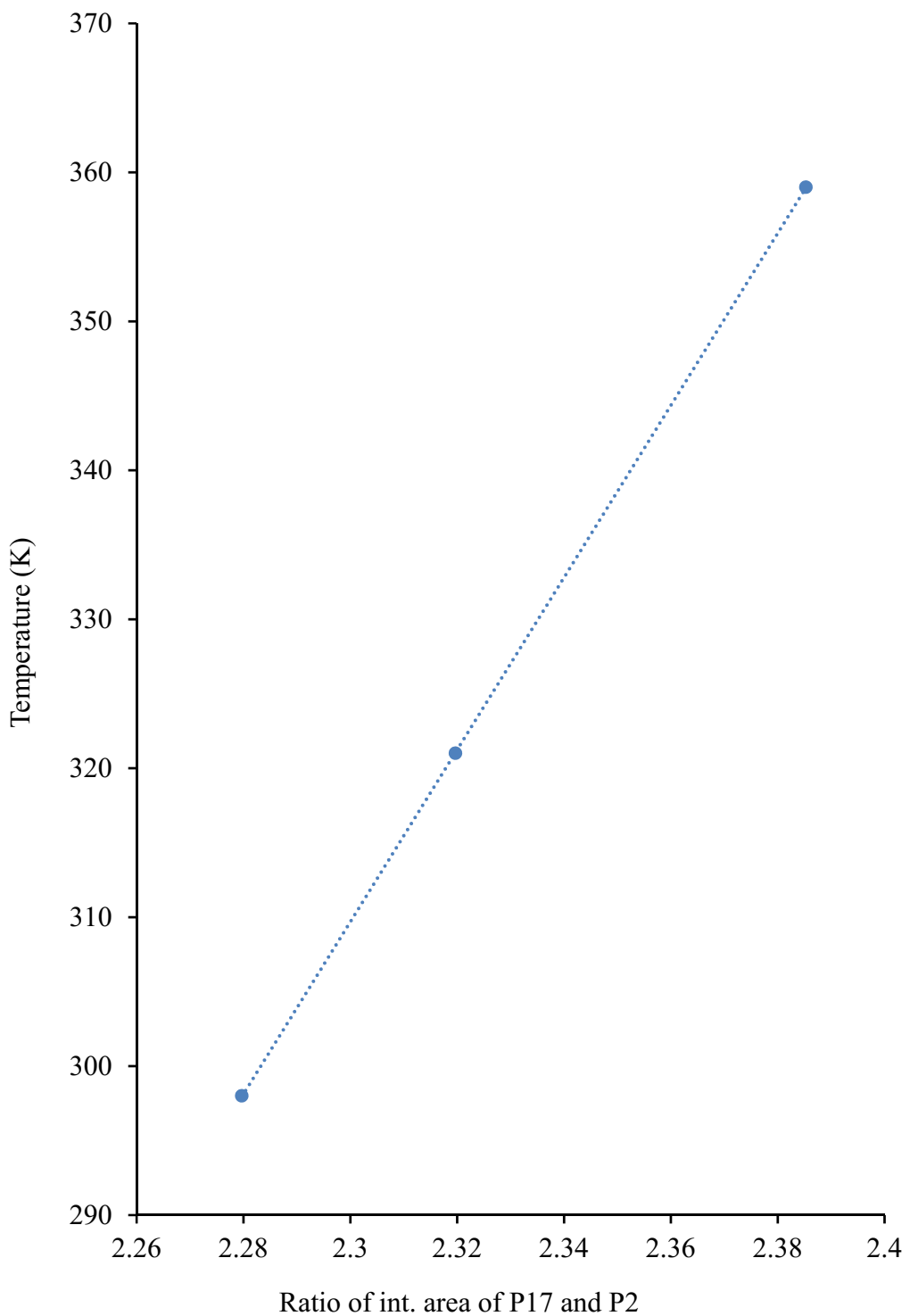


Figure 21. Plot of ratio of the integrated area of the P17 and P2 transitions versus temperature

1.4 Conclusions and Research Outlook

Oxygen temperatures in the range of 90–297 K have been determined by obtaining the A-band of O₂ and using this PS-CRD method with an optical cavity attached to a low temperature cryostat. We have also constructed an open-path (no windows) optical cavity using the PS-CRD technique as a temperature sensor. The A-band of oxygen was measured at several temperatures (298–373 K) with various flow rates of air, ranging from static no flow conditions to air flow up to 15 L/min. The temperature was obtained from a Boltzmann plot. For this plot, we consider the ^PP (lines with odd values of rotational quantum numbers (N) lines with value of N 5–17 because these lines are more intense, free from the interference of other absorption, and more sensitive to the temperature change. The same selected transitions were used to calculate all the temperatures above 297 K. The accuracy of the measurements was obtained by comparing the calculated temperatures with the temperatures measured with a sensor. The further validation of technique was done by comparing the result with simulated and two-line thermometry literature results.

The study has shown that the oxygen absorption is a very good choice to determine the temperatures in a flow system. Although it will be ideal to have a diode laser to resolve the peaks, the study has shown that a low-resolution spectrum is capable of giving the correct temperature of the flowing air. In our laboratory, the main application of the open-path PS-CRD absorption of oxygen is the possibility to measure the temperature of the output air flow cooling the blades of a laboratory turbine. This flowing air temperature sensor will be used to measure the local film temperature near the surface of a gas turbine airfoil under laboratory conditions. The protective film results on the surface from the mixing of the cooling air and the hot mainstream air flowing around the airfoil. By non-

intrusively measuring this turbulent film temperature, the heat transfer to the airfoil surface could be determined. This would be an important contribution for the development of efficient blade cooling technology. A low temperature CRD optical cavity, like the one described here, could provide laboratory data simulating conditions of pressure and temperature for planets and satellites of our solar system. A typical case is the atmosphere of Titan, a satellite of Saturn. At 140, 40, and 10 km of altitude, the atmospheric pressures are approximately 3,152, and 760 torr and the temperatures are 140,70, and 80 K, respectively [90]. The visible spectra of CH₄, C₂H₆, C₂H₂, C₂H₄, HCN, as well as C₃H₄, C₃H₈, C₄H₂, HC₃N can be obtained. Another application is related to the detection of atmospheric trace gases and their chemical reactions. In the lower atmosphere (troposphere) of earth, the air temperature falls with increasing altitude to reach a minimum of around 210 K between 10 and 16 km above sea level. It is possible to study in the laboratory the smallest concentrations of molecules such as NO₂, NO, NO₃, N₂O₅, O₃, HONO, and hydrocarbons simulating atmospheric conditions on Earth [91]. The observation of weakly bound complexes is possible with the low temperature CRD cell. The equilibrium distributions allow thermodynamic studies of the binding energies of the complexes [92].

CHAPTER TWO

2.1 Thermal Lens Spectroscopy(TLS)

2.1.1 *Thermal Lens Effect*

Thermal lens spectroscopy (TLS) is one of the most sensitive molecular absorption techniques among the photo-thermal methods. It depends upon the absorption and non-radiative decay of the energy. In this technique, molecules absorb the energy of the excitation beam (pump laser) which passes through the sample. The excited molecule relaxes through various radiative as well as non-radiative processes [93]. The non-radiative energy (heat) produces a significant amount of heat along the optical path, which results in a hot spot [94]. This hot spot has a different refractive index in comparison to its surroundings and acts as a lens. Most of the liquids show a positive coefficient of thermal expansion and negative temperature coefficient of the refractive index, which results in the formation of a diverging thermal lens. The formation of the thermal lens begins from the absorption of the energy and continues until the system reaches to thermal equilibrium through heat transfer. This effect is defined as the thermal lens effect.

Figure 22 shows the formation of the thermal lens and its effect on the intensity profile of a Gaussian beam. The formation of the thermal lens is observed by the dispersion of the probe beam, which is not absorbed by the samples. The divergence of the probe beam is observed beyond the sample cell as larger spot size or lower beam intensity [95,96]. The decrease of the intensity of the probe beam is proportional to the strength of the thermal lens formed.

2.1.2 Thermal Lens Signal (TLS)

The thermal lens signal is defined as [97,98]:

$$S = (\alpha_2 x_2 l) \left(\frac{1}{1+t_c/2t} \right) \left(-\frac{\partial n}{\partial T} \frac{1}{k} \right) \left(\frac{P}{\lambda} \right) (Y_H) \quad (18)$$

Where, the signal S is proportional to the sample absorbance ($\alpha_2 x_2 l$) with α_2 the absorption coefficient, X_2 the mole fraction of the solute, l (10cm) the optical path length and the second term in parenthesis($1/(1 + t_c/2t)$).The beam radius at the center of the cell is $w_0 = 0.030\text{cm}$. The characteristic time constant ($t_c = w_0^2 2\rho C_p / 4k$) depends on w_0^2 , the density (ρ), the thermal conductivity (k), and molar heat capacity (C_p) of the solvent. The time (t) is related to the modulation frequency of the pump laser, which in our case is in the range of 1-5 Hz. The signal magnitude is directly proportional to the negative temperature gradient of the index of refraction ($-\partial n/\partial T$) and inversely proportional to the thermal conductivity (k).

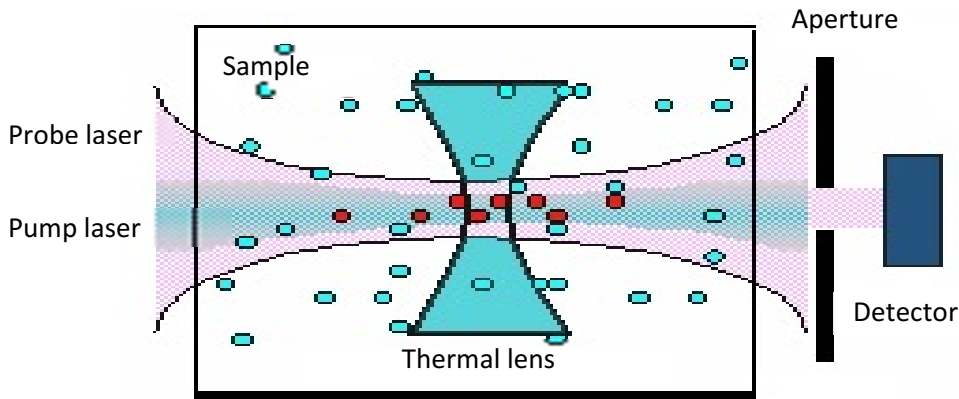


Figure 22. Formation of thermal lens

The signal S is also dependent on the power of the pump laser (P) at wavelength (λ). The last term in the parenthesis of equation 1 is the heat or energy yield (Y_H). This term is related to the energy transfer mechanism from the molecule that absorbs the pump

laser to the solution and its magnitude is still unknown for the fifth vibrational overtone of the C-H.

2.1.3 *Laser Beams Configuration on Thermal Lens Spectroscopy*

The TLS technique was discovered by Gorden et al. in 1965 when they were attempting to enhance the intensity of the Raman scattering from benzene with a single beam He-Ne laser at Bell Laboratory [99]. Grabiner et al. [100] later decided to use mode-matched dual beam configuration in which both beams have the same waist at the center of the cell. They used a Q-switched CO₂ laser as an excitation source and a He-Ne laser as a probe to measure the vibrational relaxation rates in polyatomic molecules. Over the time, Hu and Whinnery [101,102] improved the sensitivity of the TLS technique by using mode-mismatched dual-beam configuration, where the two beams have different waists. In our lab, we have been using mode-mismatched dual-beam configuration to study a high overtone transition of very weak absorptions. Figure 23 depicts the configuration of the pump and probe beams. The pump beam is focused at the center of the sample cell, and the probe beam is arranged to be at a distance $Z_1=1.73Z_{cp}$, where Z_{cp} is the confocal distance of the probe beam and Z_1 is the distance between the probe beam waist and the pump waist. In literature, there are several configuration models of the TLS technique have been used. Some models of the thermal lens effect with pulse [103-105] and modulated excitation [107,108], transverse [105] and collinear configuration [109-112]and stationary [113] and flowing media [114,115] are reported. They are being used to study the various phases of the sample like, liquid, solid [105] and gas [104].

The TLS signal depends upon the excitation power and the thermo-optical properties of the solvent (equation 18).

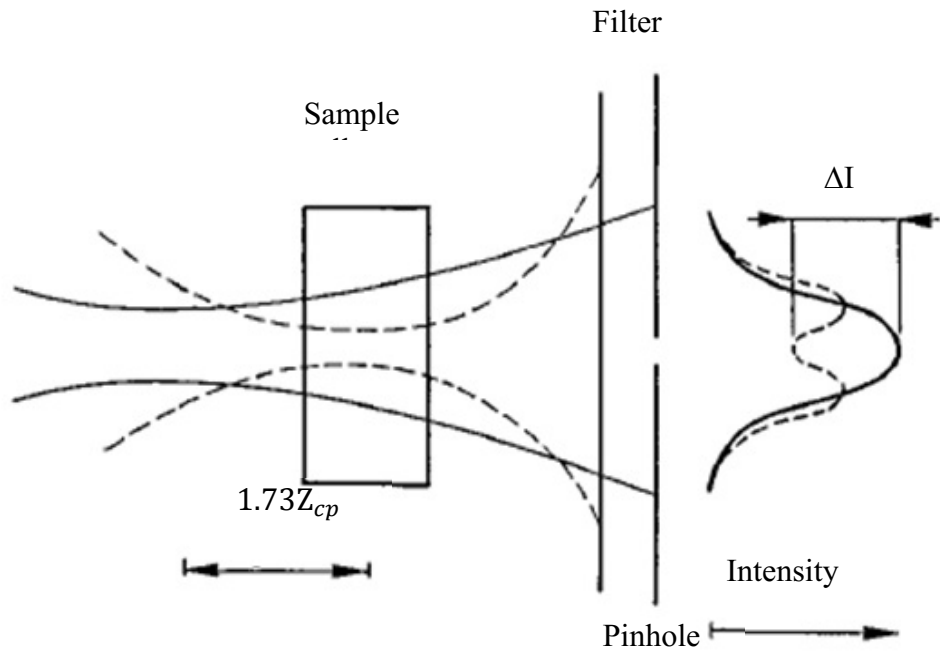


Figure 23. Pump and probe beam configuration on mode-mismatched dual-beam TLS technique

Various researchers are trying to increase the sensitivity of the TLS technique by increasing the excitation power, but there is a limit of the excitation power. If the power exceeds the limit, this causes optical saturation (optical bleaching) which results in diminishing the sensitivity of the technique. In this project, we were focusing on other possible ways to increase the sensitivity of the technique.

2.2 Experimental Method and Procedure

In order to accomplish our projects, we used mode mismatched dual beam collinear configuration of the thermal lens spectrometer. Figure 24 depicts the actual experimental set-up, which comprises of a tunable continuous-wave (cw) Coherent dye laser model CR-599 for excitation beam. The dye laser was pumped by an argon ion laser, Spectra Physics,

model Stabilite 2017, with a wave length of 514 nm. The stepper motor was used to scan a dye laser in the range of the Rhodamine 6G dye from 15800 cm^{-1} to 17400 cm^{-1} . The stepper motor is remotely controlled by a computer with LabVIEW 2013 software. A small fraction of the excitation beam which is modulated at 250 Hz with Stanford Research System (SRS) mechanical chopper (model SR 540), is detected with a photo-sensor (Newport, Model 882), and sent to a lock in amplifier (Ithaco 3962A). On the other hand, the main excitation beam is modulated by a low frequency optical shutter (Electro-Optic CH-60). The shutter is operated with a function generator (BK Precision, Model 3011A) with the frequency 1 to 5 Hz range. The modulated excitation beam is focused at the center of the 10 cm sample cell. The spot radius and confocal distance of the beam at that position are 0.030 and 51 cm respectively. The Spectra Physics laser model 177-G7205 with multiple wavelengths is used to get a continuous wave probe beam. A prism is used to separate a single wavelength (488 nm) which is used as a probe beam. The excitation and probe beam are overlapped with a blue dichroic filter and propagate collinearly through the cell. An interference filter is used to block the excitation beam and transmit the probe beam. Any residual transmission of the excitation beam is removed by placing a blue glass filter very close to the detector. At the end, the probe beam is passed through pinhole with 20 μm in diameter and its intensity is recorded with a photomultiplier tube (GCA McPherson, model EU-701-93). The detector is installed on x, y and z stage which allows the precise location of signal and intensity maximization. After the detector, a signal is pre-amplified with a SRS low noise pre-amplifier (model SR 560). Finally, the signal is sent to another single-phase lock-in amplifier (Ithaco 3962 A). The normalization of the signal is accomplished by dividing the probe signal output by the excitation beam signal.

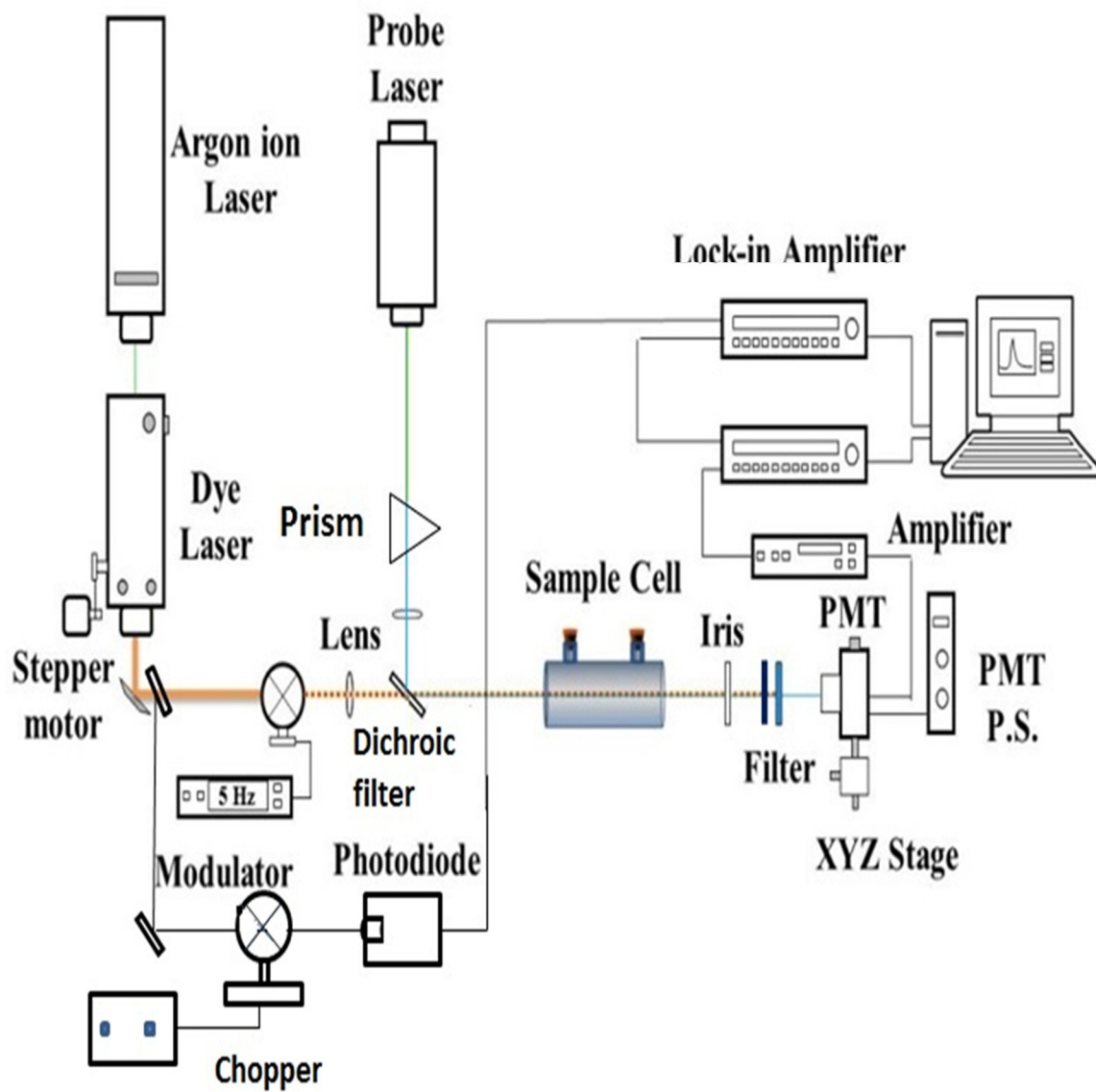


Figure 24. Experimental setup of thermal lens spectrometer

The LabVIEW 2013 software is used as an interface for the several processes such as, data acquisition, processing and plotting. At the end, a normalized thermal lens signal as a function of the wavenumber is obtained.

2.2.1 Concentric Alignment of the Excitation and Probe Beam

The measurement of the signal begins with turning on both the pump and the probe laser and allow them to warmup. The pump laser wavelength close to the place of maximum absorption of the sample is selected. The concentric alignment of the excitation and probe beam is obtained. If the alignment is not good, we could observe a fraction of the signal intensity or no signal at all. Therefore, accurate alignment is critical during the experiment. In order to make an alignment easy and convenient, the optics like mirror, lenses, and filters are mounted on translational stages which allow the displacement of the beams in x, y, and z directions. Far-field alignment is monitored by observing the beam spots three meters from the sample cell. In our experimental setup, the spot size of the probe beam is made larger than the excitations, but both beams have a common center.

2.2.2 Complete Blocking of Excitation Laser

It is necessary to make complete blocking of the excitation beam before PMT. It avoids the problem of highly erratic signals which obscure the TLS signal. The complete blocking was obtained by using both interference and glass filters.

2.2.3 Observations of TLS Signal on Oscilloscope

First, it is better to observe the TLS signal on oscilloscope. For that, the wavelength of excitation laser at the place of maximum absorption of sample was selected. The modulated excitation beam was focused at the center of the cell and nearly three times

larger size unmodulated probe beam was focused at the point where the TLS signal amplitude is maximum. The modulation of the excitation beam was obtained by a low frequency shutter (Electro-optical products CH-60). It was operated by function generator (SRS DS345) with square wave 4 V amplitude and frequency 0.5 to 10 Hz range. We can observe the TLS signal on the oscilloscope in reference with the signal from the function generator. The TLS signal was optimized with the proper aligning of the center of the probe beam with a pin hole of the detector.

2.2.4 Normalization of TLS Signal

The TLS signal depends upon the excitation power which gets changed throughout the scanning region. So, the signal must be normalized. A small fraction of the excitation beam modulated at 250 Hz with Stanford Research System (SRS) mechanical chopper model SR 540 was detected with a photo-sensor (Newport, Model 882) and sent to a lock in amplifier (Ithaco 3962A). The lock- in amplifier locks the voltage signal with respect to the reference signal from the chopper. On the other side, the probe beam modulated with the periodic formation of thermal lens was measured with a photomultiplier tube (PMT, GCA McPherson EU-701-93) which was operated at 1000 kV. The normalization of the signal is accomplished by dividing the probe signal by the excitation beam signal.

2.2.5 Signal to Noise Ratio Improvement

First, the signal from PMT was fed to a low-noise preamplifier (Stanford Research, SR-560). A $50\ \Omega$ cap was connected to the feeding terminal, which avoids the high voltages that might leak from the detector. The noise was reduced through the cut-off filter 0.03 to 30 Hz on the preamplifier. The signal to noise ratio was improved by selecting AUTOSET

on the main panel of the lock-in amplifier which provides the optimum values for the various parameters like: time constant, sensitivity, dynamic range. If it is necessary, we can adjust the instrumental parameters at any time. Intense TLS signals require sensitivities up to 1V, while weak signals only require 300 μ V. The value of time constant depends on noise levels; a value of 1s is characteristic of low-noise samples, while a value of 3s reflects a noisy signal. Table 11 shows the various instrumental parameters used for optimization of the TLS signal. Those would be different for different conditions.

Final maximization of the TLS signal, was achieved by small increment of the position of the detector in x, y, and z direction. The procedure requires alternative movement of the y and z direction to get the place of maximization. In general, mapping time based on the TLS signal intensity. For example, the concentrated samples generate intense signals and require less mapping time and vice versa. Once we found the maximum strength, it is recommended to do an AUTOSET or at least an AUTOPHASE one more time to update instrumental parameters to the current level of intensity.

2.2.6 Acquisition of Spectra

Once the TLS signal was optimized, the spectral data were acquired by using a LabVIEW interface. The details of the program are presented in appendix A. however, the general features are provided here. At first, the calibration chart was required to correlate the micrometer positions of the birefringent filter with the corresponding wavelengths. Second, the stepper motor was turned on, and initial wavelength was selected by moving the micrometer screw on the dye laser. A belt was used to connect the rotating wheel on the micrometer screw to the shaft of the stepper motor.

Table 11. Parameters for Optimization of the TLS Signal

Parameters	Values
Time constant for pump laser signal	10 s
Time constant for probe laser signal	30 s
Sensitivity for pump laser signal	300 mv
Sensitivity for probe laser signal	100 mv
Cut off filter	0.1 to 10 Hz
Gain on preamplifier	5×10^4
Step size	0.404 μ m
Pause	2 s

The LabVIEW file was opened, and the step-size, acquisition pause, as well as final and initial micrometer positions were specified. On the control panel, the MOTOR button was showing the stepping action. Right before running the program, linear averaging was activated by pressing the OFFSET key on the lock-in amplifier and appropriate values for time constant was selected.

The run button started the data acquisition, which might be completed by 25 min for low frequency experiments. At the end, the program allows the observation of the TLS

spectrum, which is a plot of strength of TLS signal versus wavenumber. Now, the spectrum can be saved by pressing the SAVE button. At that time, a dialog box will appear where the file name must be specified. The stop sign marks the end of a scan and allows for new data acquisition. Generally, to acquire the quality spectra, the above procedure was carried out at least three times for each sample and the average spectrum was obtained.

2.2.7 Experimental Shutdown

Normally, the process of shutdown is reverse of the startup. At first, close the shutter of the PMT and turn off the electronics in the following order: voltage supply of the PMT, preamplifier, lock-in amplifier, shutter driver, function generator, chopper, and stepper motor. Turn off the lasers according to their shutdown procedures, making sure to allow cooling before switching off the power. Next step is emptying the cell.

2.3 Non-linear Thermal Lens Signal of the ($\Delta\nu = 6$) C-H Vibrational Overtone of C_6H_6 in Liquid Solutions of n - C_6H_{14} and CCl_4

In this project, we basically focused on the study of ringed compounds. The molecules are not only the possible molecules present on the lakes of the Titan (a satellite of Saturn) but also biologically interesting compounds. Unsaturated ring compounds are present in the biological molecules like proteins, nucleic acids and amino acids.

Our group is very interested in the laboratory experiments to simulate the composition of lakes of Titan where the major components, liquid methane and ethane act as solvents at temperature around 95 K [116-118]. The ultimate goal of our investigation is to determine the solubility of unsaturated hydrocarbons in liquid methane and ethane at the surface temperature of Titan. However, it's very costly and challenging to perform the experiment at cryogenic temperature without having the basic information about the

solubility of the compounds, solvent interference and the suitability of the technique. Therefore, it is good to know such basic information before doing the experiment at cryogenic temperatures. So, in this experiment we test the suitability of our TLS technique for that purpose. To avoid the solvent interference on TLS spectrum of interested molecule, we want to study the high energy ($\Delta\nu = 6, 7\dots$) C-H or O-H vibration transitions overtone spectrum.

The thermal lens signal of the fifth ($\Delta\nu = 6$) C-H overtone of pure liquid benzene at room temperature was obtained by using a quartz cell of 10 cm path length. The power of the excitation beam and probe beam were 54 mW and 1 mW respectively. The beam was modulated at a frequency of 1 Hz. The maximum intensity of signal is localized at 16480 cm^{-1} with a band width (FWHM) of 250 cm^{-1} . Both of the parameters are in agreement with the literature values [119,120]. The peak absorption coefficient of pure benzene has been reported [119] as $(2.2 \pm 0.3) \times 10^{-3}\text{ cm}^{-1}$. C-H fifth vibrational overtone spectrum of benzene is detected at room temperature for compositions per volume in the range 1 to 1×10^{-4} using CCl_4 and $n\text{-C}_6\text{H}_{14}$ as solvents. By detecting the absorption band in a 100 ppm solution, the peak absorption of the signal is approximately $(2.2 \pm 0.3 \times 10^{-7}\text{ cm}^{-1})$. Figure 25 and figure 26 show the several spectra of the thermal lens signal of the fifth ($\Delta\nu = 6$) C-H overtone transition of benzene in CCl_4 and n -hexane solutions respectively. The concentrations of benzene vary from (0.1 to 1×10^{-4}) composition by volume in CCl_4 and (0.2 to 1×10^{-4}) in n -hexane. In case of the solvent CCl_4 the spectrum becomes narrower and symmetric with decrease in concentration of benzene. This is not the case for benzene in $n\text{-C}_6\text{H}_{14}$ as solvent.

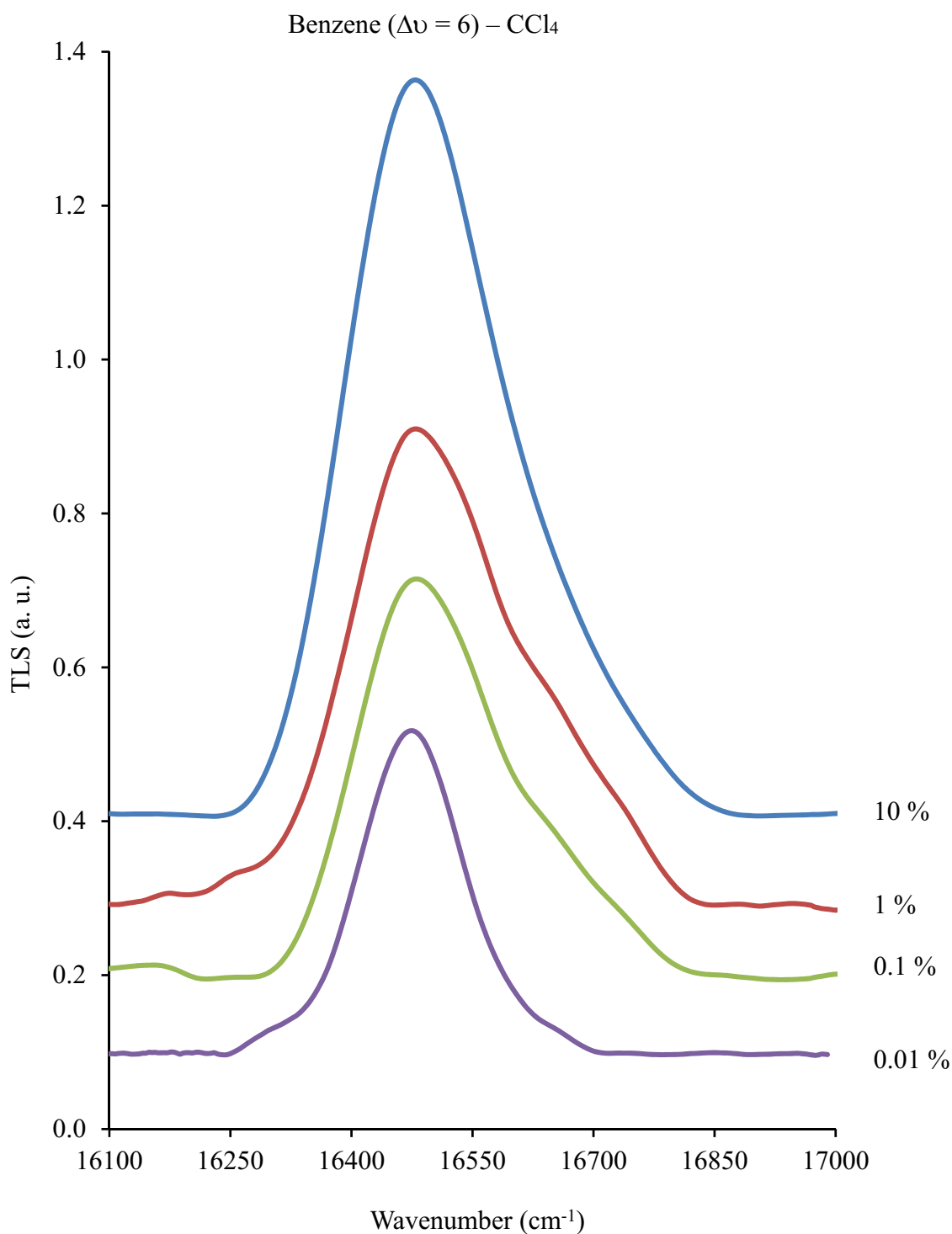


Figure 25. Thermal lens spectra of the C-H vibrational overtone ($\Delta\nu = 6$) of benzene solutions in CCl₄ with various compositions by volume at 295 K

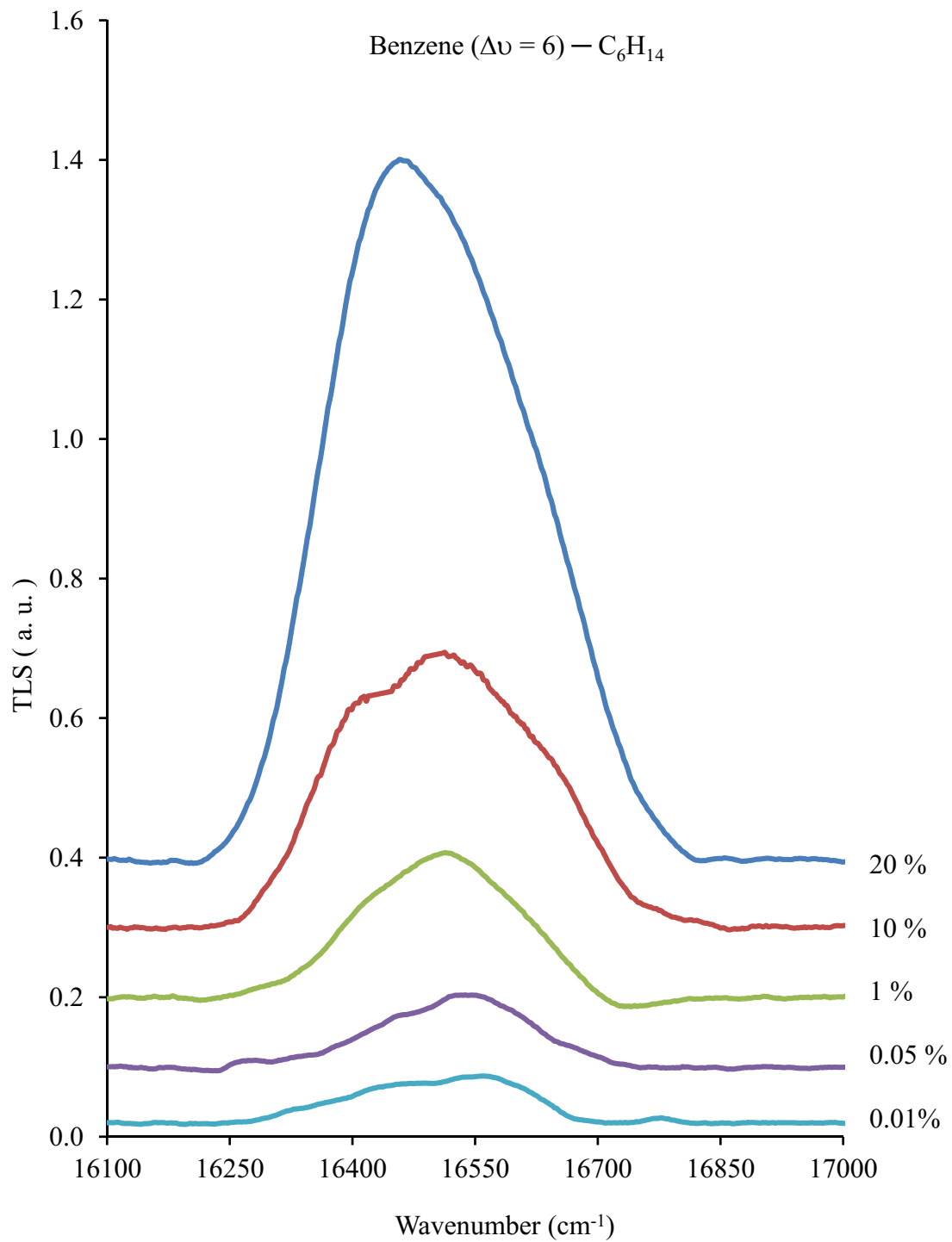


Figure 26. Thermal lens spectra of the C-H vibrational overtone ($\Delta\nu = 6$) of benzene solutions in n-C₆H₁₄ with various compositions by volume at 295 K

2.3.1 Solvent Enhancement in C₆H₆-CCl₄ and C₆H₆-n-C₆H₁₄

In thermal lens experiments, the solvent enhancement has been defined as:

$$(-\frac{\partial n}{\partial T}) \frac{1}{k} \left(\frac{P}{\lambda}\right) = g(x_2) \left(\frac{P}{\lambda}\right) \quad (19)$$

The pump power (P) at the maximum of absorption (λ) is fixed but can be altered to increase the sensitivity of the system. In thermal lens, magnitude of signal is directly proportional to the negative temperature gradient of the index of refraction ($-\partial n / \partial T$) and inversely proportional to the thermal conductivity (k). Some researchers have enhanced the thermal lens signal by preparing solutions with high negative temperature gradients of index of refraction ($-\partial n / \partial T$) using electrolytes and making low values of thermal conductivity (k) using surfactants [121]. However, the electrolytes provided only 2-fold enhancement of the signal, while surfactants provided up to an 8-fold enhancement.

The $g(x_2)$ factor is usually obtained for the solvent but in our case, it was calculated as a function of the solute composition. The C₆H₆-CCl₄ and C₆H₆-n-C₆H₁₄ solutions are considered ideal solutions for the numerical calculation. Assuming that the index of refraction (n) of the solution can be obtained with the Lorentz-Lorenz equation [122,123]

$$\left(\frac{n^2 - 1}{n^2 + 2}\right) \frac{1}{\rho} = \left(\frac{n_1^2 - 1}{n_1^2 + 2}\right) \frac{x_1}{\rho_1} + \left(\frac{n_2^2 - 1}{n_2^2 + 2}\right) \frac{x_2}{\rho_2} \quad (20)$$

The equation for the index of refraction derived by Heller [124] is:

$$n = \left(\frac{2A+1}{1-A}\right)^{1/2} \quad A = \left[\left(\frac{n_1^2 - 1}{n_1^2 + 2}\right) \frac{x_1}{\rho_1} + \left(\frac{n_2^2 - 1}{n_2^2 + 2}\right) \frac{x_2}{\rho_2} \right] \quad (21)$$

The density (ρ), the coefficient of the thermal expansion (β), and thermal conductivity (k) of the ideal solution are given by:

$$\rho = \rho_1 + (\rho_2 - \rho_1)x_2 \quad (22)$$

$$\beta = \beta_1 + (\beta_2 - \beta_1) \quad (23)$$

$$k = k_1 + (k_2 - k_1) \quad (24)$$

$$C_p = C_{p,1} + (C_{p,2} C_{p,1}) x_2 \quad (25)$$

The terms $n_1; \varrho_2; \beta_1$ and $C_{p,1}$ refer to the solvent (CCl_4 or $\text{n-C}_6\text{H}_{14}$) and n_2, ϱ_2 β_2 k_2 and $C_{p,2}$ refer to the solute. Table 12 presents numerical values of the index of refraction, temperature dependence of the index of refraction [125-127], thermal conductivity [128,129], coefficient of thermal expansion [130], and heat capacity at constant composition of solute (x_2). The partial derivative of (equation 21) with respect to the temperature at constant pressure is:

$$\left(\frac{\partial \eta}{\partial T}\right)_p = \frac{3}{2(2A+)^{1/2} (1-A)^{3/2}} \left(\frac{\partial n}{\partial T}\right)_p \quad (26)$$

$$\left(\frac{\partial n}{\partial T}\right) = A_1 x_1 + A_2 x_2 \quad (27)$$

$$A_i = \left(\frac{\varrho}{\varrho_1} \left(\frac{\partial}{\partial T} \left(\frac{n_i^2 - 1}{n_i^2 + 1} \right) \right)_p + \left(\frac{n_i^2 - 1}{n_i^2 + 1} \right) \left(\frac{\partial}{\partial T} \left(\frac{\varrho}{\varrho_i} \right) \right)_p \right)_{i=1,2} \quad (28)$$

$$A_i = \frac{\varrho}{\varrho_i(n_i^2 + 2)} \left(2n_i \left(\frac{dn_i}{dT} \right) \left(1 - \frac{n_i^2 - 1}{n_i^2 + 1} \right) + (n_i^2 - 1)(\beta - \beta_i) \right) \quad (29)$$

In this equation, the variation of the density with temperature at constant pressure has been replaced by the product of the density (ϱ) and the coefficient of thermal expansion (β) of the solution, as well as the corresponding $\beta_i \varrho_i$ of the solute and the solvent. The function $g(x_2)$ is defined multiplying above equation by (-1/k):

$$g(x_2) = -\frac{1}{k} \left(\frac{\partial n}{\partial T}\right)_p = -\frac{3}{2k(2A+)^{1/2}(1-A)^{3/2}} (A_1 x_1 + A_2 x_2) \quad (30)$$

The function $g(x_2)$ is positive because $(\partial n / \partial T)$ is negative. The product function: $(p/\lambda) * g(x_2)$ is called the solvent enhancement factor.

We calculated the solvent enhancement factor in both solvent CCl_4 and $n\text{-C}_6\text{H}_{14}$. Table 12 shows the parameters that we applied to calculate the solvent enhancement factor and the actual pure solvent enhancement factor of the compounds. Figure 27 shows the numerically calculated values of the solvent enhancement factor $g(x_2)$ from Eq.30 as a function of the composition of benzene (x_2) in carbon tetrachloride and n -hexane. The calculation shows that the solvent factor (enhancement) increases as the composition of solute decreases in CCl_4 as solvent. For C_6H_6 in $n\text{-C}_6\text{H}_{14}$ shows that the solvent $n\text{-C}_6\text{H}_{14}$ has no effect in enhancement, in fact the solvent enhancement factor decreases slightly when the composition of C_6H_6 decreases. As predicted from the solvent enhancement calculations for C_6H_6 in CCl_4 and C_6H_6 in $n\text{-C}_6\text{H}_{14}$ (Table 12 and Figure 27), the comparison of the bands at the same composition give the larger signal to the CCl_4 solution (Figure 25).

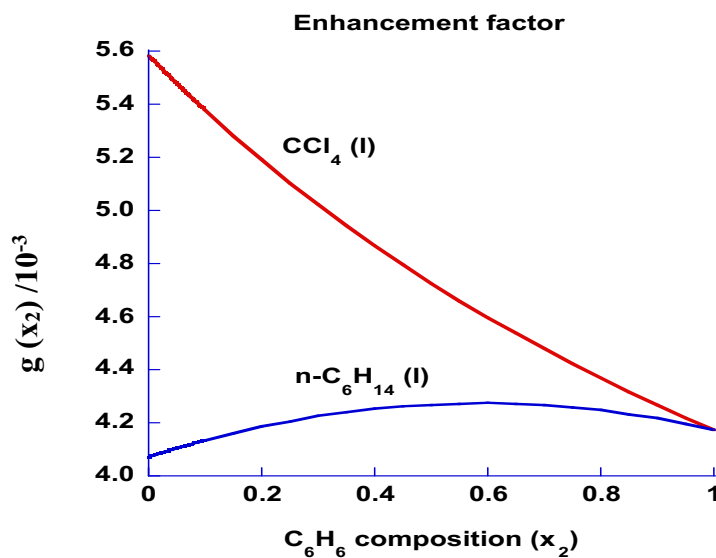


Figure 27. Numerical calculation of the solvent enhancement factor (g) as function of the composition of benzene (x_2) in $n\text{-C}_6\text{H}_{14}$ (bottom) and CCl_4 at the top

Table 12. Thermophysical Properties of Liquid C₆H₆, CCl₄, and n-C₆H₁₄ at 295 K

Physical properties	Symbols	C ₆ H ₆	CCl ₄	n-C ₆ H ₁₄
Index of refraction	η	1.5005	1.4595	1.372
Negative temperature gradient of the index of refraction	$-(\delta\eta/\delta T) (K^{-1})$	0.00066	0.00058	0.00056
Molar density	ρ (mol cm ⁻³)	0.01122	0.01036	0.0076
Thermal conductivity	k (W m ⁻¹ K ⁻¹)	0.15813	0.10385	0.13753
Coefficient of thermal expansion(vol.)	β (K ⁻¹)	0.00125	0.00122	0.00138
Heat capacity at constant pressure	C_p (J mol ⁻¹ K ⁻¹)	136.1	131.75	192.63
Solvent factor(enhancement)	$(-\delta\eta/\delta T)/k$ (m/W)	0.00417	0.00558	0.00407
Thermal time constant	t_c (s)	0.22	0.30	0.24

2.3.2 Comparison of Experimental Signal with Calculated Signal

We calculated the integrated area of each spectral band of various composition of benzene in CCl₄ and n-C₆H₁₄ and normalized with the integrated value of pure liquid

benzene. Tables 13 and 14 shows the actual and normalized integrated values of area for various compositions of benzene in n-C₆H₁₄ and CCl₄, respectively.

Table 13. Integrated Area of the TLS Spectrum of ($\Delta\nu = 6$) C-H Overtone of Benzene in n-C₆H₁₄

Benzene composition (x ₂)	Integrated area	Normalized signal
0.0001	12.717	0.027
0.0005	17.87916	0.03796
0.005	28.98063	0.06153
0.01	38.151	0.081
0.02	47.92425	0.10175
0.1	82.425	0.175
0.2	122.46	0.26
0.4	205.0263	0.4353
0.6	300.2154	0.6374
1	471	1

Table 14 Integrated Area of the TLS Spectrum of ($\Delta\nu = 6$) C-H Overtone of Benzene in CCl₄

Benzene composition (x ₂)	Integrated area	S (normalized)
0.0001	70.9	0.150531
0.001	122.8	0.260722
0.01	162.2	0.344374
0.1	194.9	0.4138
1	471	1

The thermal lens signal $x_2 \times g(x_2) \times [1/(1+t_c/2t)]$ was calculated numerically for the C₆H₆-CCl₄ solutions. In order to make a comparison of numerically calculated values of signal with the experimental values, the calculated signal (S) was normalized by using the integrated value of the experimental band of pure benzene as normalized for all the experimental bands of various compositions of benzene in CCl₄. Figure 28 shows the result of the calculation as a function of x₂ (red line). The experimental points are the full circles connected by broken blue lines. It is clear that the experimental results are not simulated by the product function that is linearly varies with concentrations. The figure also shows a non-linear behavior of the experimental results.

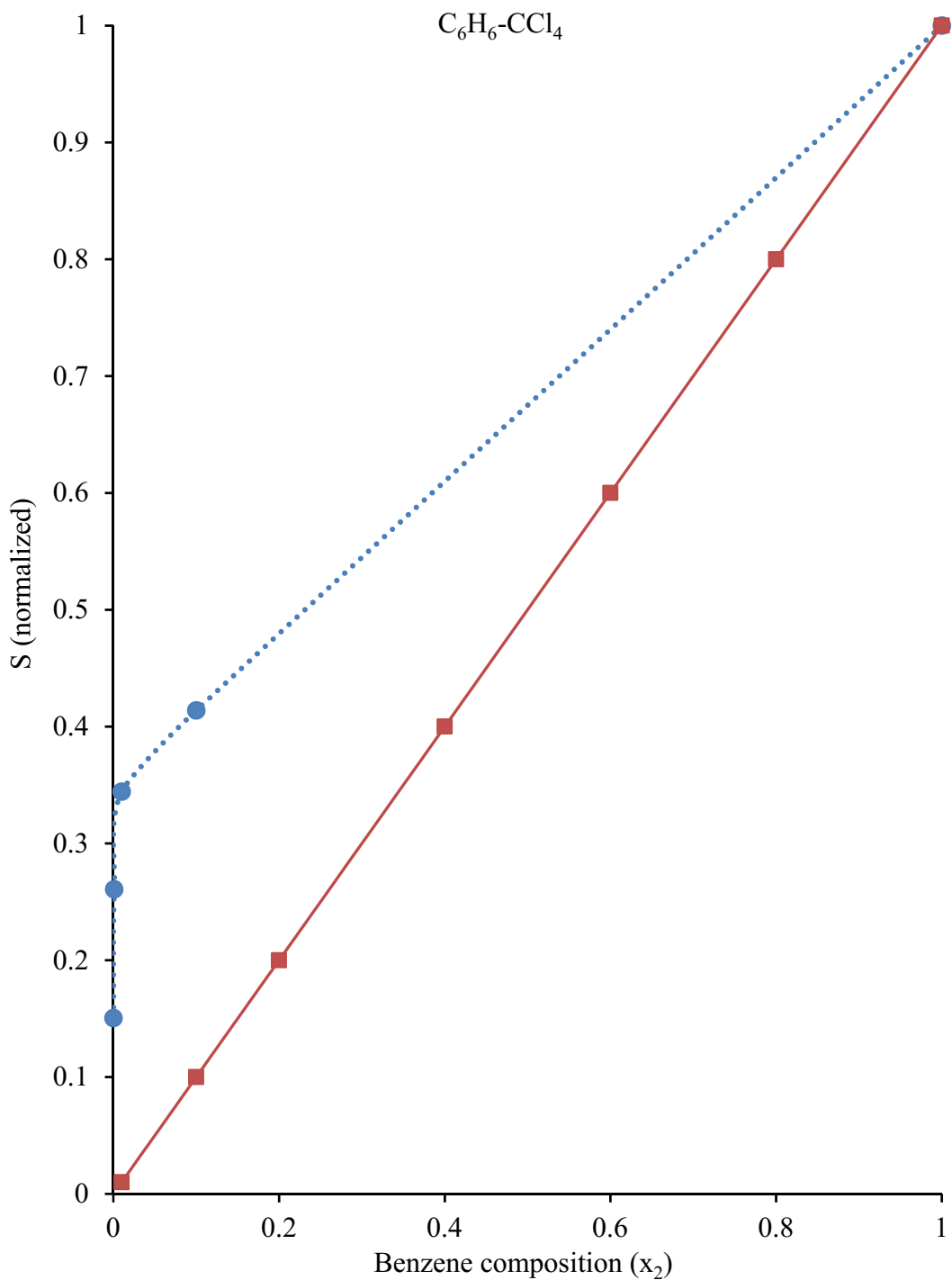


Figure 28. Comparison of predicted thermal lens signal (straight line) with the experimental thermal lens signal (non-linear) as function of the composition of benzene in CCl_4

2.3.3 Two-color Excitation Model

In our laboratory's previous investigation, the TLS signal was enhanced by using three different laser beam configurations in which two beams acts as excitation and one beam as a probe [131]. The signal enhancement was obtained by two color excitation model in which simultaneous absorption of two different kinds of photons occurs. One excitation beam was used for the vibrational excitation, and the other was used for the electronic transition of the vibrationally excited molecules.

Recently, we started focusing on the two-color excitation model in which simultaneous absorption of excitation and the probe lasers occur. The two-color excitation process not only improved the sensitivity of the technique by the two orders of magnitude, but also generated the non-linearity of TLS signal of ($\Delta\nu = 6$) C-H overtone transition of benzene below the composition of 1% by volume. This signal enhancement and non-linearity cannot be explained by the solvent enhancement factor. In order to explain the non-linearity, a two-color absorption model was developed which reflects the experimental signal. The principle behind this model is as follows:

The change in the magnitude of the experimental TLS signal below 1% composition by volume represents the non-linear behavior. A possible explanation is based on the fact that the total thermal lens signal is the sum of the two terms: a linear plus a non-linear contribution. For one color absorption, the power of the transmitted signal (P_{trans}) is given by:

$$P_{\text{trans}} = P e^{-\alpha_2 x_2 l} \quad (31)$$

where, P is the laser power, α_2 is the absorption coefficient of the overtone transition ($\Delta\nu = 6$) of C-H, x_2 is the composition by volume and l is the length of the cell. The power absorbed (P_{abs}) that contributes to the thermal lens signal is given by [98]:

$$P_{\text{abs}} = P - P_{\text{trans}} = P(1 - e^{-\alpha_2 x_2 l}) \quad (32)$$

If the molecule simultaneously absorbs photons from the pump and probe laser the power absorbed for the electronic transition is:

$$P'_{\text{abs}} = P'(1 - e^{-\beta_2 x_2 l}) \quad (33)$$

In this case, β_2 is the absorption coefficient for an electronic transition and P' is a combined power absorption whose magnitude is not known. The total thermal lens signal S is:

$$S = G(P(1 - e^{-\alpha_2 x_2 l}) + P'(1 - e^{-\beta_2 x_2 l})) \quad (34)$$

In this equation 34, the parameter G represents all the other terms shown in equation of the thermal lens signal (equation 18) except for the power and the absorption term. Since $e^{-\alpha_2 x_2 l} = 1 - \alpha_2 x_2 l$ for small $\alpha_2 x_2 l$ ($\Delta\nu = 6$ overtone transition) and taking power as a common factor, eq.34; can be written as:

$$S = GP(\alpha_2 x_2 l + C(1 - e^{-\beta_2 x_2 l})) \quad (35)$$

The constant C is the ratio P'/P . It is assumed that electronic absorption coefficient (β_2) is larger in magnitude than the absorption coefficient (α_2) of the overtone transition. In this case, for compositions larger than 1%, the exponential term that contains $(\beta_2 l)$ in equation is very small compared to l and the second term can be considered part of the thermal background (C). For small composition (in our case below 1%), the first term $\alpha_2 x_2 l$ is negligible, but the entire second term becomes an important function of the concentration and non-linearity on TLS signal occurs.

Figure 29 depicts a plot of normalized thermal lens signal versus composition of benzene in n-hexane for the ranges of concentration (0.0-1.0). Figure 30 presents the detail at low ranges of concentration (0.0-0.2). In the solvent n-C₆H₁₄, we obtained the excellent fit of those ten experimental points over the entire range of composition of (0.0-1.0) in figure 29 and the points are represented by a function:

$$S = 0.029 + 0.919x_2 + 0.050(1 - e^{-184x_2}) \quad (36)$$

S is the total normalized signal and x₂ is the composition of benzene in n-hexane. Because of the fact that above function is a fit of ten experimental points over three orders of magnitude concentrations, it is reasonable to except that the function has a constant term (different from zero) as an intercept. The line in figure 29 shows the agreement between experimental points and function of equation 36. The general results are in agreement with this simple model.

Here we observed that the TLS signal linearly varies with concentrations above 1% composition of benzene by volume. At higher values of x₂, the function is predominantly a single photon absorption (the second part of the equation 36) and the contribution from the two color absorption (from the last part of the function) is negligible since it is only present in the form of a constant background thermal signal.

At the concentration below 1 % of benzene, the last term of equation 36 becomes importantly prominent and is responsible for non-linearity and the enhanced thermal lens signal. The enhancement at composition below 1% comes from the fact that there is more thermal energy released by the electronic transition.

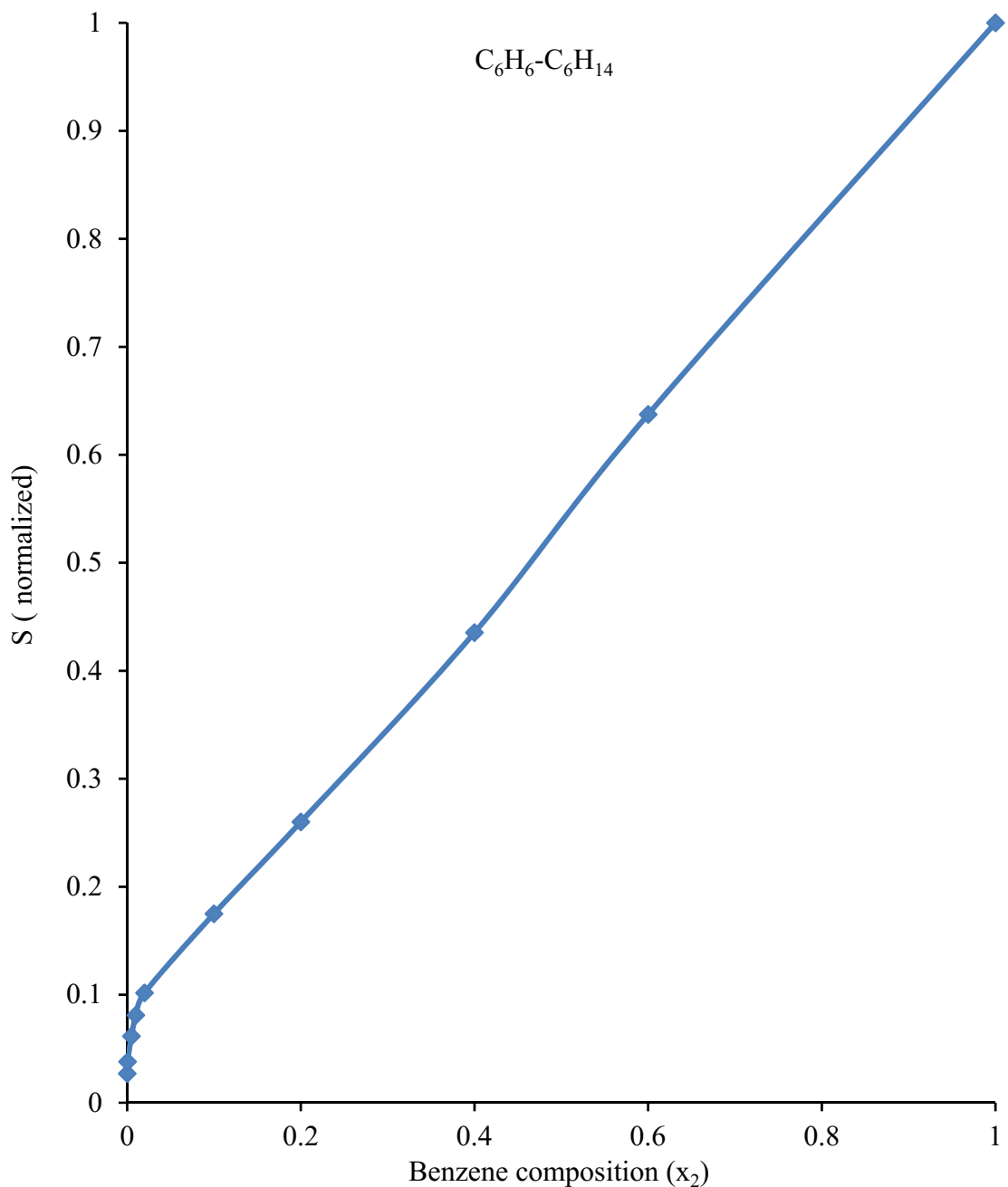


Figure 29. Normalized experimental thermal lens signal as a function of composition of benzene in $n\text{-}C_6H_{14}$ for the range (0.0-1.0) at 295 K

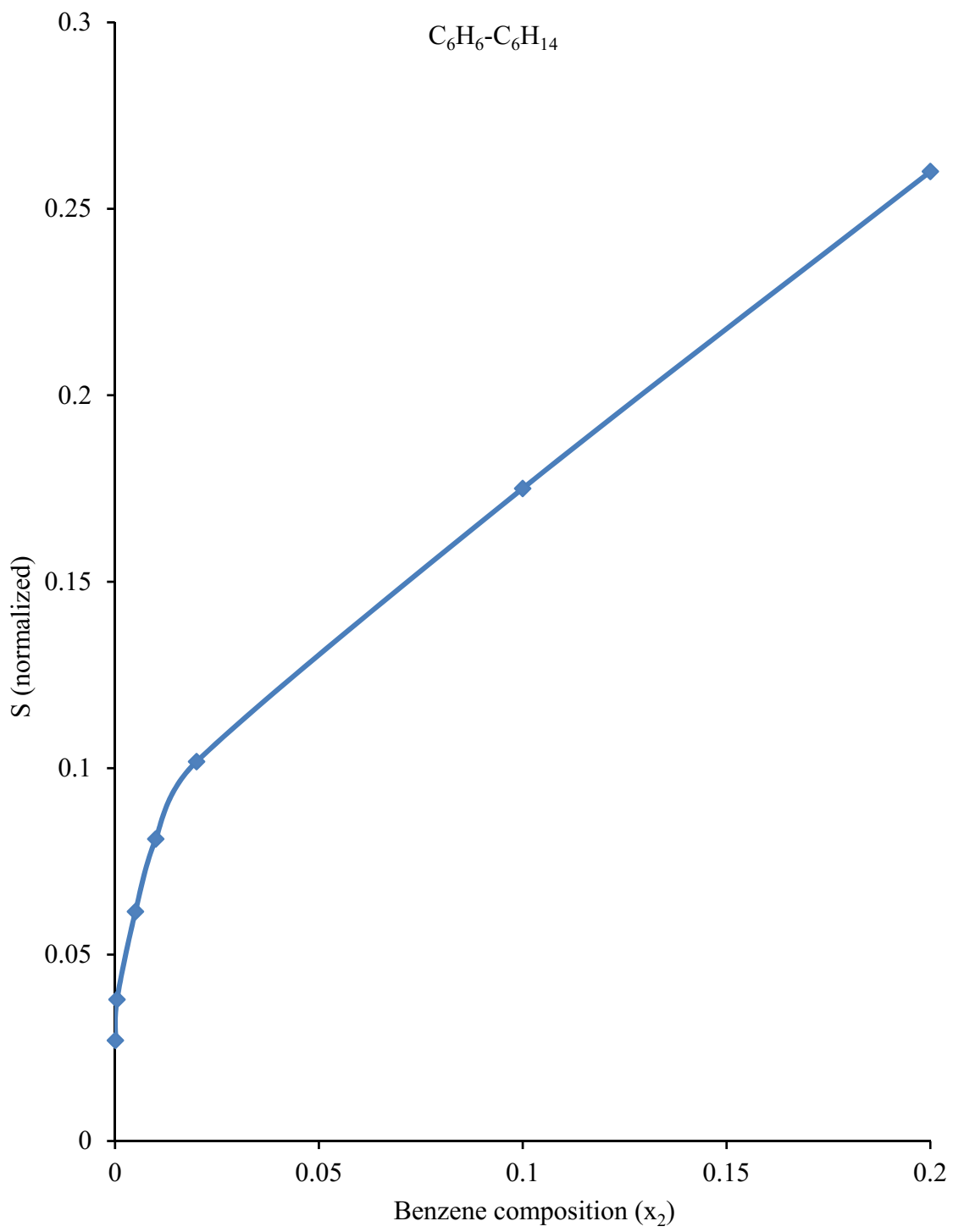


Figure 30. Normalized experimental thermal lens signal as a function of low composition of benzene in n-C₆H₁₄ for the range (0.0-0.2) at 295 K

Similarly, Figure 31 depicts a plot of normalized thermal lens signal versus composition of benzene in CCl_4 for the concentration range (0.0-1.0) and Figure 32 presents detail at low range of concentration (0.0-0.1). In this case, there are less experimental points and fitting function is represented by:

$$S = 0.156 + 0.702x_2 + 0.050(1 - e^{-228x_2}) \quad (37)$$

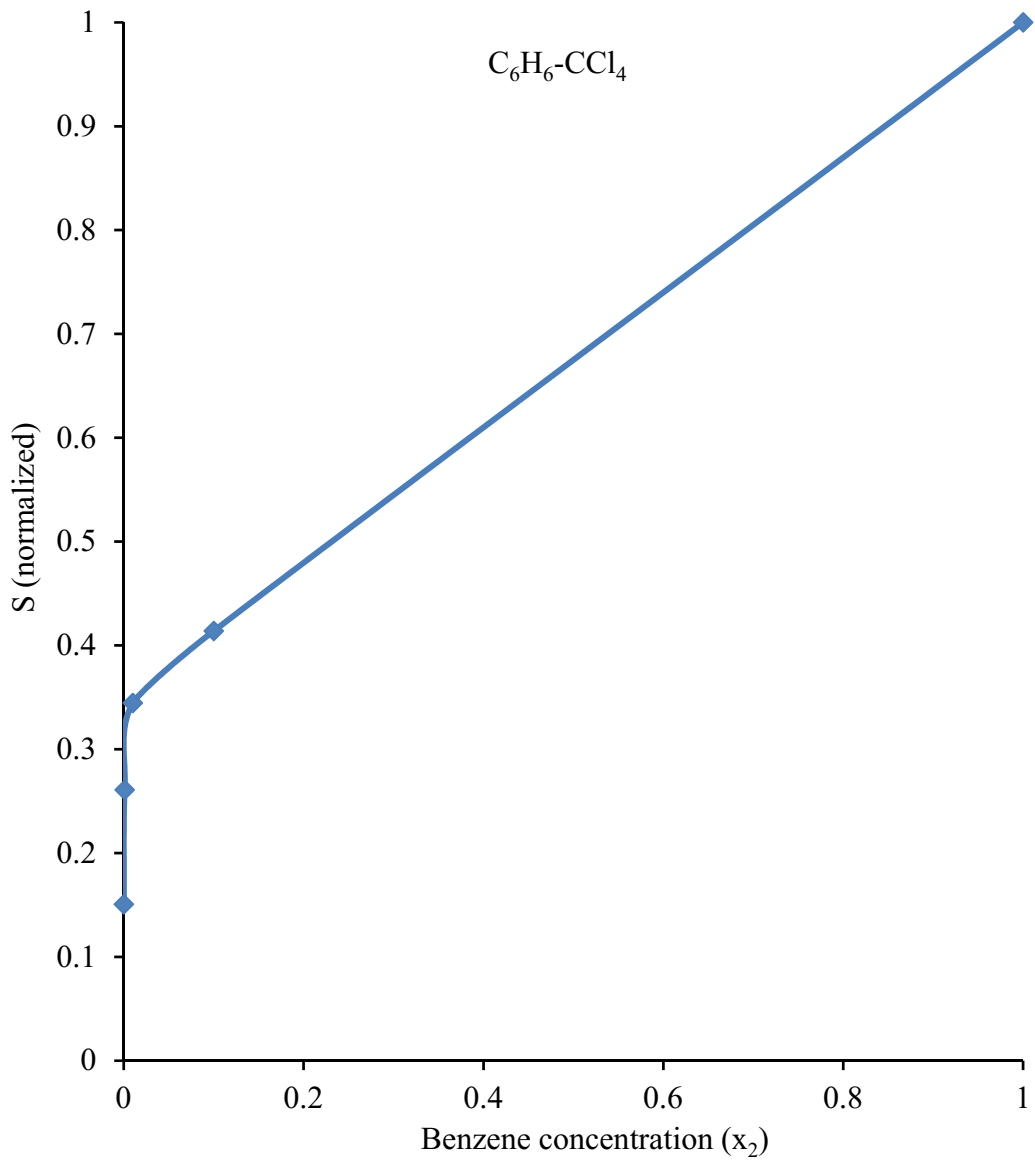


Figure 31. Normalized experimental thermal lens signal as a function of composition of benzene in CCl_4 for the range 0.0 - 1.0 at 295 K

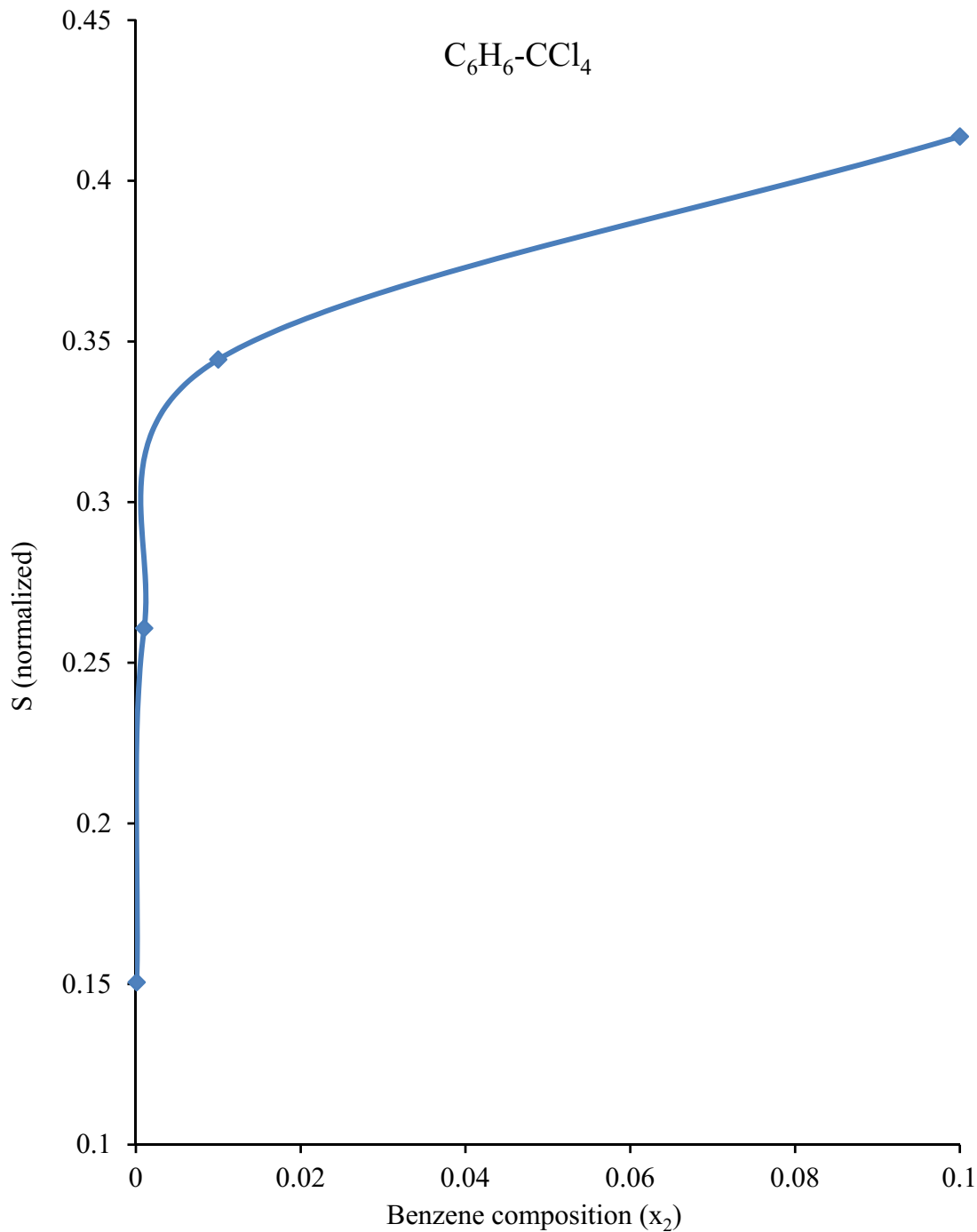


Figure 32. Normalized experimental thermal lens signal as a function of low composition of benzene in CCl_4 for the range 0.0 - 0.1 at 295 K

In both of the solvents the non-linear behavior can be reproduced. We obtained the exponents ($\beta_2 l$) (Eq. 37) which are of the same order of magnitude for the two different solvents.

2.3.4 Electronic Transition of Benzene in n-hexane

In order to support a hypothetical model of two color absorption we obtained the ultra violet absorption spectrum of solution of benzene in n-hexane. Figure 33 presents the electronic absorption spectrum of benzene in liquid hexane. A small band that begins at 270 nm is responsible for the electronic transition in our system.

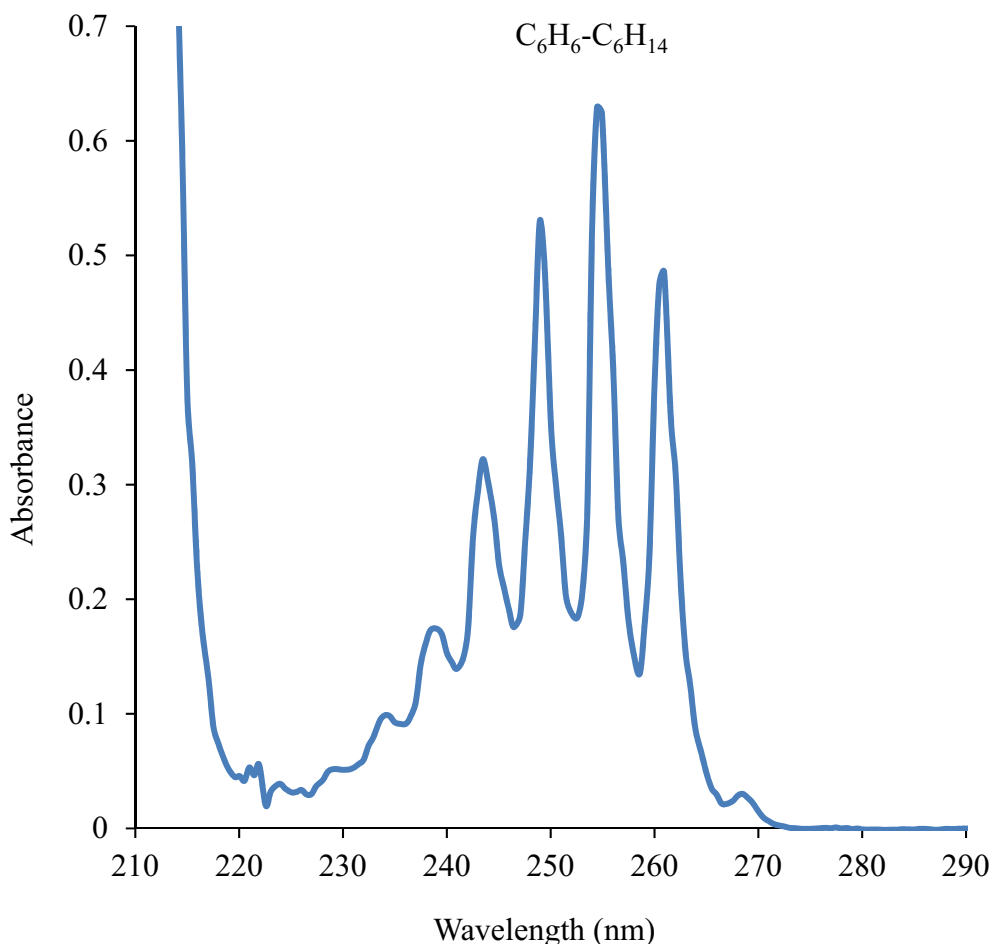


Figure 33. Ultraviolet spectrum of the secondary band of benzene (210-290 nm) in n-C₆H₁₄

Because of the high sensitivity of the technique we are able to see the effect of such small electronic transition on the TLS signal. The addition of the blue laser 488 nm (20492 cm^{-1}) plus the dye laser at 607 nm (16474 cm^{-1}) is 271 nm but the transition is probably around 268 nm considering that at room temperature 1.5 KT is around 308 cm^{-1} .

However, the solvent CCl_4 has an electronic absorption band in this region that overlaps with the absorption of benzene. It is possible to think that CCl_4 is involved in the two-color absorption although it does not have an intermediate vibrational level as in benzene. The fact that benzene in n-hexane also shows non-linear behavior for the overtone absorption at very low compositions could be an indication that benzene is the main molecule involved in the two-color absorption transition.

2.3.5 Experiment with 568 nm Probe Laser

In order to support the two-color excitation model, another experiment with different wavelength of probe laser was performed. To perform an experiment, we just need to change the laser line of same probe laser as well as two filters. In this case, a laser line of wavelength 568 nm is provided by the same probe laser spectra physics model 177-G laser. Excitation and probe beams are overlapped with a red dichroic filter and propagate collinearly through the sample cell. An interference filter (570 nm) was used to block the excitation beam while only transmitting the probe beam.

Figure 34 shows the TLS signal of the fifth ($\Delta\nu = 6$) C-H overtone of benzene in n-hexane with 568 nm probe laser and 607 nm excitation laser. Here we noticed that the same benzene composition signals with 568 nm are smaller than the signals with 488 nm as probe laser (figure 25).

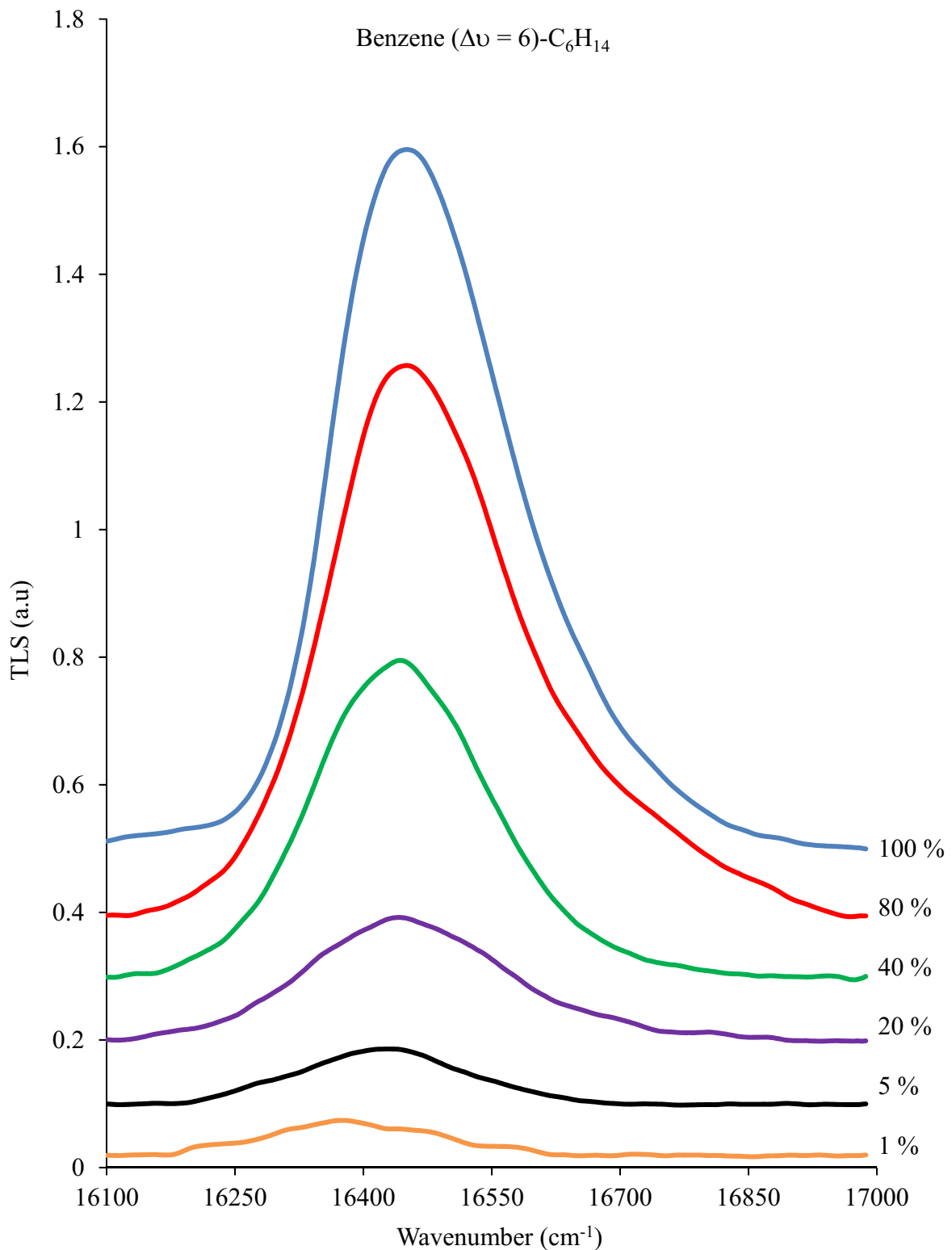


Figure 34. Thermal lens spectra of the C-H vibrational overtone ($\Delta\nu = 6$) of benzene solutions in n-C₆H₁₄ with 568 nm probe laser at 295 K

We integrated the TLS spectral bands for all compositions to get integrated area and normalized all the values with the integrated values of pure benzene similar to the first experiment. Table 15 shows the integrated area and normalized TLS signal of benzene in hexane with the probe laser 568 nm. The solutions of benzene in n-hexane were prepared for compositions by volume in the range 0.01 to 1. Figure 35 shows the comparison of results using two different probe beams. The blue points (non-linear) correspond to the 488 nm probe beam and the red points (linear) correspond to the 568 nm probe beam. The addition of the photon energy at 568 nm (17606 cm^{-1}) plus the dye laser photon at 607 nm (16474 cm^{-1}) gives a 293 nm wavelength (34080 cm^{-1}). This wavelength is outside the main absorption band of C_6H_6 (Figure 33). It is obvious from Figure 35 that decreasing the energy of the second photon (λ_2) eliminates the non-linearity giving support to the hypothesis of two color absorption by using a 488 nm probe laser.

Table 15. Integrated Area of the TLS Spectrum of ($\Delta\nu = 6$) C-H Overtone of Benzene in n-C₆H₁₄ with 568 nm Probe Laser

Benzene composition (x ₂)	Integrated area	Normalized signal
0.01	11.77	0.04036
0.05	21	0.07201
0.1	36.269	0.12436
0.2	56.589	0.194
0.4	128.641	0.44112
0.6	195.157	0.6692
0.8	254.43	0.8724
1	291.623	1

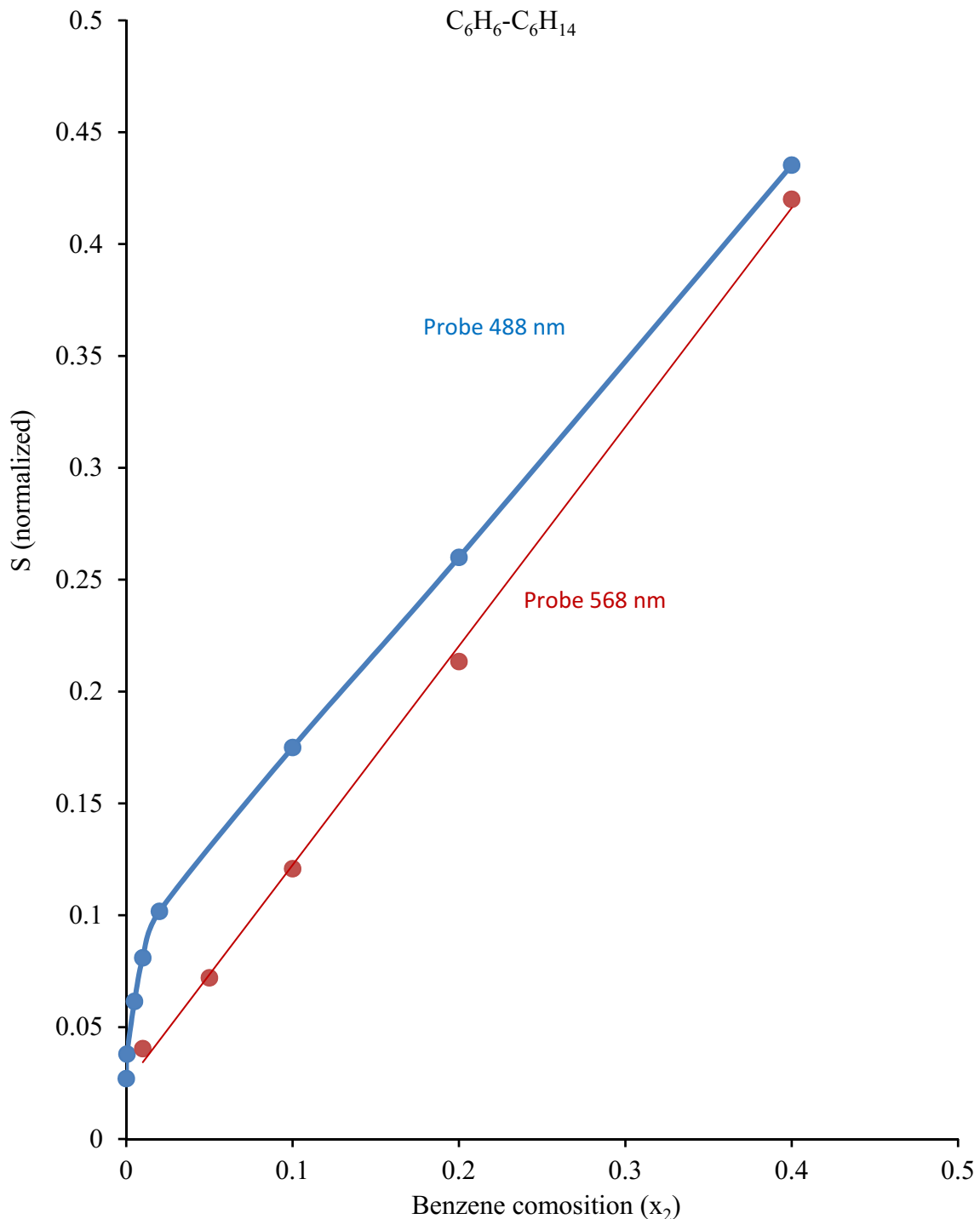


Figure 35. Comparison of non-linear (blue line, 488 nm probe) and linear (red line, 568 nm probe) normalized thermal lens signal as a function of the composition by volume in $\text{C}_6\text{H}_6\text{-n-C}_6\text{H}_{14}$ solutions

2.4 Non-linear Thermal Lens Signal of the ($\Delta\nu = 6$) C-H Vibrational Overtone of Naphthalene ($C_{10}H_8$) in Liquid Solutions of n-hexane

The fifth ($\Delta\nu = 6$) C-H overtone of naphthalene in n-hexane was measured by using the TLS technique. The purpose of this experiment is not only to support the two-color pump probe excitation model but also to show that our technique could be an appropriate choice to study poly-aromatic hydrocarbons at very low compositions. Similar to benzene studied above, we did the experiments with two different wavelengths of a probe laser (488 nm and 568 nm). Figure 36 is TLS spectra of various concentration of naphthalene in hexane with a 488 nm probe laser. The concentrations vary from saturated solution (81963.0 ppm) to low concentration (19 ppm) of naphthalene in hexane at 295 K. The signals presented in the figure are the average of more than 3 measurements for each composition. The averaging of the signal helps to increase the signal to noise ratio of the spectrum.

Similarly, Figure 37 shows the C-H fifth overtone spectra of naphthalene with 568 nm probe laser. The concentrations vary from saturated solution (81963 ppm) to low concentration (19538 .0 ppm) of naphthalene in hexane at 295 K. The signals presented in the figure are the average of more than 3 measurements for each composition. The signal from the 568 nm is smaller than the signal from the 488 nm probe laser. We calculated the integrated area of the spectral bands for all the concentrations and normalized with the integrated values of spectral band of saturated solution of naphthalene in hexane. Table 16 and Table 17 present the integrated area and normalized TLS signals of various concentration of naphthalene in hexane. We plotted the normalized signal versus mole fractions.

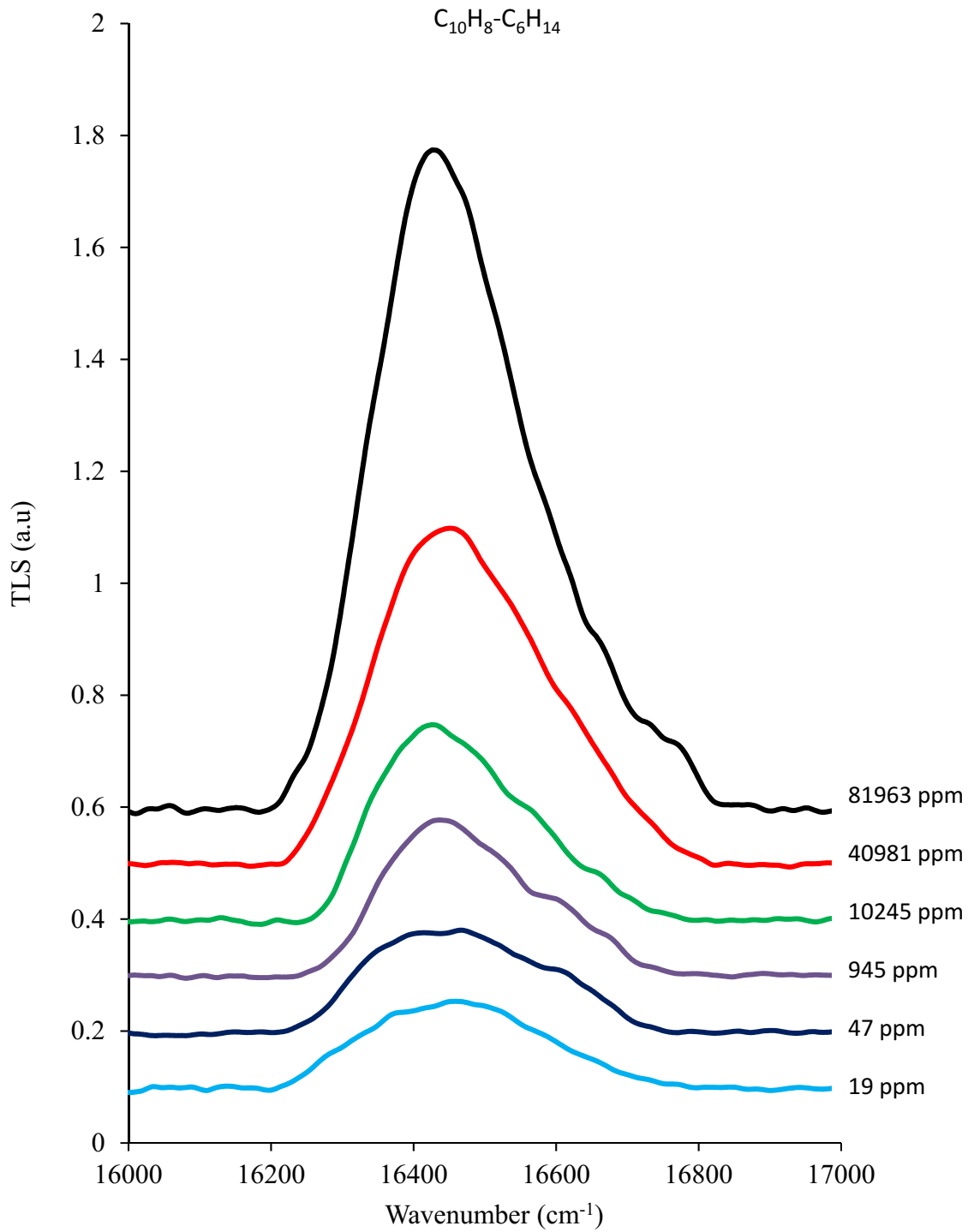


Figure 36. Thermal lens spectra of the C-H vibrational overtone ($\Delta\nu = 6$) of naphthalene solutions in $n\text{-}C_6H_{14}$. The concentrations vary from (19-82360) ppm at 295 K with 488 nm as probe laser.

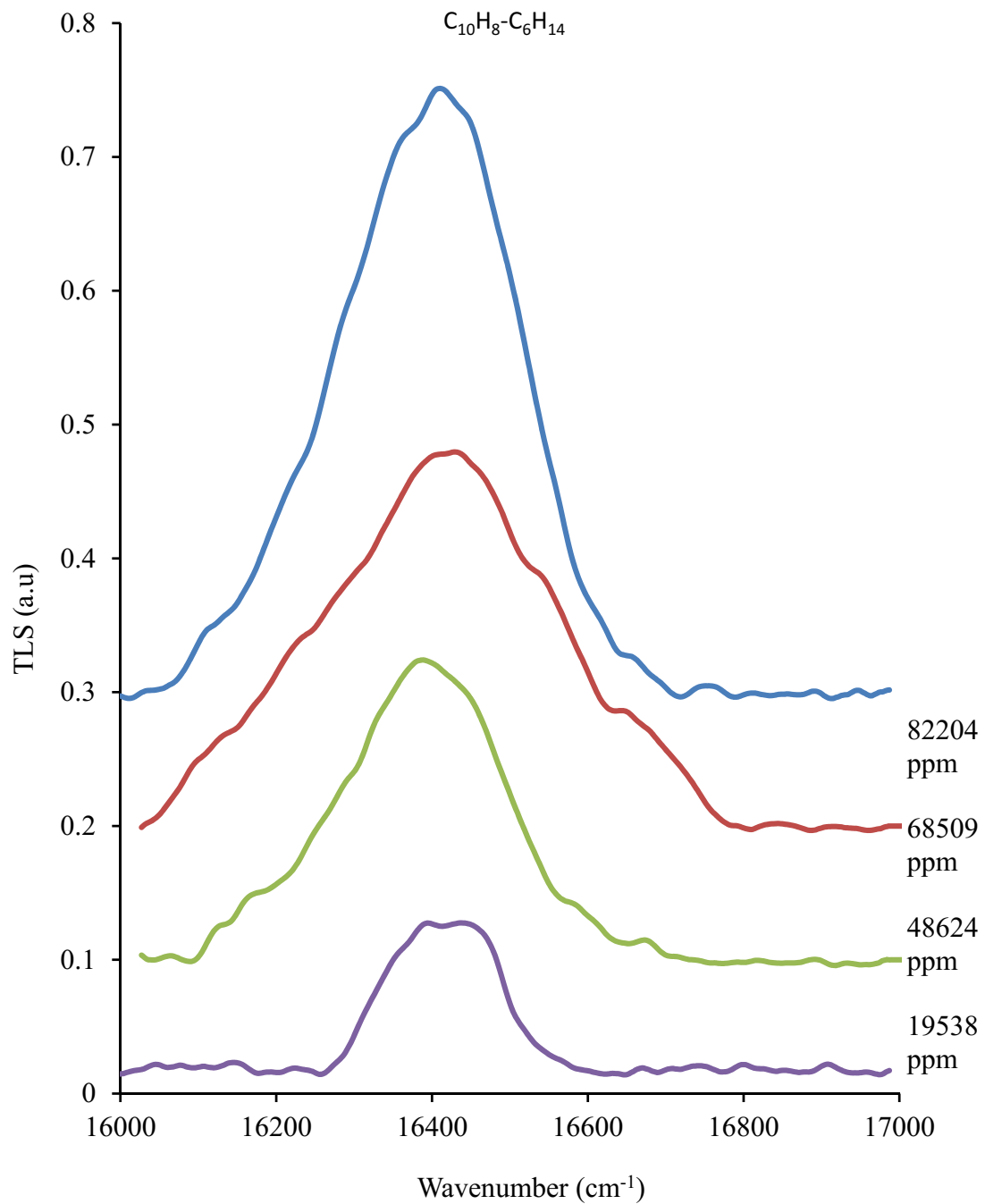


Figure 37. Thermal lens spectra of the C-H vibrational overtone ($\Delta\nu = 6$) of naphthalene solutions in $n\text{-C}_6\text{H}_{14}$. The concentrations vary from (19-82360) ppm at 295 K with 568 nm as probe laser.

Table 16. Integrated Area of the TLS Signal of ($\Delta\nu = 6$) C-H Overtone Transition of Naphthalene Solutions in n-C₆H₁₄ with a 488 nm Probe Laser

X ₂ (ppm)	Molarity (mol/L))	Integrated area	Normalized signal
19	0.00015687	48	0.149
47	0.00039218	57.52	0.178
95	0.000784	36.56	0.113
945	0.00784	72.74	0.226
5123	0.0425	84.16	0.261
10245	0.085	88.88	0.276
20491	0.17	117.71	0.365
40981	0.34	173.65	0.539
81963	0.68	322.45	1

Table 17. Integrated Area of TLS Signal of ($\Delta\nu = 6$) C-H Overtone Transition of Naphthalene Solutions in n-C₆H₁₄ with a 568 nm Probe Laser

X ₂ (ppm)	Molarity (mol/L)	Integrated area	Normalized signal
19538	0.16	19.37	0.06
48624	0.40	61.34	0.19
68509	0.57	103.47	0.32
82204	0.68	132.16	0.41

Figure 38 depicts the comparison of the results with two different probe lasers. The solution of naphthalene in hexane is prepared from saturated solution (81963 ppm) to 19.0 ppm. The blue line corresponds to 488 nm probe beam and the red line corresponds to the 568 nm probe beam. The addition of the photon energy at 488 nm (20492 cm^{-1}) plus the dye laser photon at 607 nm (16474 cm^{-1}) gives an energy equivalent of 271 nm (34080 cm^{-1}). The wavelength (271 nm) lies very close to the place of maximum absorption of naphthalene as shown in the Figure 39. As a result, the signal enhancement in naphthalene is even higher than in benzene.

However, the addition of the energy of a photon at 568 nm (17606 cm^{-1}) with the photon of dye laser 607 nm (16474 cm^{-1}) results in 293 nm (34080 cm^{-1}) which lies outside the main absorption band of naphthalene. It helps to support the two color two photon absorption with a 488 nm probe laser.

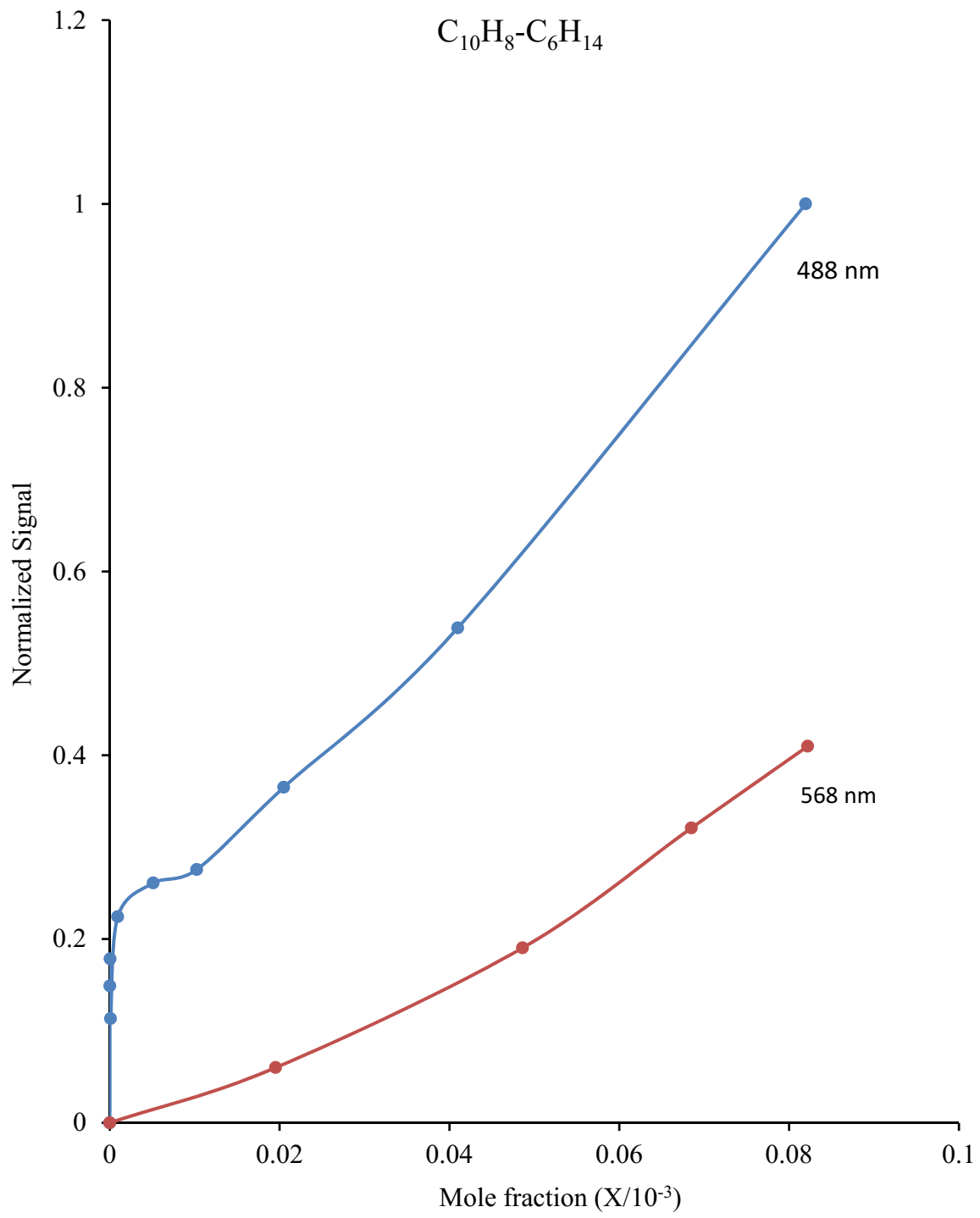


Figure 38. Comparison non-linear (blue dots, 488 nm probe) and linear (red dots, 568 nm probe) normalized thermal lens signal as a function of the concentration of in $\text{C}_{10}\text{H}_8\text{-C}_6\text{H}_{14}$ solutions for the range (19.0-82360) ppm at 295 K.

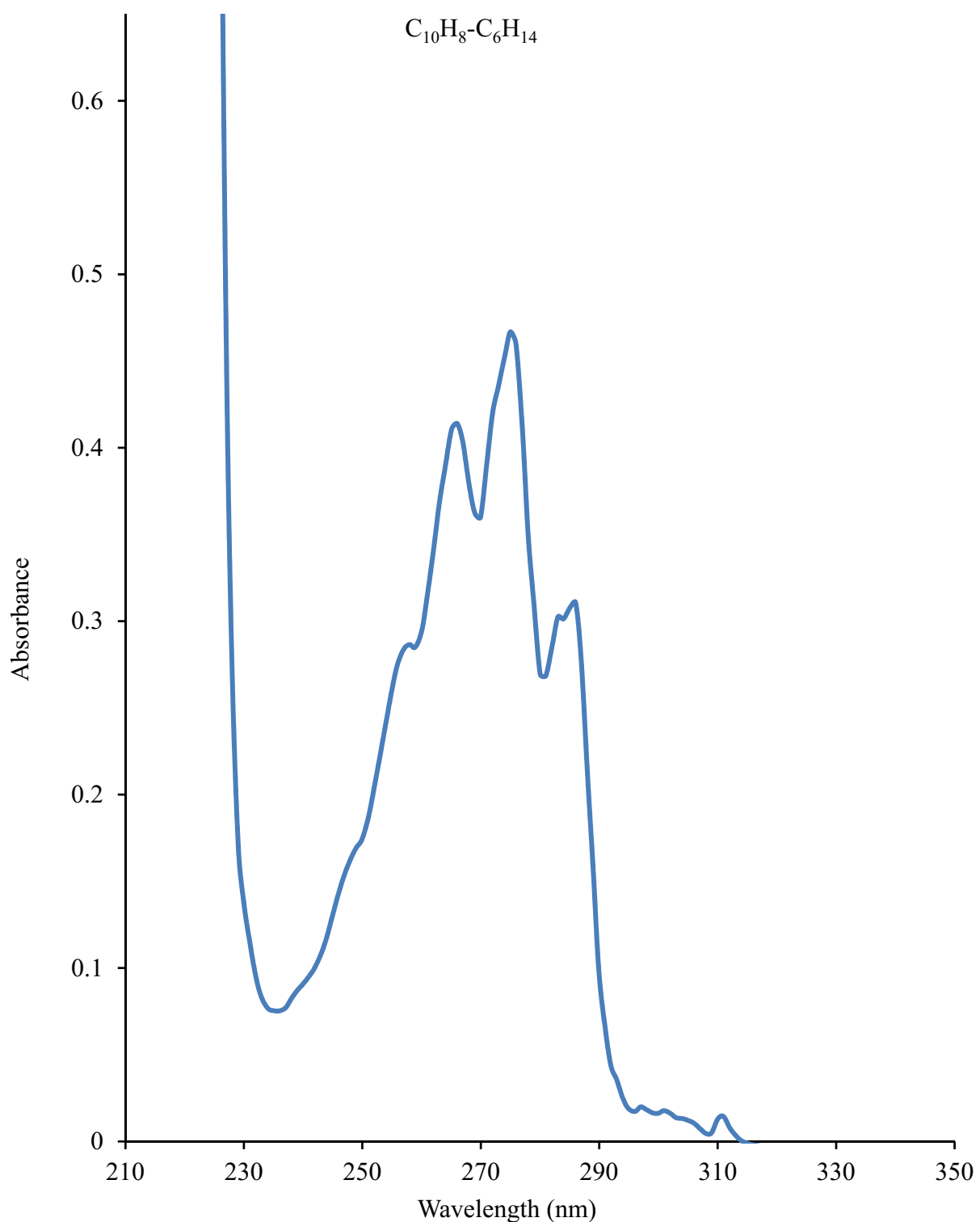


Figure 39. Ultraviolet spectrum of the naphthalene (210-350 nm) in $\text{n-C}_6\text{H}_{14}$

2.5 Conclusions

The sensitivity of the thermal lens technique has been demonstrated by measuring a very weak overtone transition ($\Delta\nu = 6$) of benzene in solutions of CCl₄ and n-C₆H₁₄ as the solvents and naphthalene in n-hexane. The complete absorption band of a 100 ppm solution of benzene has been obtained indicating that a peak absorption $\alpha_2 x_2 = 2.2 \times 10^{-7}$ cm⁻¹ is being detected. This absorption is 100 times smaller than the one measured previously using piezoelectric acoustic detection [132].

The solvent enhancement effect has been calculated over the entire range of concentrations indicating a steady increase when the composition solute decreases for CCl₄ as a solvent. A similar calculation shows that with n-C₆H₁₄ as solvent there is no enhancement. It has been shown that solvent enhancement is not responsible for the non-linear behavior at composition below 1%. A two color absorption mode that includes the simultaneous absorption of the pump and probe lasers could explain the non-linear behavior at low composition. A comparison of the normalized calculated and experimental signals shows very good agreement for both solvents over the entire range of benzene compositions.

It has been demonstrated that the dual-beam thermal lens technique can detect high vibrational overtones in very low concentration (ppm) solutions at room temperature. In addition, by exciting very weak overtone absorption, a non-linear term is exposed at compositions below 1%. It is the combination of the very low absorption cross section and low concentrations that exposes the non-linear behavior.

These new room temperature experiments will allow us to continue investigating the enhancement and non-linear behavior in more detail for weaker transitions such as the

C-H ($\Delta\nu = 7$) overtone transition of benzene and other aromatic compounds to show the non-linear behavior at higher composition. In addition, the cryogenic experiments will be expanded to consider other unsaturated ring compound that could be present in the lakes of Titan.

2.6 Optical Saturation in Thermal Lens Spectroscopy (TLS)

Optical saturation is an omnipresent problematic issue for all the branches of spectroscopy [133] and is more common in photo-thermal (PT) spectroscopy. The thermal lens spectroscopy (TLS) is one type in which the strength of signal depends on the absorption of energy from the excitation laser. From the study of TLS signal as a function of excitation power, it is found that the signal is directly proportional to the excitation power at low intensities. This encourages researchers to use high excitation power and improve the detection limit [134] specifically with work involving weakly absorbing samples and imaging applications.

However, an attempt to increase the PT signal by increasing the intensity of highly focused excitation source might bring non-linear optical phenomena, such as optical saturation or optical bleaching, which limit the sensitivity of the techniques. The unnecessarily high power can lead to a great reduction in the amplitude of the signal. This effect not only complicates the interpretation of the experimentally obtained data, but also distorts the spectral profiles of the measured samples [134].

As far as we know, to date, the effect of optical saturation on TLS has been investigated through the various theoretical models like the Parabolic Model and aberrant model [134,135]. However, there is limited experimental data on the effect of optical

saturation on TL spectroscopy. The purpose of this project is to study the effects of optical saturation on TLS signal.

2.7 Study of Optical Saturation on Thermal Lens Signal (TLS) of the Fifth ($\Delta\nu = 6$) C-H Overtone Transition of Benzene, Chlorobenzene and O-dichlorobenzene.

Optical saturation on thermal lens spectroscopy (TLS) of the fifth ($\Delta\nu = 6$) C-H vibrational overtone transition of benzene and some of its derivatives has been studied with the analysis of dependence of the TLS signal on the intensity of the illumination source. The various degrees of the optical saturations were obtained by raising the power of the excitation laser up to 120 mW and keeping the rest of the parameters affecting the signal constant. When the excitation power exceeds the optimum limit, the amplitude of the TLS signal around the place of maximum absorption of the sample gets smaller than expected and forming a dip, which is because of the stimulated emission. As far as we know, this first time experimental report on the optical saturation of TLS signal of the fifth ($\Delta\nu = 6$) C-H overtone transition of benzene and its derivatives could be a contribution to developing theoretical models for the thermal lens effect and provide more insight on the TLS technique.

At first, we studied the strength of the TLS signal as a function of the excitation power. Spectra were obtained by increasing the power of the pump laser until the amplitude of the signal at the place of maximum absorption reached to the maximum value and indicating the saturation. Figure 40 and Figure 41 show the TLS signal of chlorobenzene and O-dichlorobenzene with various pump powers respectively. Here we noticed that the amplitude of the signal increases with power at a certain limit and then decreased at the region of the maximum absorption of the sample.

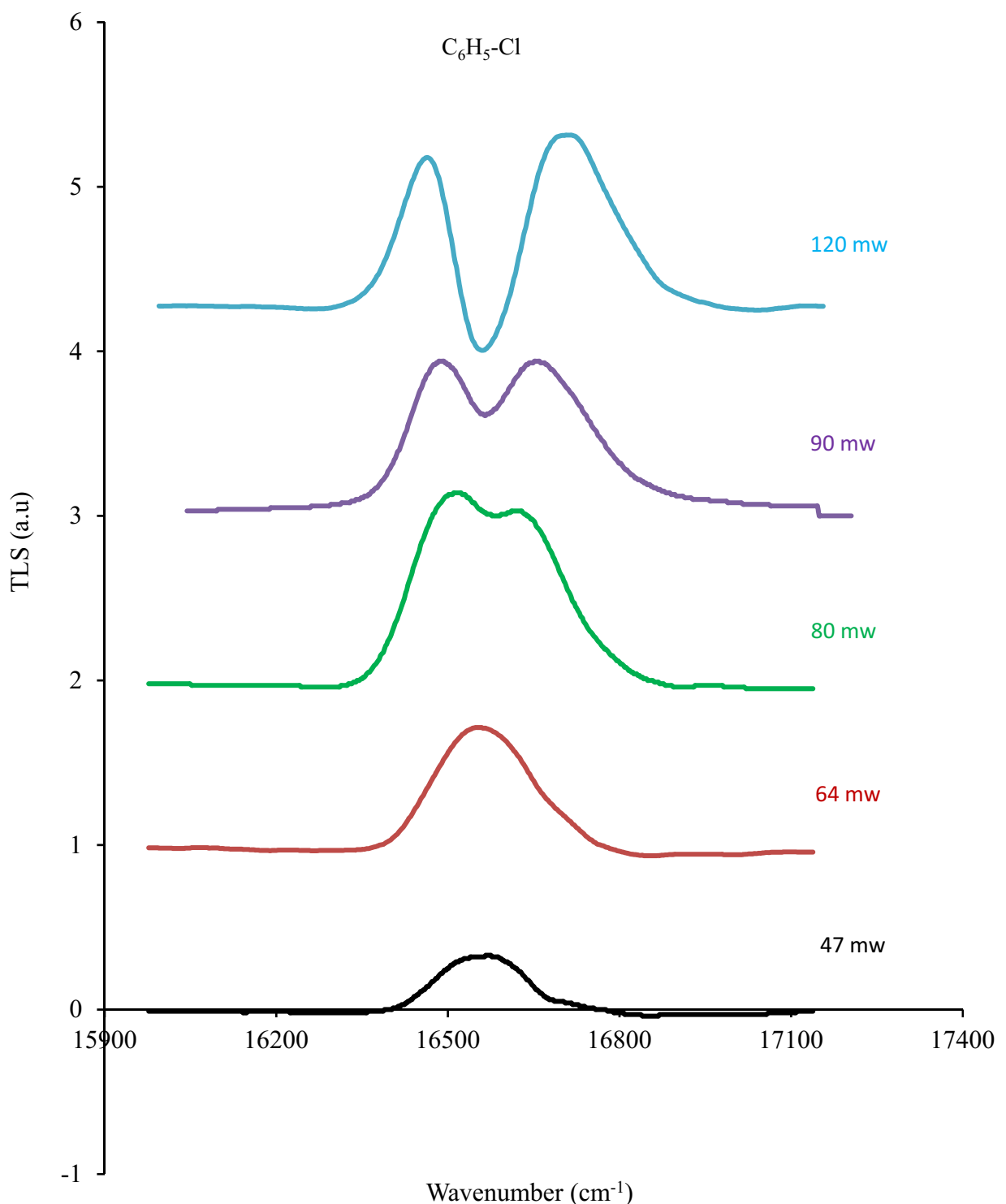


Figure 40. Thermal lens signal of the fifth ($\Delta\nu = 6$) C-H overtone spectrum of chlorobenzene with various pump powers at 295 K

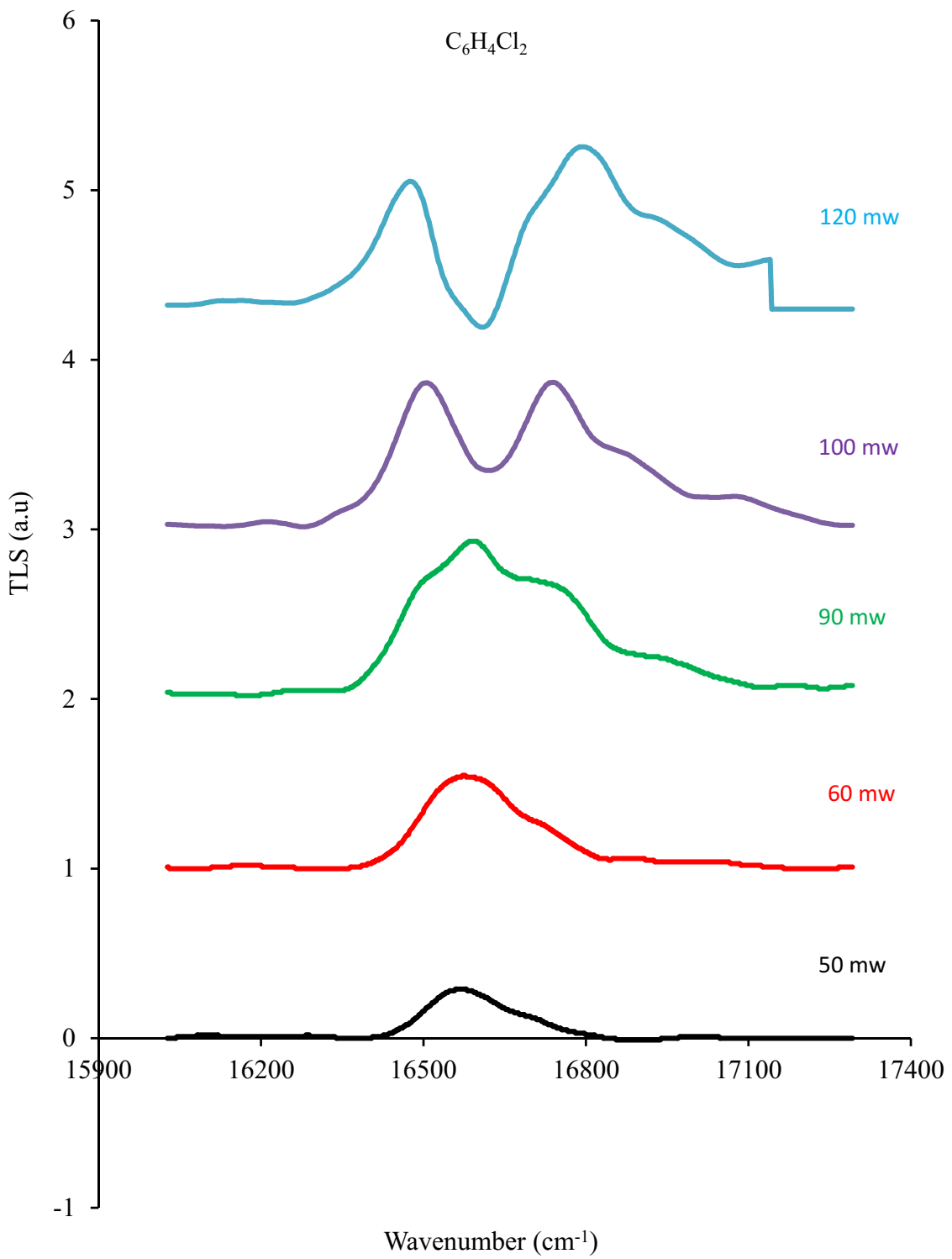


Figure 41. Thermal lens signal of the fifth ($\Delta\nu = 6$) C-H overtone transition of O-dichlorobenzene with various pump powers at 295 K

Table 18 and Table 19 present the amplitude of the TLS signal of chlorobenzene and o-dichlorobenzene liquid with various pump power respectively. The data shows that the amplitude of the TLS signal linearly increases with power up to 80 mW (for chlorobenzene) and 90 mW (for O-dichlorobenzene) and then started to decrease with power higher than that limit. Figure 42 and Figure 43 depict the plot of the TLS signal amplitude as a function of excitation power which only covers the linear portion of the plot.

Table 18. TL Signal Amplitude at Region of Maximum Absorption of Chlorobenzene

Amplitude of the signal	Pump power (mW)
0.33	47
0.559	57
0.714	64
1	80
0.62	90

Table 19. TL Signal Amplitude at the Region of Maximum Absorption of O-dichlorobenzene

Amplitude of the signal	Pump power (mW)
0.15	40
0.29	50
0.55	63
0.63	70
0.93	90
0.348	100

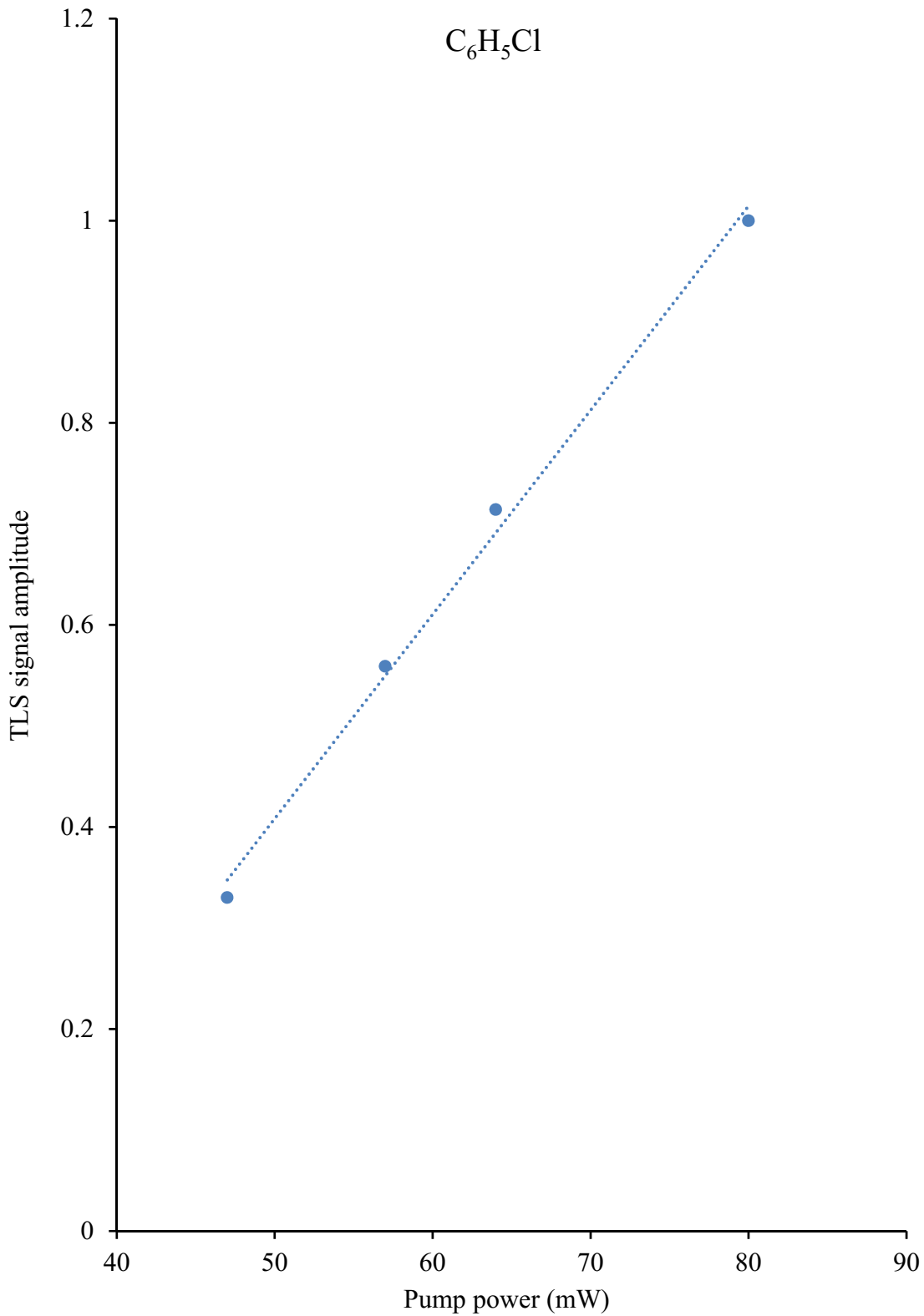


Figure 42. Pump power versus the TLS signal amplitude of chlorobenzene at 298 K

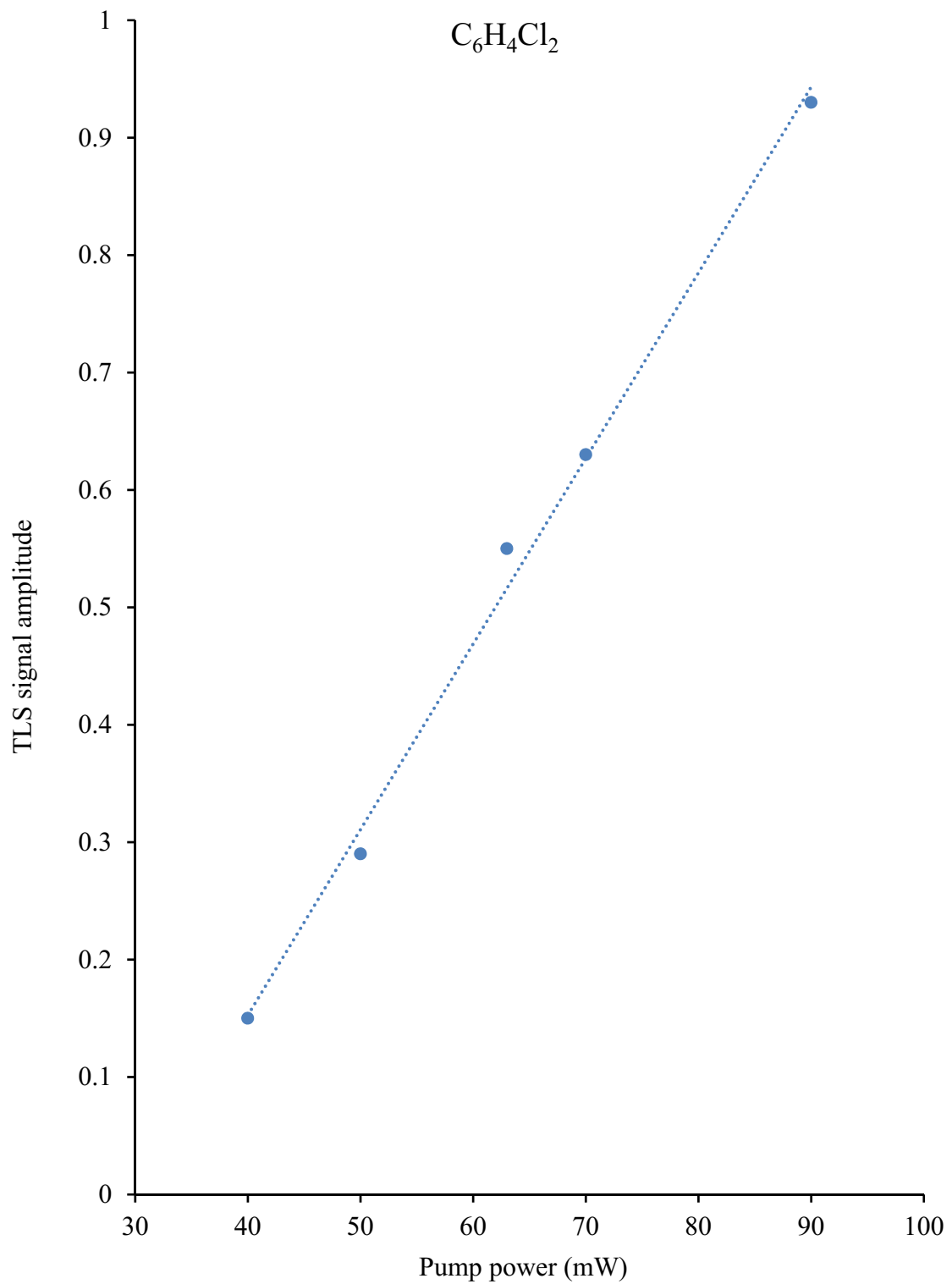


Figure 43. Pump power versus the TLS signal amplitude of O-dichlorobenzene at 298 K

Once we observed an optical saturation effect on TLS signal, our interests focused on the detailed exploration of the optical saturation on the thermal lens spectroscopy. Figure 44 and Figure 45 shows the various degrees of the optical saturation on the TLS signal of the fifth ($\Delta\nu = 6$) C-H overtone transition of benzene and chlorobenzene liquid. In this experiment pump power varies from 18 mW to 70 mW but Figure 44 and Figure 45 only present the signals from the optimum (57 mW) and higher power of the excitation laser. The figures show that, at optimum power the signal is narrower and more symmetric with maximum intensity. However, if the excitation power exceeds the limit, the spectra show the optical saturation. The degree of the optical saturation increases with an increase in excitation power. At excessive power, the signal intensity localized around the place of maximum absorption (16474 cm^{-1} for benzene and 16580 cm^{-1} for chlorobenzene) are lower than expected, and formed a dip which is called the Lamb-dip. Table 20 and Table 21 show the height and width of the Lamb dip for benzene and chlorobenzene at various powers.

Table 20. Height and Width of Lamb Dip on Various Saturated TLS Signal of Pure Benzene

Pump power (mW)	Height of Lamb dip	Width of lamb dip (cm^{-1})
58	0.061	54.186
60	0.1065	66.935
62	0.244	85.261
64	0.3275	79.685
66	0.4995	94.824
70	0.631	109.168

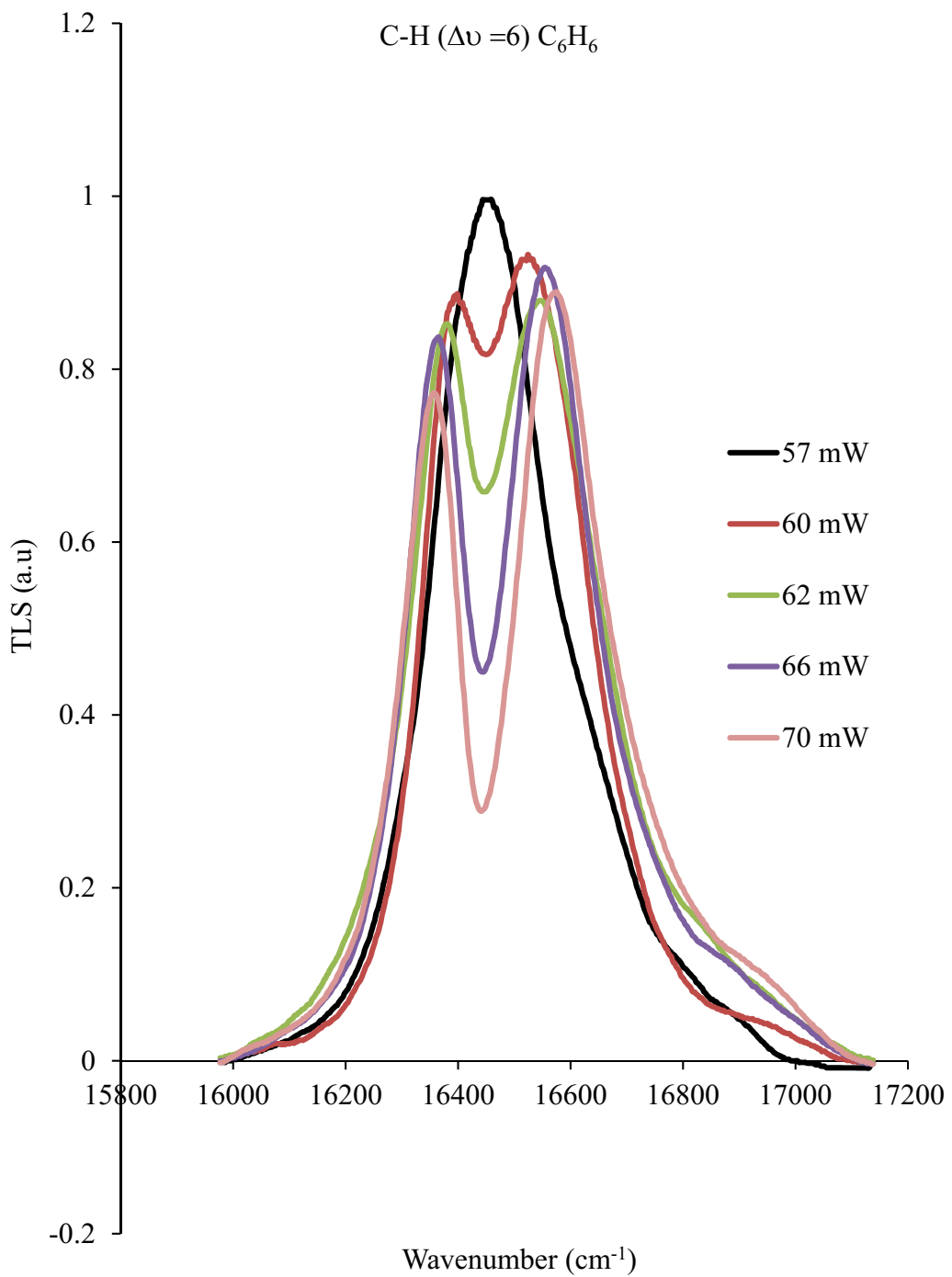


Figure 44. Various degrees of optical saturation on TLS spectrum of the fifth ($\Delta\nu = 6$) C-H overtone transition of benzene with various excitation laser powers

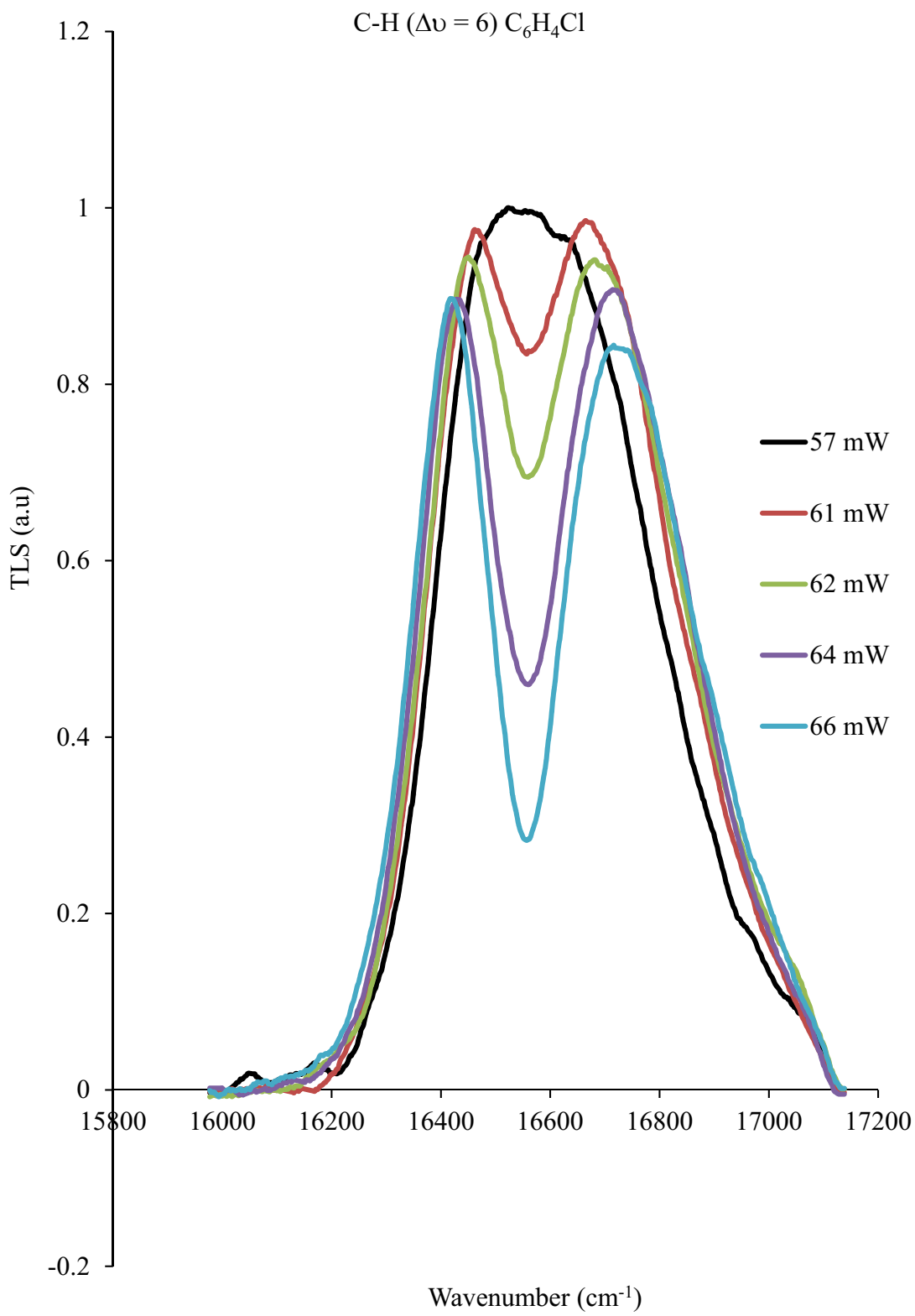


Figure 45. Various degree of optical saturation on TLS spectrum of the fifth ($\Delta\nu = 6$) C-H overtone transition of chlorobenzene with various excitation laser powers

Table 21. Height and Width of Lamb Dip on Various Degree of Saturated TLS Signal of Chlorobenzene

Pump power (mW)	Height of lamb dip	Width of lamb dip (cm ⁻¹)
61	0.108	109.4
62	0.185	118.33
64	0.3295	136.19
66	0.4365	147.36

Figure 46 and Figure 47 depict the plot of the height of the Lamb dip versus power of the pump laser for benzene and chlorobenzene. The plots show that the Lamb dip height increases with increase in power. This is because of the significant depopulation of the ground and excited states by stimulated emission and not by the radiation-less decay. This assumption is supported by obtaining the negative signal amplitude at very high saturation power as shown in the top spectra in Figure 40 or Figure 41. Furthermore, the absorption coefficient decreases with increasing intensity of the excitation beam which results in increase of height of the Lamb dip.

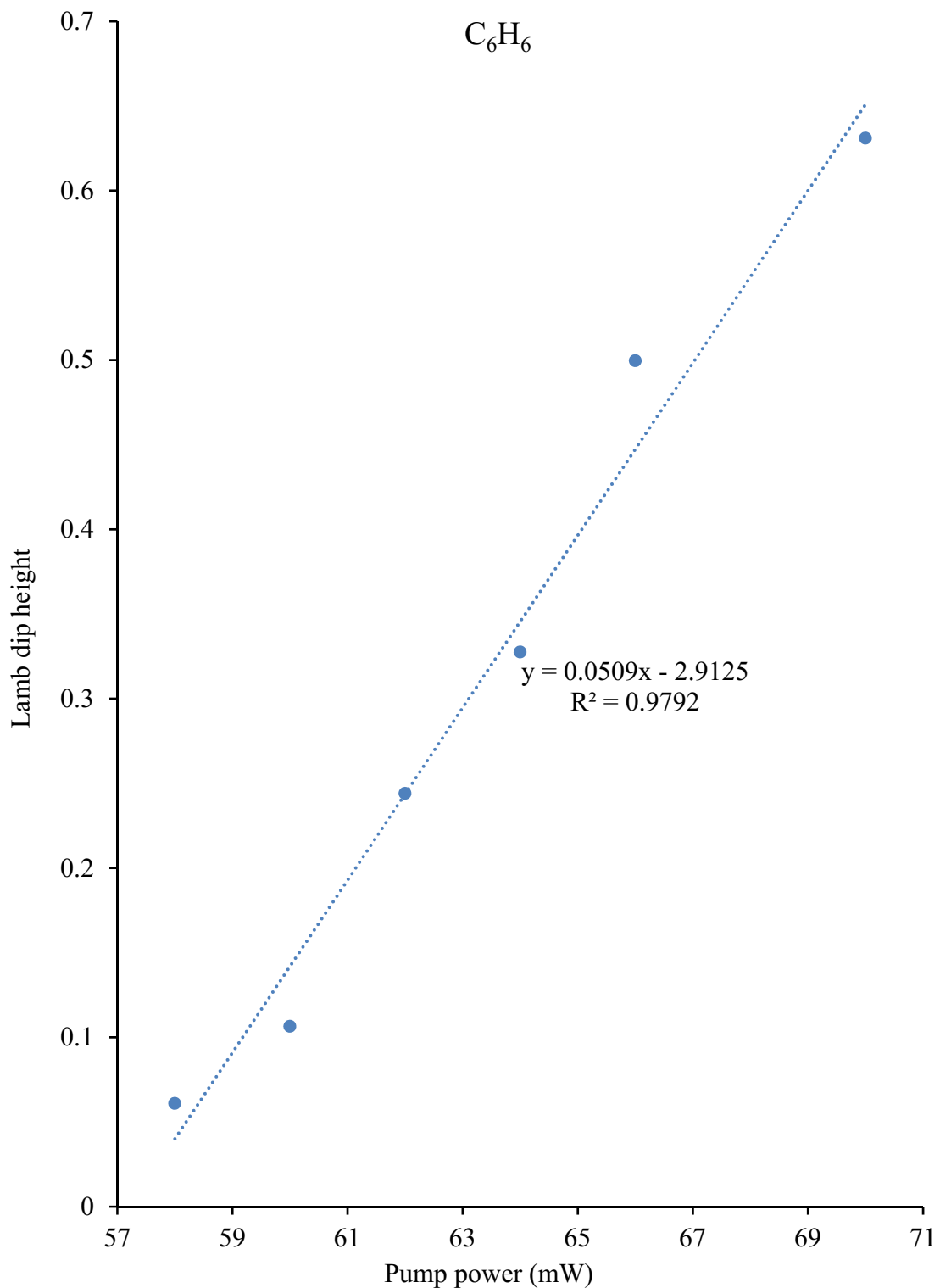


Figure 46. Plot of the height of the Lamb dip on saturated TLS spectrum of the fifth ($\Delta\nu = 6$) C-H overtone transition of benzene versus excitation laser power

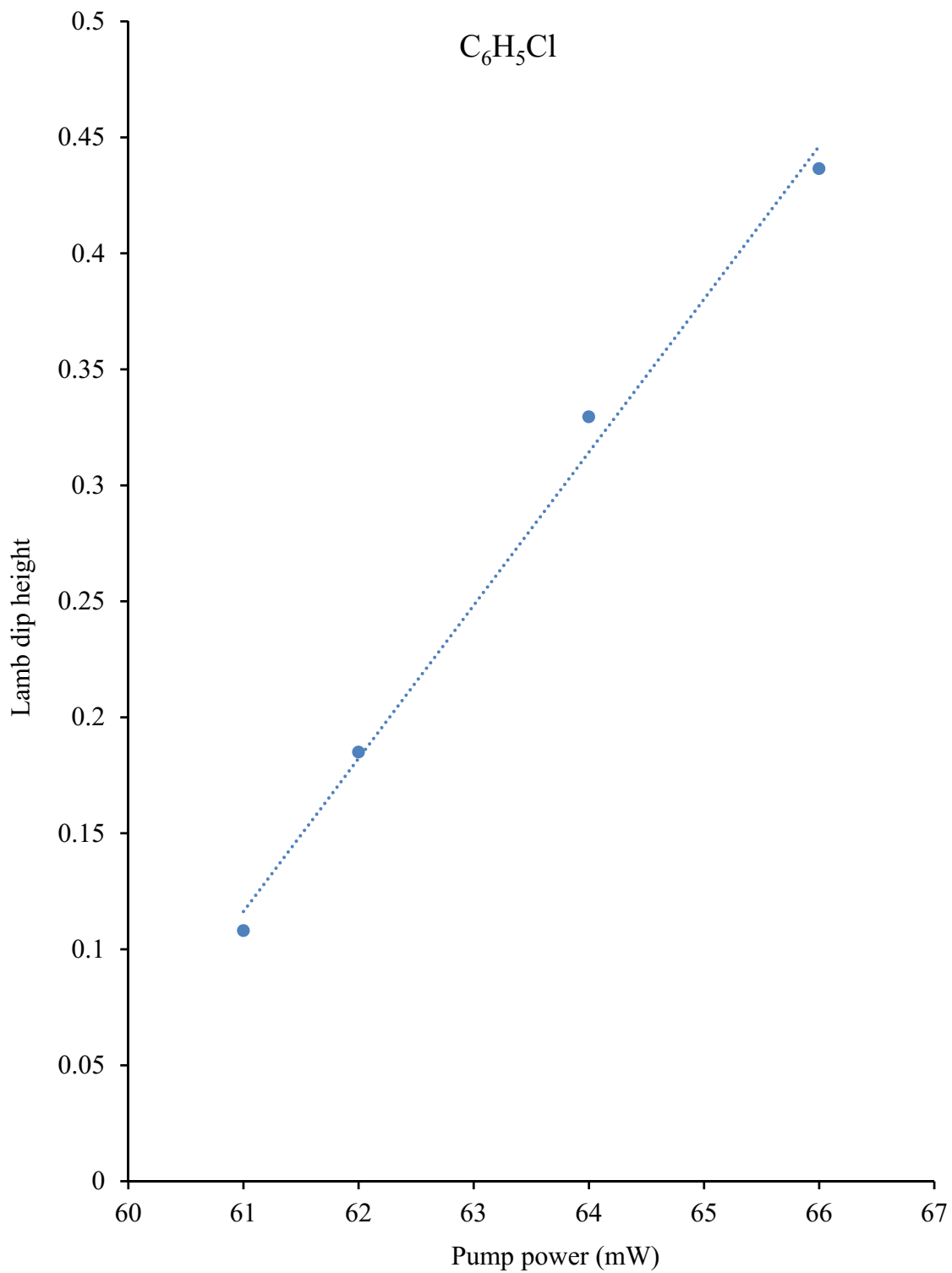


Figure 47. Plot of the height of the Lamb dip on saturated TLS spectrum of the fifth ($\Delta\nu = 6$) C-H overtone transition of chlorobenzene versus excitation laser power

2.8 Conclusions and Research Outlook

We studied the optical saturation on thermal lens spectroscopy of the fifth ($\Delta\nu = 6$) C-H overtone transition of liquid benzene, chlorobenzene and dichlorobenzene at room temperature. The various degree of saturation was observed by increasing the excitation power up to 120 mW. In our system, the optimum power for TLS spectrum ($\Delta\nu = 6$) C-H overtone of benzene and chlorobenzene was around 57 mW. If the excitation power exceeds the optimum power, then the amplitude of the signal at the place of maximum absorption (16474 cm^{-1} for benzene and 16580 cm^{-1} for chlorobenzene) was lower than expected and formed a dip. The dip becomes deeper with increasing excitation power; this is because of the significant depopulation of the ground and excited state by stimulated emission and not by radiation-less decay. In addition, the absorption coefficient decreases with increasing intensity of the excitation laser and formed a deeper lamb-dip. The optical saturation not only influenced the amplitude, but also distorted the temporal behavior of the TLS signal. This experimental study will be helpful to test and modify the theoretical TLS model which will address the issues of optical saturation.

We have established our system as an ultra-sensitive technique by showing the successful utilization for the study of very low concentrated solutions of complex molecules like naphthalene, benzene and its derivatives. The enhancement on the TLS signal by two orders of magnitude really encourages us to use this technique for the study of complex biomolecules in the future. Additionally, we would like to apply this technique in the measurement of fluorescence signal which is generated by two color absorption.

CHAPTER THREE

3.1 C-H Infrared Absorption and Solubility of Unsaturated Hydrocarbons at Cryogenic Temperatures

The solubility of solid and liquid impurities in cryogenic solvents has received tremendous attention in the scientific community because of its direct implication on the designs of heat exchangers and transport systems for cryogenic liquids. The solubility of impurities plays a key role in various processes of the cryogenic solvents like, liquefaction and purification. If the impurities' concentration exceeds their solubility limits, they might be suspended as microcrystals which are not discernible. Such solid precipitation causes the blockage in the heat exchangers and pipelines and eventually, it might result in shutting down the process [136-138].

Global searching of the outer planets and moons, like Jupiter, Mars, Titan etc., has made scientists curious about the existence of alien life. For that purpose, it is necessary to study the chemistry on their atmosphere and surfaces. Hydrocarbons are the basic compounds that can predict the evolution of life. So, identification and quantification of hydrocarbons is a highly concerning matter in scientific investigating. We were interested in Titan (largest moon of Saturn). There are many reports on the composition of the atmosphere of Titan [139-142], but its surface is still mysterious. The study of composition of lakes on the surface of the Titan was the focus in this project. Many researchers believe that Titan has lakes of hydrocarbons which are mainly composed of ethane and methane and simple diatomic molecules [143-145]. Surprisingly, there is very little information that focuses on spectroscopic and photochemical transformation of organic unsaturated linear

or ring compounds dissolved in liquid ethane and methane. Some scientists have simulated the composition of the lakes [146,147]. It is necessary to know the solubility of compounds at low temperature to reflect the conditions of Titan. However, it's complicated to obtain the solubility data of various saturated and unsaturated hydrocarbons at low temperatures. The solubility of hydrocarbons in the lakes is supposed to be very low; some powerful techniques are required to get such a low solubility data.

In the past, some of the conventional techniques, like filtration and gravimetric analysis, were used to calculate the solubility of various compounds [148-153]. However, the results were highly inconsistent among the different techniques because the conventional methods have various sources of the error and low sensitivity.

Determination of solubility of the solute from the filtration method introduces several sources of error. Prime sources are from the process of attaining the equilibrium between the solid and liquid phases. The process of filtration of the saturated solution, evaporation of large quantities of the very dilute sample solutions and the vapor pressure of the solute are major contributor for the erroneous result [154]. Some sources of error are also associated with super saturation, formation of metastable phase of solid solute (amorphous solids, or the amorphous portions of crystalline solids), clusters, purity of components of the solute, and accuracy of the measurement in the process of preparation of the sample [155,156]. In some cases, the cooling of the solute may not be sufficient to produce the crystals and a glass may occur. In addition, stable suspensions of the finely dispersed solid phase of solute are readily formed in cryogenic solutions [156]. These sources of error in filtration methods are very difficult to avoid and adding the adsorption onto the sample setup could lead to an erroneous result.

3.1.1 Cryospectroscopy and its Importance

In order to minimize error and obtain precise data with very convenient and easy techniques, researchers are focusing on molecular spectroscopy at cryogenic temperature which is called cryo-spectroscopic techniques [157, 158]. It has several advantages over the traditional techniques. One of the preferable aspects is that the spectra are very sharp and avoid the hot vibrational bands and rotational congestion. Second, there is no spectral splitting as in matrix isolation method [159-164]. There are various spectroscopic techniques which have been used to study molecular spectroscopy at cryogenic temperatures like: thermal lens spectroscopy (TLS) [131], photo-acoustic spectroscopy (PAS) [165,166], ultraviolet spectroscopy (UVS) [157,167], and Fourier transform infrared spectroscopy (FTIR) [157,158,159, 168].

Furthermore, due to the lack of technicalities and difficulties in carrying out the experiment with very dilute solutions at low temperature, some of the existing data needs to be reevaluated. In this project, the solubility of the unsaturated hydrocarbons, 2-methyl-2-butene and methyl-acetylene in liquid argon solutions have been determined at 100 K. For this purpose, Fourier transform infrared (FTIR) spectrometer coupled with a cryostat was used. Even though the solubility of hydrocarbons in liquefied rare gas is very low, rare gases are preferable as a solvent due to their transparency, absence of any spectral shift, and their ease of availability [162]. This technique is easy and simple for the preparation of the sample. It avoids the pitfalls of the conventional filtration method, and is able to reproduce the results.

3.2 Fourier Transform Infrared (FTIR) Spectroscopy

3.2.1 Spectrometer Description

Thermo-Scientific Nexus 760 Fourier Transform Infrared (FT-IR) spectrophotometer was used to obtain vibrational transitions in the range 400-15750cm⁻¹. It is operated with OMNIC software which provides an interface and optimizes performance. It allows working in various spectral regions by selecting the appropriate combinations of different parameters like light source, beam splitter, and detector. Table 22 presents various combinations recommended by manufacturer and experimental testing for the best performance in different spectral regions.

3.2.2 Cryostat, Sample Cell and Vacuum Chamber

A cryostat, APD cryogenics Heli-Tran Model LT-3-110 system was used for cooling of the samples. Liquid N₂ acts as cryogen which is obtained from a pressurized supply Dewar. The cryogen is forced by pressurized nitrogen (5 psi) to make a flow through a transfer line to the cryostat head and then spread out from a needle valve present at the tip of the cryostat head. The flow of cryogen is controlled and regulated by the needle valve.

Table 22. Combination of Instrumental Parameters for FTIR Spectrometer

Spectral range (cm ⁻¹)	Beam splitter	Detector	Source
2000-6500	XT-KBr	DTGS-KBr	Ever-Glo
6500-9500	XT-KBr	DTGS-KBr	White
9500-25000	Quartz	Si	White

The cryostat has five different ports: coolant exhaust, vacuum pump-out, electric feed through, BNC terminal, and a vacuum metering point. A vent gas heater is connected with the cryostat head to avoid freezing of electrical components when the cryogen is flowing through [156]. The sample cell was made of a brass block and was equipped with two parallel silicon windows (14 mm diameter) which were sealed with indium O-rings and fastened to the cell with flanges. The dimension of the cell was 48 mm in length and 12 mm in diameter. The cell was fastened to the cryostat cold head and suspended in a metal vacuum chamber fitted with two parallel KBr windows which were aligned to the cell windows. The vacuum chamber was placed inside of the sample compartment of the FT-IR spectrometer and was aligned with the infrared beam. The thermal isolation of the cell was achieved by evacuating the metal chamber ($< 10^{-6}$ torr). Two mechanical pumps in combination with one diffusion pump were used to get such a low vacuum. The cell was connected to the external gas handling system through a tiny stainless steel tubing of 3.17 mm diameter for the process of filling or emptying. A Scientific Instrument (Model 9650) temperature controller with an indicator was used to control and monitor the temperature of the cell. This unit feeds power to the heater resistance on the cryostat cold head and can hold and reproduce any dialed temperature from 300 K to 2 K. The temperature was measured with a sensor attached to the middle of the cell body. Figure 48 shows schematics of the cryostat, sample cell and vacuum chamber coupled with FTIR spectrometer.

3.2.3 Cryostat Operation

The operation of cryostat started with the filling of the 100 liter Dewar with liquid nitrogen. A transfer line bayonet was introduced inside the Dewar and securely fastened with a rubber sleeve and hose clamps. A steady and continuous flow of liquid nitrogen was

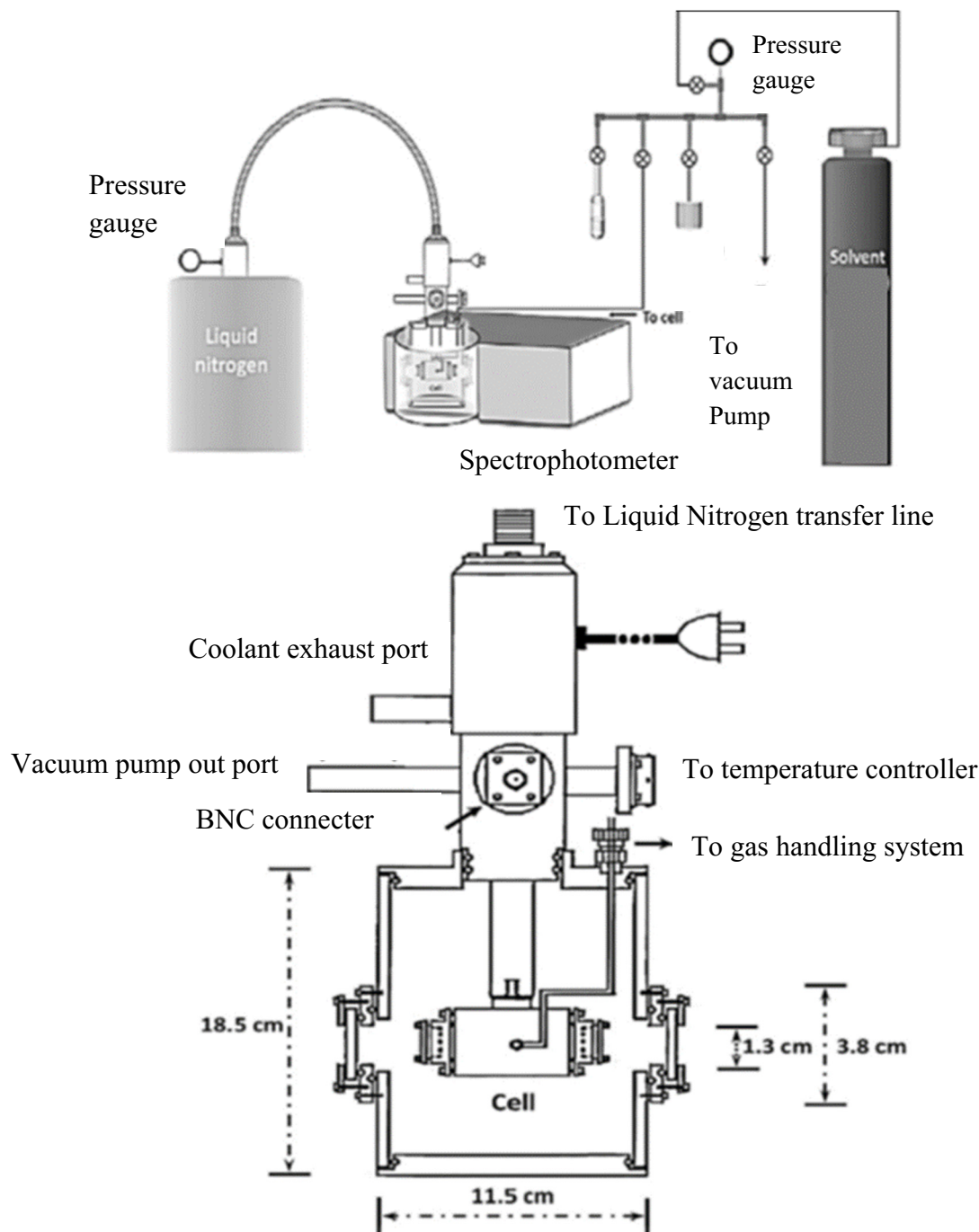


Figure 48. Schematics of the cryostat, sample cell and vacuum chamber used in FT experiments

maintained until the Dewar got full. The flow was controlled with pressurization which was driven by the appropriate connection to the laboratory nitrogen gas supply line. The adjusted pressure was about 5 psi. The pressure adjustment knobs (needle valve) on the cryostat head and both valves on flowmeters were opened to allow the flow of the liquid nitrogen. Normally, after 20 minutes or less, the cryogen started to flow through the transfer line to the cryostat cold head. At this point, the vent gas heater was plugged in to avoid freeze damage of the electrical components. The SI-9650 controller was turned on, providing a 25 V setting for the heater output voltage.

3.2.4 Collecting the Data

The process of the collection of the data was initiated with getting the background of an empty cell with a specific resolution (1 cm^{-1}) and number of scans (100) at room temperature. The sample was introduced into the cell at room temperature and the pressure was measured with a Barocel Pressure Sensor (600A). The C-H absorption spectrum of the sample was collected by choosing the background collection file of the empty cell. After that, the cell was evacuated, closed and cooled down to about 100 K. Once the cell gets cooled down to required temperature, the process of filling of the cell with liquid argon was started. The argon gas from the tank was passed through a copper spiral which has 12 loops of copper tubing with one-quarter-inch diameter. The portion of the last loop of the spiral was immersed in liquid nitrogen, which helps with the further reduction of the concentration of water and CO_2 in argon gas. Then, the argon gas was introduced into the cell through the gas handling system with a back pressure of 25-30 psi and it immediately started condensing in the cell. When the cell was filled and the temperature was stabilized at a desired value, the background data of the cell with liquid argon was collected.

The cell was then evacuated and warmed up to room temperature. The cell was filled with a certain amount of sample, closed, and cooled down to 100 K. The argon gas was passed to the cell with the same process as described above. The passing of the argon gas with a back pressure of 25-30 psi and its immediate condensation caused great turbulence inside the cell, which helped to dissolve the sample without additional stirring. When the desired temperature of the cell was stabilized and the solution reached equilibrium (usually within 30 min), the IR spectrum of the sample was obtained with the background spectrum of liquid argon.

3.2.5 Experimental Shutdown

The experimental shutdown process is started with the slow evaporation of the sample by carefully opening of the Swagelok for the vacuum line. The temperature was dialed at 200 K and the flow of cryogen was stopped by closing the two valves on flow meter, the valve of laboratory nitrogen line and the regulator of the cryogenic tank. Once, the solution was warmed to 200 K, a temperature of 295 K was dialed. By the time of warming to room temperature, the cell got completely empty. After that, the vent gas heater was unplugged and the bayonet of the transfer line was carefully removed from the Dewar. At the end, the light source was turned off and the OMNIC software window was closed.

3.2.6 Calculation of Mole Fraction

After the spectral data obtained, they were fitted with the solubility model equation: $\frac{1}{I_A} = \frac{a}{C} + b$ or $I_A = \frac{C}{a+bC}$ where I_A is the integrated absorbance, C is the concentration in ppm, and a, b are the fitting parameters. The integrated absorbance in cm^{-2} is represented by an equation:

$$I_A = \int a(v)dv \quad (34)$$

where, $a(v)$ is the absorbance as a function of frequency in wavenumber.

Similarly, the concentrations of the sample in solution were calculated as mole fraction (X), using the ratio of molar densities;

$$X = \frac{n_{solute}/V}{n_{total}/V} = \frac{n_{solute}}{(n_{solvent} + n_{solute})} \quad (35)$$

For very diluted solutions, $n_{total} \approx n_{solvent}$. By assuming the ideal gas approximation, the mole fraction (ppm) is calculated as;

$$X = \frac{P_i}{(RT_i\rho_{sol}(T))} \times 10^6 \quad (36)$$

where, P_i is the pressure of the sample in atm., R is the ideal gases constant in L atmK⁻¹mol⁻¹, T_i is the temperature of admittance of the solute (room temperature), and ρ_{sol} is the density of the solvent in mol/L at the temperature of the cryogenic solution.

3.3 C-H Infrared Absorption of 2-methyl-2-butene (C_5H_{10})

The Fourier transform infrared (FTIR) spectrometer coupled with a cryostat was used to study C-H fundamental transition of 2-methyl-2-butane in gas phase at room temperature and dilute solutions in liquid argon at 100 K. The structure of 2-methyl-2-butene is $CH_3-C=C(CH_3)_2$. The sample (C_5H_{10}) with a purity of 96 % was obtained from Wiley organics and the solvent argon gas with a purity of 99.9995 % was obtained from Matheson. Figure 49 presents the pressure series of 2-methyl-2-butene at room temperature. Because of the overlapping of the transition from different ways of orientation of C-H bonds in the molecule, spectra are not well resolved.

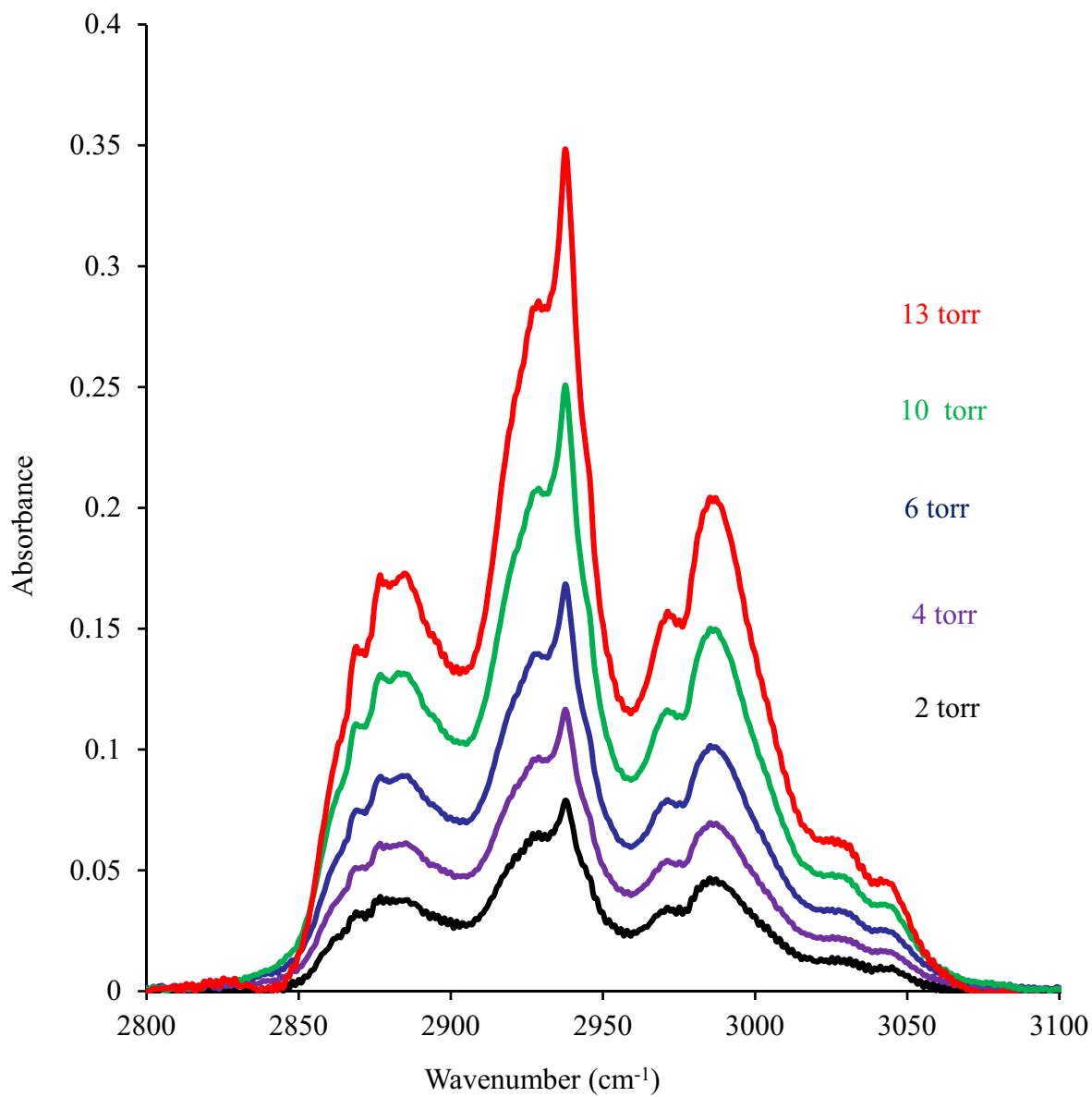


Figure 49. Pressure series of the spectral band of C-H fundamental transition of 2-methyl-2-butene in gas phase 298 K

We calculated an integrated area of spectral bands from 2800 cm⁻¹ to 3100 cm⁻¹ for various pressure of the sample. Table 23 presents the integrated area of spectral band of gas sample at 298 K. Figure 50 shows the plotting of integrated area of the spectral bands versus pressure where the integrated area increases with increase in pressure of the sample.

Table 23. Integrated Area of Absorbance of Spectral Band of C-H Fundamental Transition of 2-methyl-2-butene at 298 K

Pressure (torr)	Int. area of absorbance
2	10.29
4	15.19
6	22.21
10	27.14
13	29.56

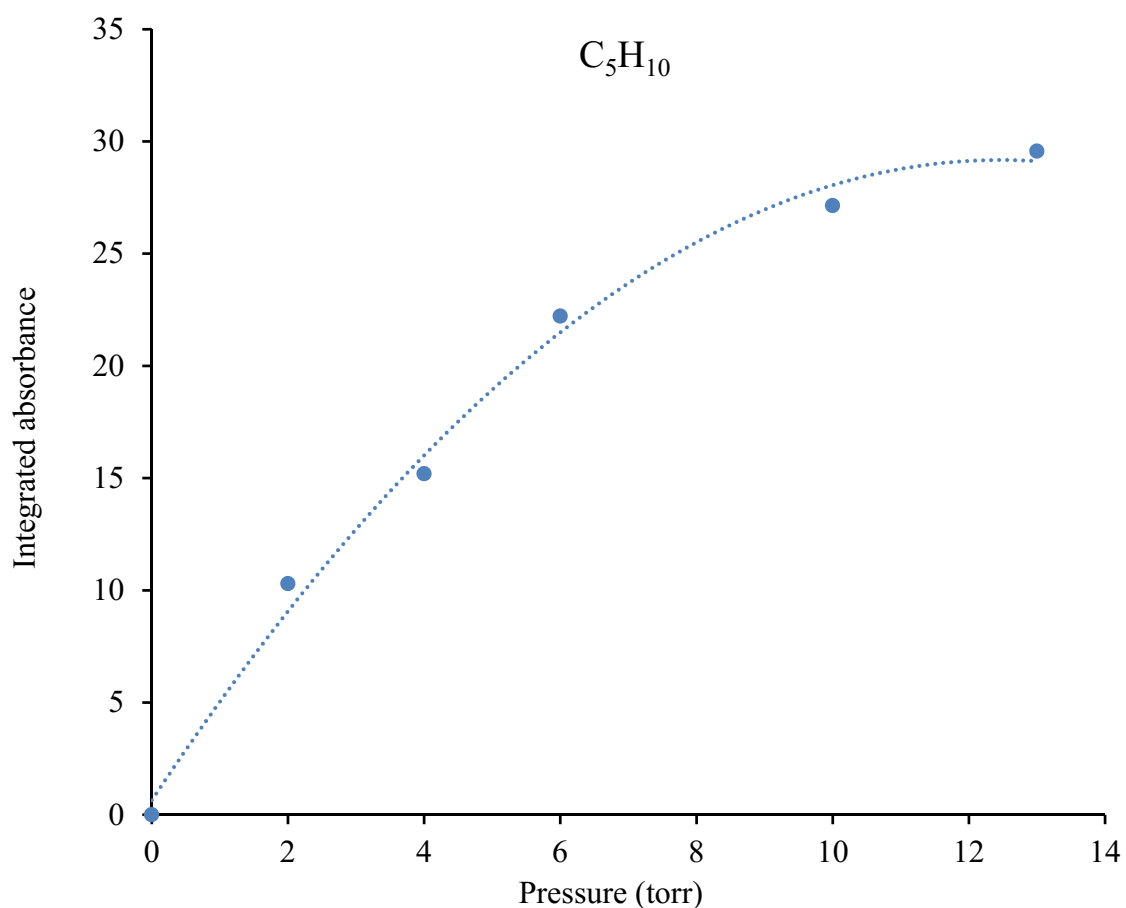


Figure 50. Integrated area of gas phase spectral band of C-H fundamental transition of 2-methyl-2-butene versus pressure at 298 K

In this project, our major focus was on the solution phase spectrum at cryogenic temperature. We obtained the spectra of various concentrated solutions of 2-methyl-2-butene in liquid argon at 100 K. Figure 51 depicts the concentration series of C-H stretching region of the spectrum ($2800\text{-}3100\text{ cm}^{-1}$) of 2-methyl-2-butene in liquid argon solutions at 100 K. From the comparison of the solution phase spectrum (Figure 51) with the gas phase spectrum (Figure 49) of 2-methyl 2-butene we observed that the solution phase spectrum was far more informative than the gas phase spectrum. The spectra were very sharp, more resolved and less frequency shifted.

In cryogenic solutions, there is very weak interaction between the gas and solvent molecules which helps to avoid the overlapping of the bands which is a major problem in the room temperature gas phase spectrum. Furthermore, the rotational band envelope collapses because of the low temperature and obstacle in rotations of the sample molecules in solvent. As a result, we can observe more bands that are hidden in gas phase spectra due to the rotation congestion [149, 152]. To predict the solubility, we obtained an integrated absorbance of spectral band of C-H fundamental transition of 2-methyl-2-butene for the several compositions until the magnitude of the integrated absorbance reached a maximum value and indicating the saturation. Integration of the spectral band has been carried out in the spectral regions ($2800\text{-}3100\text{ cm}^{-1}$). Table 24 presents the integrated area of spectral bands for various concentrated solution in liquid argon at 100 K. The solubility was obtained by plotting the integrated absorbance of the spectral band as function of the mole fraction (ppm) which is shown in Figure 52. For unsaturated solutions, the integrated absorbance increases linearly with the mole fraction whereas for saturated solutions the integrated absorbance is approximately constant.

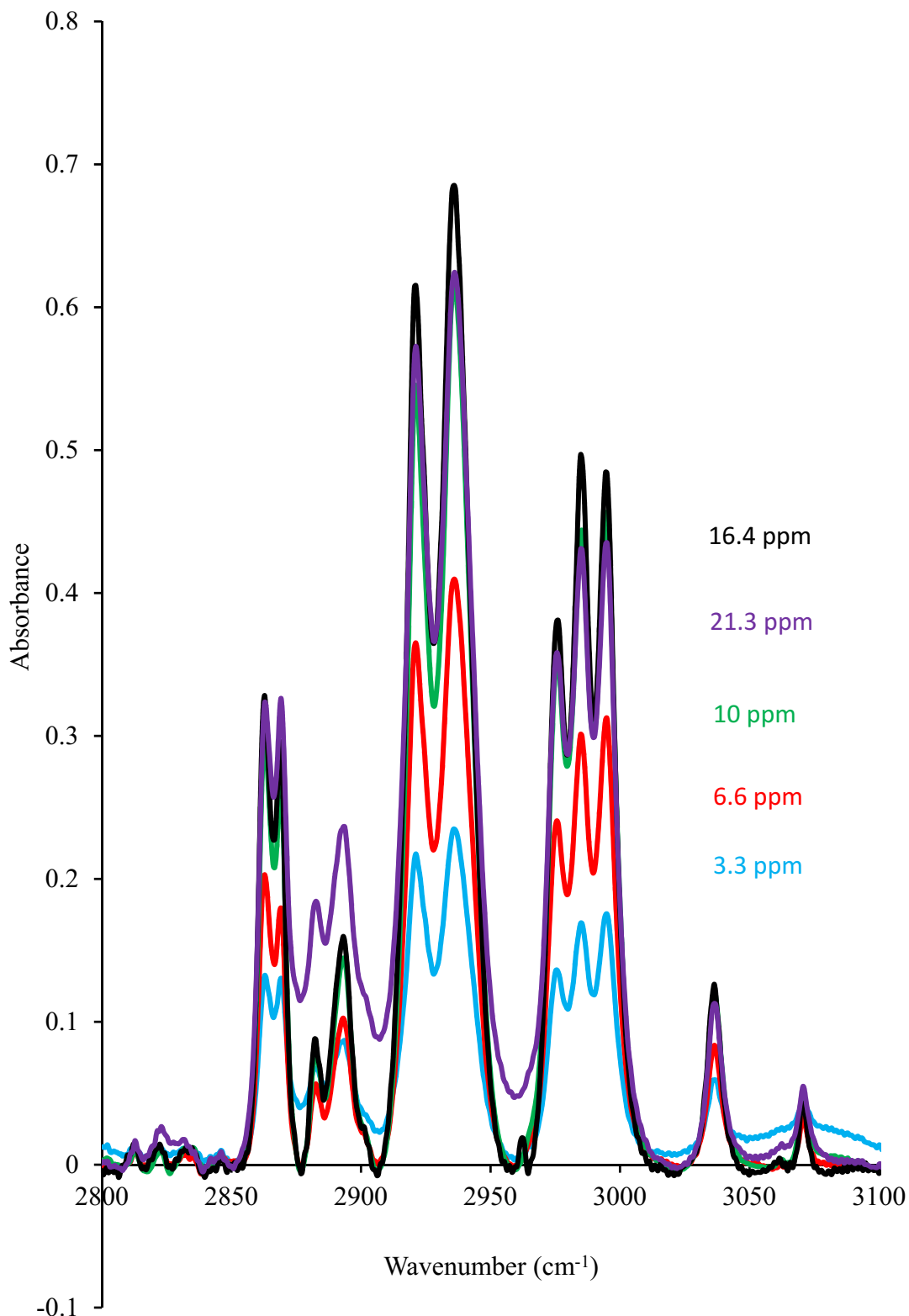


Figure 51. Concentration series of spectral band of C-H fundamental transition of 2-methyl-2-butene solutions in liquefied argon at 100 K

Table 24. Integrated Area of a Band of C-H Fundamental Transition of 2-methyl-2-butene

Mole fraction (ppm)	Integrated area
3.3	16.043
6.6	21.22
9.9	31.008
16.4	32.853
21.3	31.495

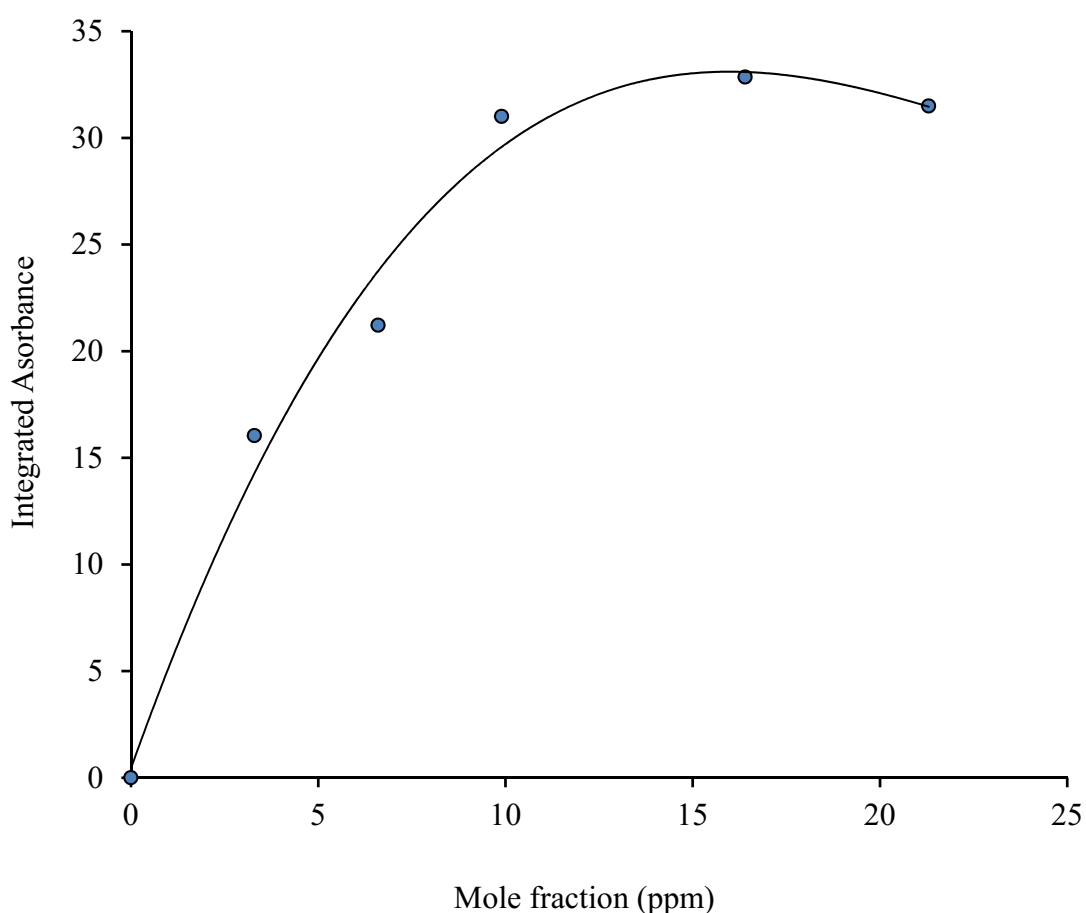


Figure 52. Plot of integrated absorbance of spectral band of C-H fundamental transition of 2-methyl-2-butene solution in liquefied argon versus mole fraction (ppm) at 100 K

The intersection of the two straight lines was taken as the solubility at the temperature of the experiment. The approximate solubility is (9 ± 5) ppm at 100 K.

3.4 C-H Infrared Absorption of Methyl-acetylene (Propyne)

Similarly, we recorded an absorption spectra of saturated and unsaturated concentrated solution of propyne in liquid argon at 100 K. Several spectra were taken for each solution to make sure that the intensities of the bands did not change and the concentration of the sample in solution was under equilibrium conditions. Normally, we took the time range of 4 hours for each solution for obtaining several spectra. Figure 53 shows the \equiv C-H stretching bands of propyne as a function of the wavenumber (3310-3340 cm^{-1}) for four different concentrations. The band in the spectra at 3329 cm^{-1} has been assigned as the C-H acetylenic (ν_1) of $\text{CH}_3\text{-C}\equiv\text{C-H}$. We obtained an integrated absorbance of spectral band. Integration of the spectral band has been carried out in the spectral regions (3310-3340) cm^{-1} . Table 25 presents the integrated area of spectral bands for various concentrated solutions in liquid argon at cryogenic temperature.

Table 25. Integrated Area of a Band of C-H Fundamental Transition Methyl-acetylene Solutions in Liquefied Argon at 100 K

Mole fraction (ppm)	Integrated area
8.2	0.412
41	1.032
82	1.126
123	0.964

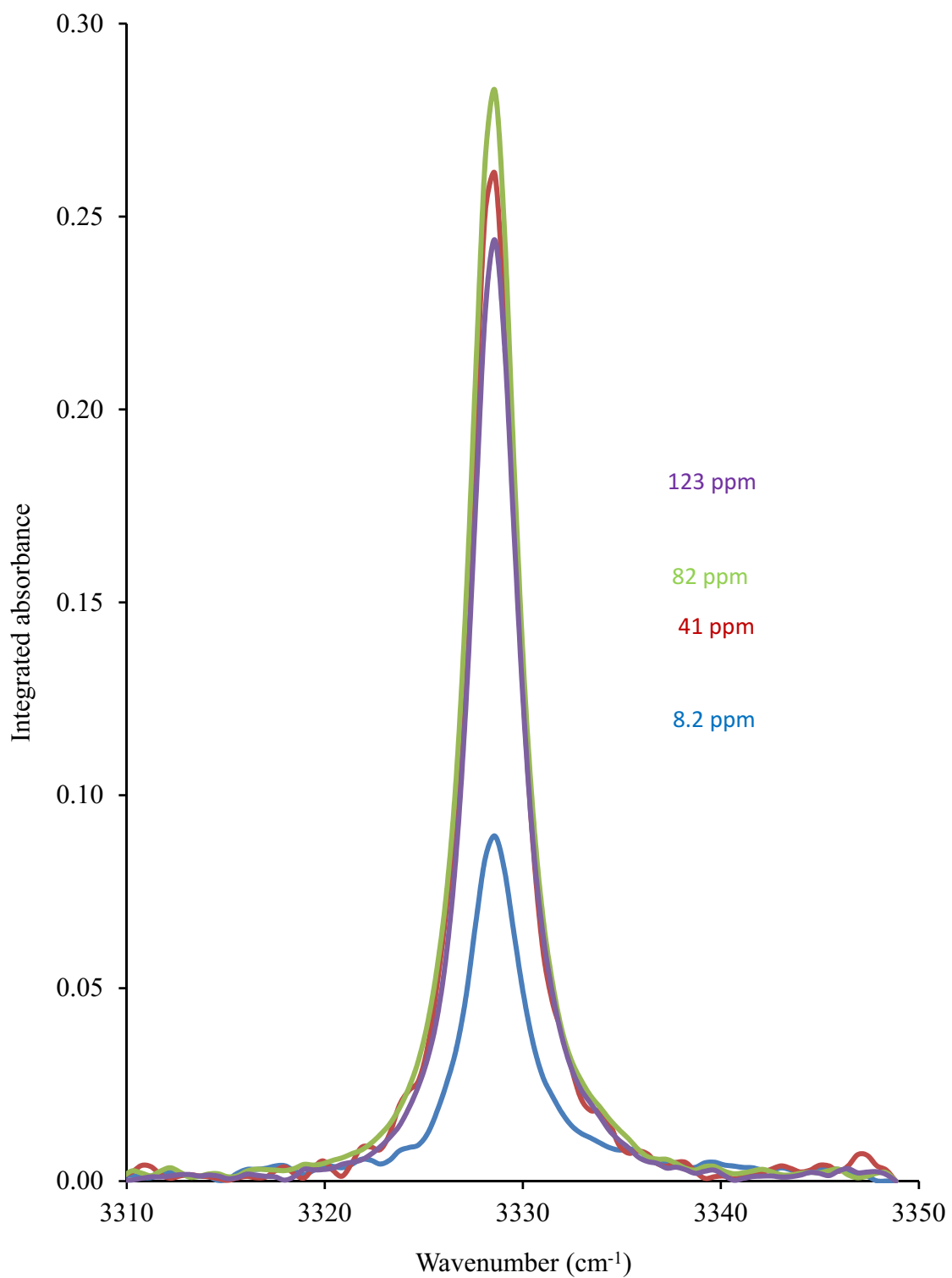


Figure 53. Concentration series of spectral band of $\equiv\text{C}-\text{H}$ fundamental transition of methyl-acetylene solutions in liquefied argon at 100 K

A plot of integrated absorbance as a function of the mole fraction (ppm) is depicted in Figure 54. The approximate solubility is (22 ± 9) at 100 K.

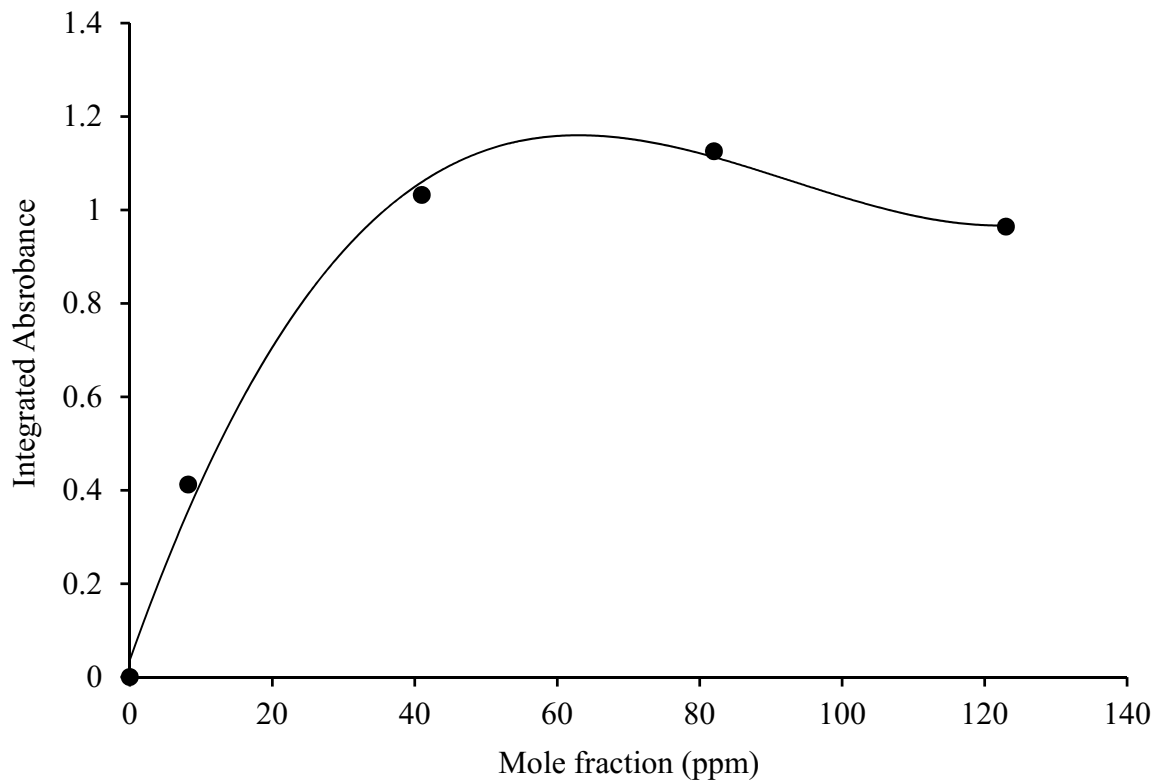


Figure 54. Plot of integrated absorbance of spectral band of C-H fundamental transition of methyl acetylene solution in liquefied argon versus mole fraction (ppm) at 100 K

3.5 Interpretation of the Experimental Data with Thermodynamic Frame Work

Proper estimation of solubility of solid in liquid solvent at low temperature is of prime importance for the design of cryogenic processes. The experimental results only, are not adequate to do so. In order to make prediction with confidence, it is necessary to interpret and correlate experimental data within the thermodynamic frame work [163]. The experimental solubility values at the corresponding temperature were used with solubility parameters of the two separate models: The Perturbed-Chain Statistical Associating Fluid Theory (PC-SAFT) and Regular Solution Theory (RST).

3.5.1 PC-SAFT Model

In order to estimate the experimental solubilities of a solute with a theoretical model, we have implemented an approach similar to the one used by Cordier et al [169,170]. This method assumes a thermodynamic equilibrium between the solid phase of the considered species (2) and the quantity of matter of the same compound, dissolved, here in liquid argon (1). The theoretical transcription of such an equilibrium is written as the equation:

$$\ln \Gamma_2 x_{2,\text{sat}} = - \frac{\Delta H_{2,m}}{RT_{2,m}} \left(\frac{T_{2,m}}{T} - 1 \right) \quad (37)$$

Where, $X_{2,\text{sat}}$ is the mole fraction of the solute (2) at saturation, Γ_2 is the activity coefficient, $T_{2,m}$ is the melting temperature and $(\Delta H_{2,m})$ is the enthalpy of melting of the considered species. The temperature of the system is denoted T , and $R= 8.314 \text{ J/mol K}$ is the gas constant. This relation can be found in the textbook by Poling et al. [171] and in Cordier et al. [169,170]. The validity of Eq. (37) is discussed. The activity coefficient (Γ_2) that takes into account the effect of the solvent, is calculated in the frame of the Perturbed Chain Statistical Association Fluid Theory (PC-SAFT) [172] which has been proven to be one of the most powerful equations of state for the liquid and vapor states. This theory has been used in many calculations related to the thermodynamics of solutions. For this application to solid-liquid equilibrium, the activity coefficient is written as the ratio $\Gamma_2 = \phi_2^L / \phi_2^{L,0}$ where, ϕ_2^L is the fugacity coefficient of the solute (2) and $\phi_2^{L,0}$ is fugacity coefficient of the pure subcooled liquid solute. In the frame of the PC-SAFT, molecules are considered as chains of segments where each molecule is characterized by its pure component parameters: the number of segments m , the segment diameter σ (Å) and the energy of interaction ϵ/K_B (K). The PC-SAFT is extended to mixtures using the Berthelot-

Lorentz combining rule for the dispersive energy, resulting in a single binary parameters k_{12} . The value of the parameters m , σ , and ϵ/K_B were estimated using the group contribution method developed by Tihic et al. [173]. The corresponding values are given in Table 26 and Table 27. The experimental solubilities were reproduced by adjusting the interaction parameter k_{12} . The interaction parameters obtained are valid only for the temperature used for the determination, since, the parameter is temperature dependent.

Table 26. Individual PC-SAFT Parameters of Compounds

Compound	Temperature (K)	$\Delta H_{2,m}$ (J/mol)	$T_{2,m}$ (K)	Molar mass (g/mol)	Segment (m)
C ₃ H ₄	100	5348.0	170.4	40.06	1.8167
C ₅ H ₁₀	100	7579.0	139.4	70.13	2.4470

Table 27. Individual PC-SAFT Parameters and Derived Interaction Parameters from Experimental Solubility at 100 K

Compound	σ	ϵ/K_B	Solubility	k_{12}
C ₃ H ₄	3.4710	229.66	~ 22	0.143
C ₅ H ₁₀	3.7800	243.90	~ 9	0.119

3.5.2 Regular Solution Theory

In regular solution theory (RST) or Preston–Prausnitz solubility model, [171,174] the solubility term ($\ln \Gamma_1 x_{2,sat}$) is calculated using Eq. 37 with the values for $\Delta H_{2,m}$ and T_{2m} for molecules from Yaws [175]. The activity coefficient is given by:

$$\ln \Gamma_2 = \frac{V_2 \Phi_1^2}{RT} [(\delta_1 - \delta_2)^2 + 2l_{12} \delta_1 \delta_2] \quad (38)$$

The molar volume of the solute is V_2 , the volume fraction of the solvent in solution is Φ_1 , the solubility parameters are δ_1 (solvent) and δ_2 (solute). The term l_{12} is an interaction constant characteristic of a solvent-solute pair. Instead of calculating solubility parameters (δ_i) from the molar enthalpy of vaporization (ΔH°) the temperature T and the liquid volume (V^L) of the component i (1,2) the method used by Preston-Prausnitz [174] is adopted. In order to find the reduced molar volumes of the solvent and solute, the reduced volume (V_R) surface corresponding to the Table (A-1) given by Preston and Prausnitz [174] was fitted to a two-dimensional polynomial with the variables: reduced temperature (T_R) and Pitzer's acentric factor (w) [175]. The polynomial is:

$$\begin{aligned} V_R(T_R, w) = & 0.3236 + 0.1762T_R - 0.1564w - 0.3896T_R^2 \\ & + 0.004791T_Rw + 0.03122w^2 + 0.4611T_R^3 \\ & + 0.1839T_R^2w - 0.1408T_Rw^2 + 0.02778w^3 \end{aligned} \quad (39)$$

Once the reduced volumes are calculated for solvent and solute, the molar volumes V_1 and V_2 from $V_i = (V_R * V_c)_i$ ($i = 1$ or 2) are obtained. Similarly, in order to find the reduced solubility parameters of the solvent and solute, the reduced solubility (δ_R) surface corresponding to Table (A-2) given by Preston and Prausnitz [174] was fitted to a two-dimensional polynomial with the variables: reduced temperature (T_R) and Pitzer's acentric factor (w) [175]. The polynomial is:

$$\begin{aligned}
\partial_R(T_R, w) = & 1.3 + 2.01w - 0.561T_R - 2.009w^2 - 0.9183wT_R \\
& + 0.4607T_R^2 + 0.06944w^3 + 3.102w^2T_R \quad (40) \\
& - 1.054wT_R^2 - 0.6481T_R^3
\end{aligned}$$

After the reduced solubility parameters are calculated for solvent and solute, the solubility parameters δ_1 and δ_2 from $\delta_i = (\delta_R^*(P_c)^{1/2})_i$ are obtained. Table 28 gives the values of critical constants and calculated parameters for the solutions of argon with the solute molecules at the temperature of the experiment. Table 29 shows the interaction parameter (l_{12}) that reproduces the experimental solubility of each solution.

Table 28. Molar volumes (V_i) and Solubility Parameters (δ_i) at 100 K

Parameters	Solvent (1)		Solute (2)
	Ar	C ₃ H ₄	C ₅ H ₁₀
T _c (K)	150.7	402.4	470
P _c (atm)	48.0	57.0	34.7
V _c (cm ³ /mol)	75.2	163.5	292
W	-0.002	0.212	0.287
T _R	0.66	0.25	0.21
V _R	0.4029	0.3201	0.3065
V ₁ (cm ³ /mol)	30.30
V ₂ (cm ³ /mol)	52.33	89.50
δ _R	0.94	1.49	1.59
δ ₁ (cal/cm ³) ^{1/2}	6.51
δ ₂ (cal/cm ³) ^{1/2}	11.25	9.37

Table 29. Interaction Parameters (l_{12}) Calculated from Experimental Solubility at 100 K

Parameter	C ₃ H ₄	C ₅ H ₁₀
l_{12}	0.06	0.1
X ₂ ^(calc.) ppm	~19	~8
X ₂ ^(exp.) ppm	22 ± 9	9 ± 5

3.6 Comparison with Literature Study

A summary of our results in liquid Ar compared with results with other solvents and techniques at similar temperatures is presented in Table 30. Different methods of analysis require the initial preparation of a saturated solution in equilibrium with the crystals of solute (static analytic method) followed by separation of an amount solution (filtrate). Analysis of the filtrate by evaporation is sometimes used to determine the solute concentration in the original solution. The saturated solution can also be analyzed by spectroscopic methods (IR or UV) or by chromatography. Another method is the analytic-optical method (or visual) is one where the solute-solvent mixture is prepared in the gas phase and deposited as a liquid in a transparent cell. If a solid solute is observed in the liquid, the temperature is increased until the solid disappears indicating solubility at the registered final temperature. We believe, this is the first time that the solubility of 2-methyl-2-butene in liquid argon 100 K has been measured. However, the solubility propyne in liquid Ar has been reported in the range from 2.3×10^{-6} (90 K) to 8.5×10^{-6} (100 K) [176]. The value at 100 K is approximately 2.6 times smaller than the one reported here.

Table. 30 Experimental Solubilities of the Unsaturated Hydrocarbons in Cryogenic Liquid

Solute	Temperature (K)	Liquid Solvent	Mole fraction	Method
2-methyl-2-butene	100 K	Ar	$(9 \pm 5) \times 10^{-6}$	This work
Methyl-acetylene (Propyne)	100 K	Ar	$(22 \pm 9) \times 10^{-6}$	This work
	100 K	Ar	8.5×10^{-6}	IR (Ref.176)

The PC-SAFT and RST models also use equation 37 to calculate the activity coefficient of the solute in the saturated solution. The difference between the two theories begins with the calculation of the activity coefficient. The RST provides good preliminary results for binary solutions of non-polar components. By including an interaction parameter (l_{12}), the real behavior for solutions is considered. In this paper, the two polynomial equations (39,40) that reproduce the values in tables given by Preston and Prausnitz[174] are presented in order to facilitate calculations of the solubility parameters δ_1 and δ_2 . The SRT model has been used in our laboratory to estimate concentrations of solutes in saturated solutions of cryogenic solvents before experiments are done. The equation of state PC-SAFT is derived from statistical physics. Solvent and solutes are represented by parameters related to their individual molecular properties. It has been proven to be a more realistic representation for the liquid and vapor states and it is also an excellent method for the simulation of multi-component solutions. Both methods (PC-SAFT and RST) require

a temperature dependent interaction parameter k_{ij} (PC-SAFT) and l_{ij} (RST) that is usually derived from experimental data.

3.7 Conclusion

The infrared spectroscopy of unsaturated hydrocarbons, 2-methyl-2-butene and methyl-acetylene in liquid argon solution has been studied. The solubility of the compounds was obtained from the study of integrated absorbance of C-H transition as a function of mole fraction in liquid argon solution. Spectra were obtained at increasing solution composition until the magnitude of the integrated absorption band reached a maximum value, indicating a saturated solution. The approximate experimental solubilities are (9 ± 5) ppm at 100 K for 2-methy-2-butene and (22 ± 9) ppm at 100 K for methyl-acetylene. The experimental solubility values at the corresponding temperature were used to obtain solvent-solute interaction parameters k_{12} (PC-SAFT) and l_{12} (RST) for each solute in the presence of argon as the solvent. Data from experimental measurements are important for more realistic simulations of solubility of solids in cryogenic liquids.

APPENDICES

APPENDIX A

A.1 Remote Control and Data Acquisition Systems

The process of tuning of wavelength of dye laser and data acquisition were performed simultaneously by using LabVIEW programming. The wave length tuning started with the movement of the micrometer position which was driven with stepper motor control. The voltage signal acquisition was carried out by using the phase sensitive lock in amplifier. In this appendix, we are trying to cover the programs or virtual instruments (VIs) which were used to execute remote control operation of the spectrometer.

A.2 Computer Hardware

In both instrumental technique, phase-shift cavity ring down spectroscopy (PS-CRD) and thermal lens spectroscopy (TLS), the signal was collected by using two different computer cards. The data acquisition card (DAQ PCI-6025E) which was connected to the mother board inside the computer and sends an analog wave form pulse to move the stepper motor by one step. The pulse amplitude should be not less than 5 V and not higher than 10 V. Another board (CB50LP) with connector panel was used for the communication in between the DAQ card and stepper motor. National instrument GPIB-USB-HS device was connected with GPIB connecter in lock-in amplifier to read out the lock in voltage signal in the computer.

A.3 PS-CRD LabVIEW Software Programs

LabVIEW is one of the important graphical programming languages. It provides graphical environment to make easier connectivity between the ideas and actual coding.

The primary objective of the LabVIEW is to create the data acquisition systems by generating the programs called Virtual instruments (VI's). The VI which is in charge of coordinating all sub-VI's is called main VI where each task is performed in an orderly fashion. All the VI's are usually saved into a library (*.llb) which facilitates the process of execution.

Figure A.1 depicts the main measurement panel wiring diagram for the data acquisition system in which all the components of the program are connected and ordered in the sequence that the computer can easily follow and execute. The sequence followed by the program is:

- 1) Move the step motor
- 2) Wait specified time
- 3) Take data points from the lock-in amplifier
- 4) Calculate the absorption
- 5) Write the data to a file
- 6) Repeat until the final position is reached

In the LabVIEW program, the DAQ VI is one of the essential VI which comprises various operations. At first, the process of data acquisition is started by moving the step motor. After stepping the motor, a predetermined amount of time (delay time) is provided to the lock in amplifier to respond to the signal. Now, the lock in amplifier acquire the data which is followed by the calculation of the ring down time (t) and the absorption using the equation discussed in the chapter one. After processing the data points the computer sends a signal back to the lock in amplifier for re-establishing communication. The collection of data points occurs until the final position set by the user is reached and finally the program

can stop. Figure A.2 shows the first sequence sub VI of the DAQ program. It initiates the process with the movement of the stepper motor by one step.

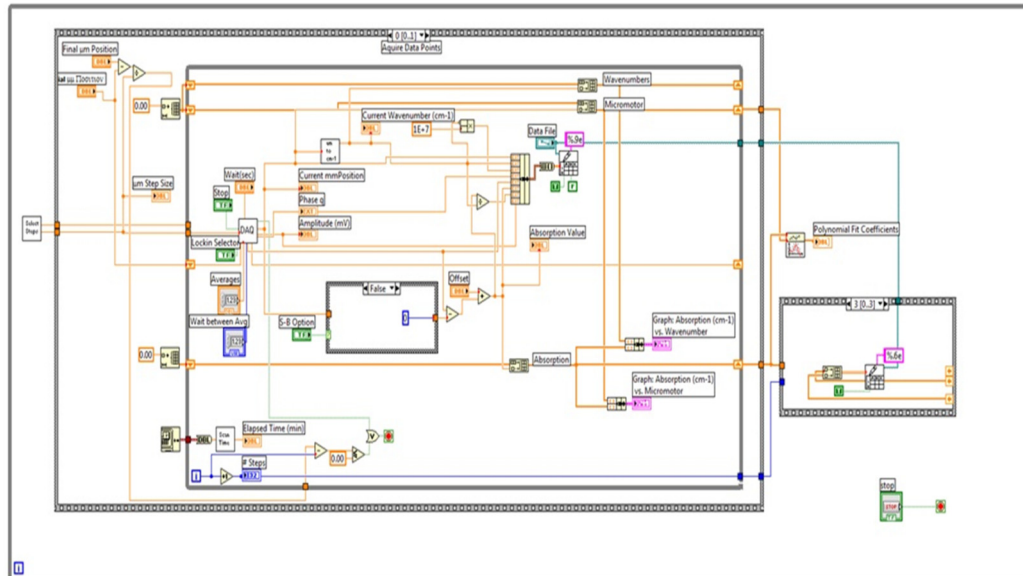


Figure A.1 Measurement Panel Wiring Diagram

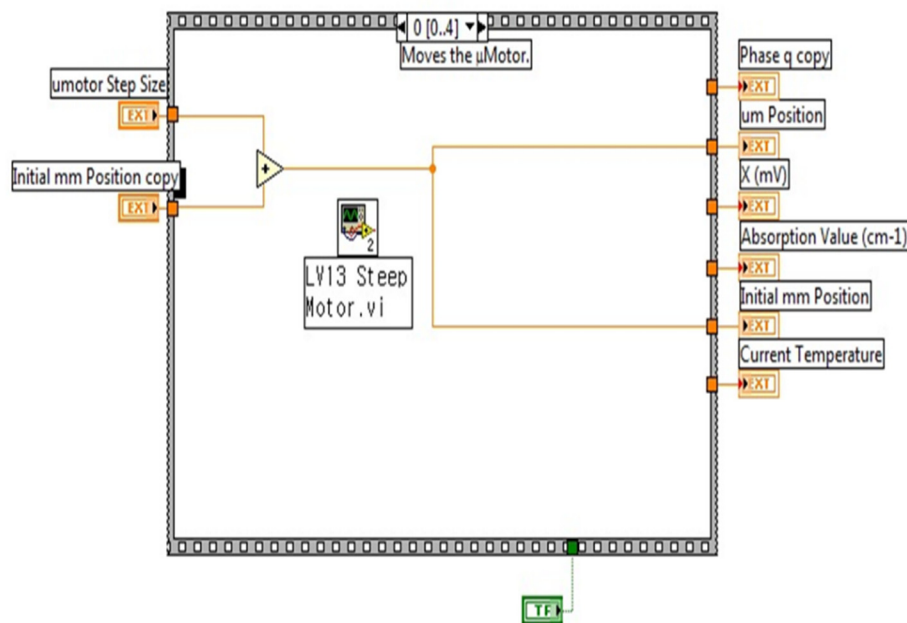


Figure A.2 DAQ Movement of the Motor

The second sequence is delay time sub VI as shown in Figure A.3 which notifies the program to wait a specified time before acquiring the data points and calculation of the absorption.

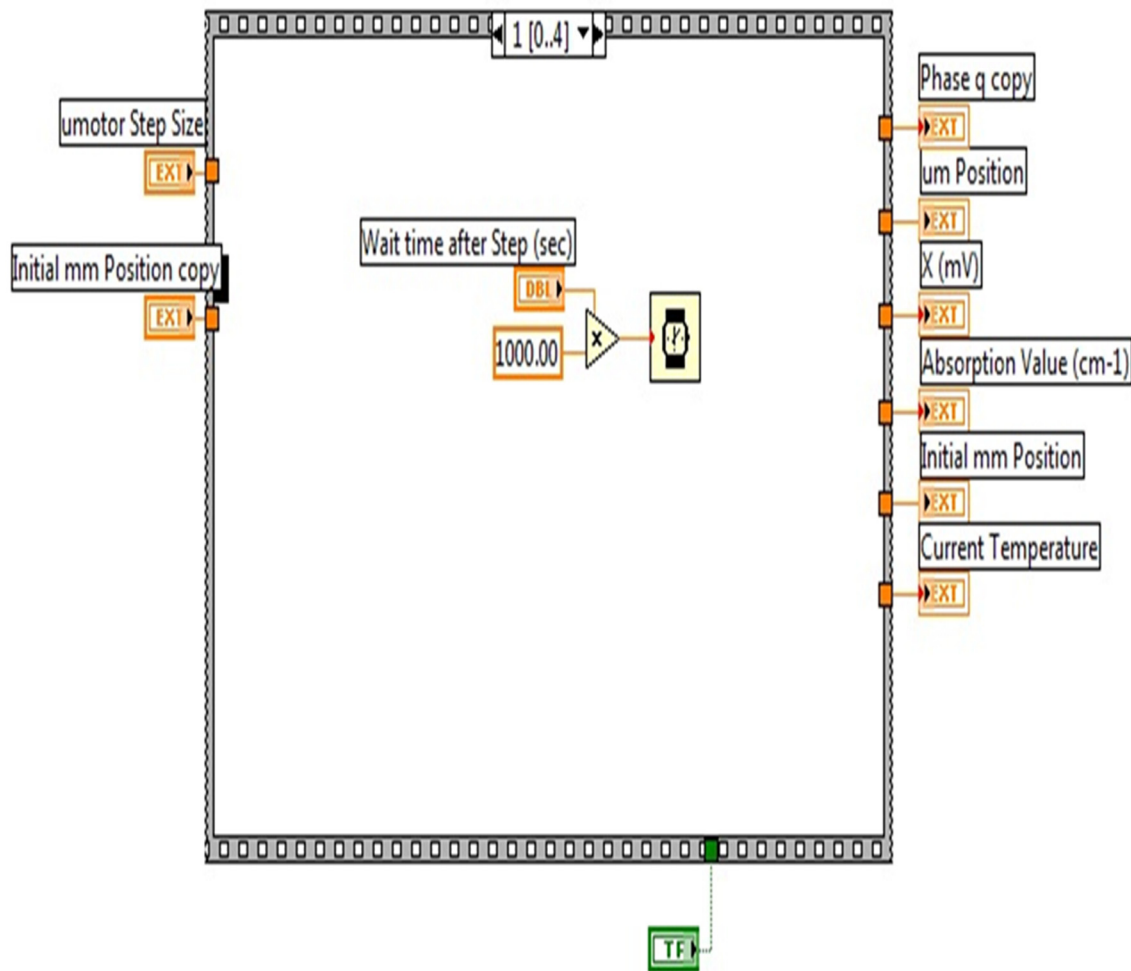


Figure A.3 Delay time

Figure A.4 shows Pscrd 830 snap VI which is in charge of communication with the lock-in amplifier and it separates string data into useable forms such as, X, Y, intensity in mV, phase angle and the reference frequency applied to the lock-in. This VI also has the setup for the calculation of the absorption as shown in figure A.6.

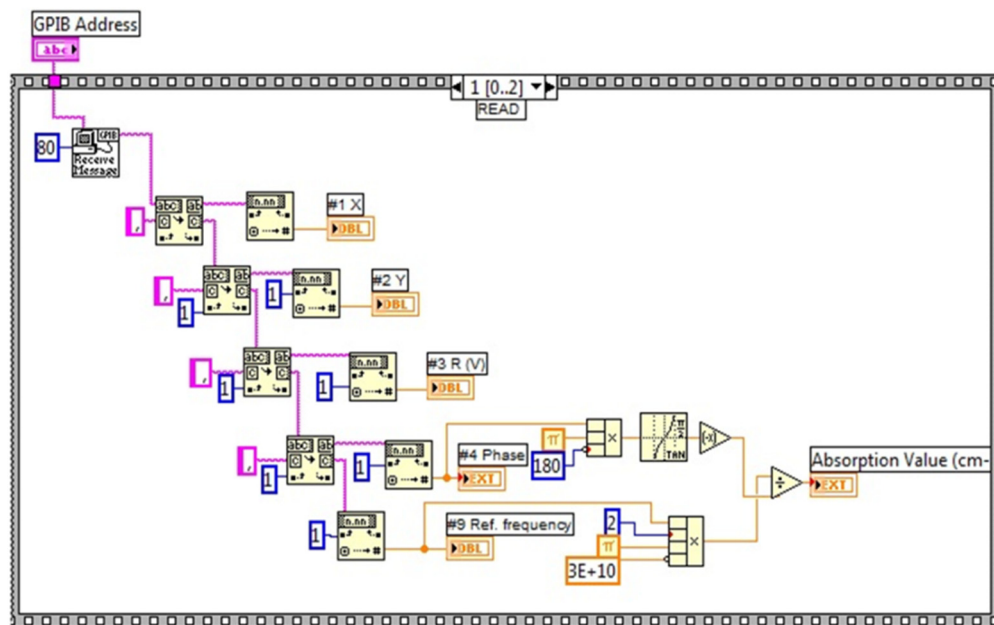


Figure A.4 Pscrd 830 Snap VI

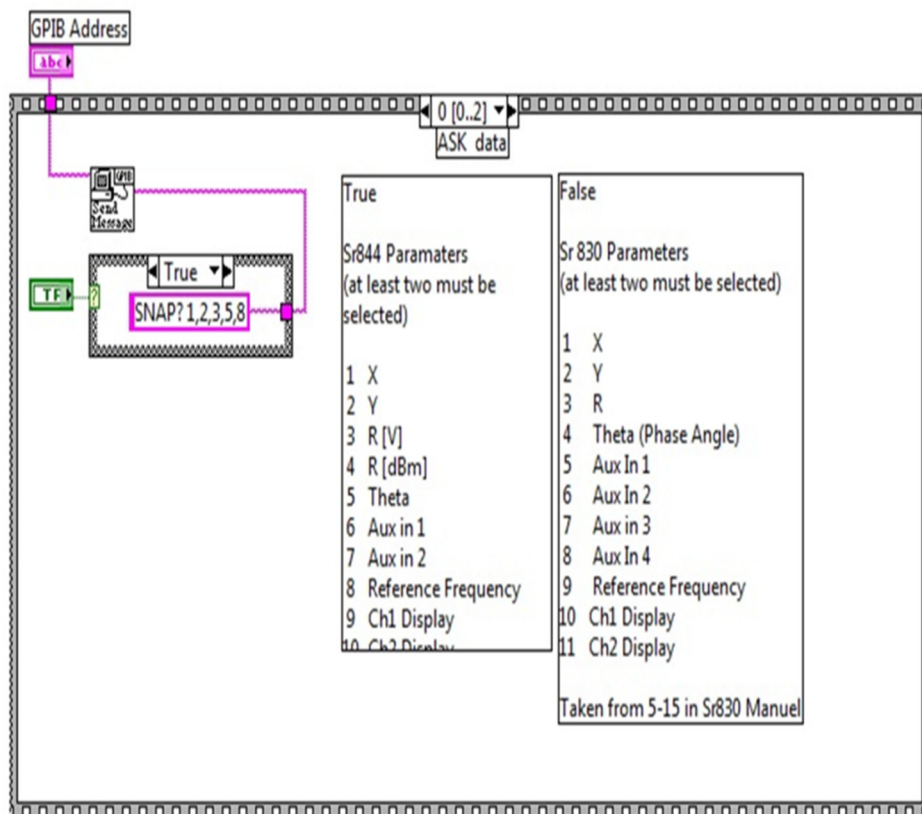


Figure A.5 Pscrd 830 Snap VI (Asking data)

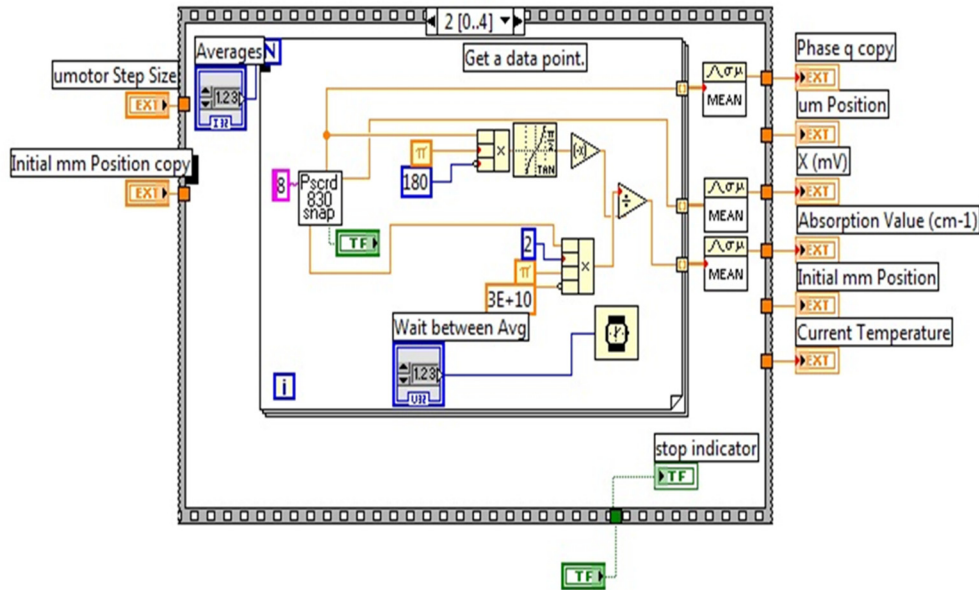


Figure A.6 Acquire data point and Calculated Absorption

Figure A.7 depicts the last sub VI which is wired to a button on the measurement panel and it is used to stop the data acquisition process. After that, all of the information collected in DAQ VI is sent to the measurement diagram where the data are assembled, processed and finally shown the main panel.

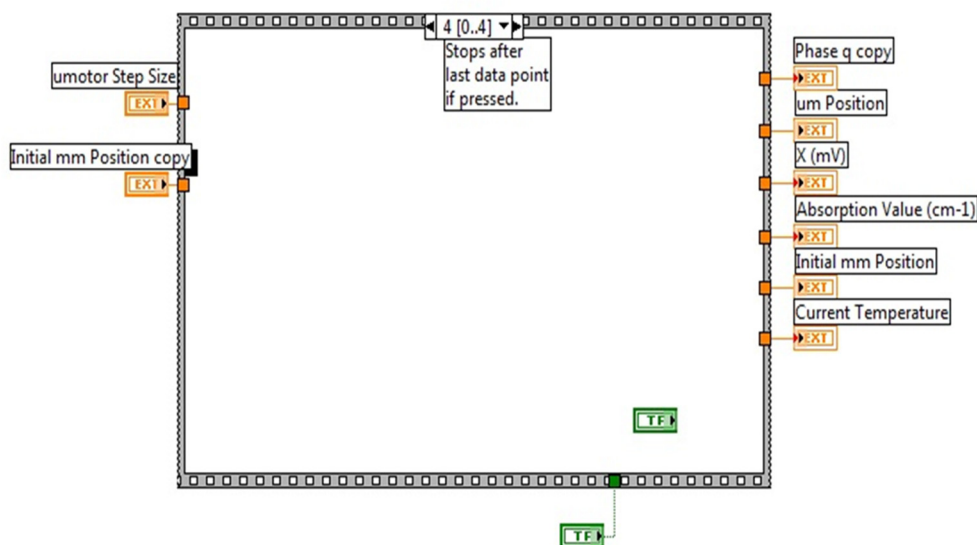


Figure A.7 Stop data collection

A.4 Thermal lens Spectroscopy (TLS) LabVIEW software program

A.4.1 Lock in Amplifier Interface (Get Volts.vi)

Acquisition of signal from the lock-in amplifier requires two important VIs: GPIB Write and GPIB Read. By specifying the GPIB address of the measuring device, the GPIB Write VI request information with specific commands. The commands are usually provided by manufacturer in their manuals. The instrumental communication can be checked by applying those commands. Similarly, once the instructions have sent to the instrument GPIB Read VI receives the information as chain of characters. Figure A.8 and Figure A.9 represent the sequence diagram for writing and reading respectively.

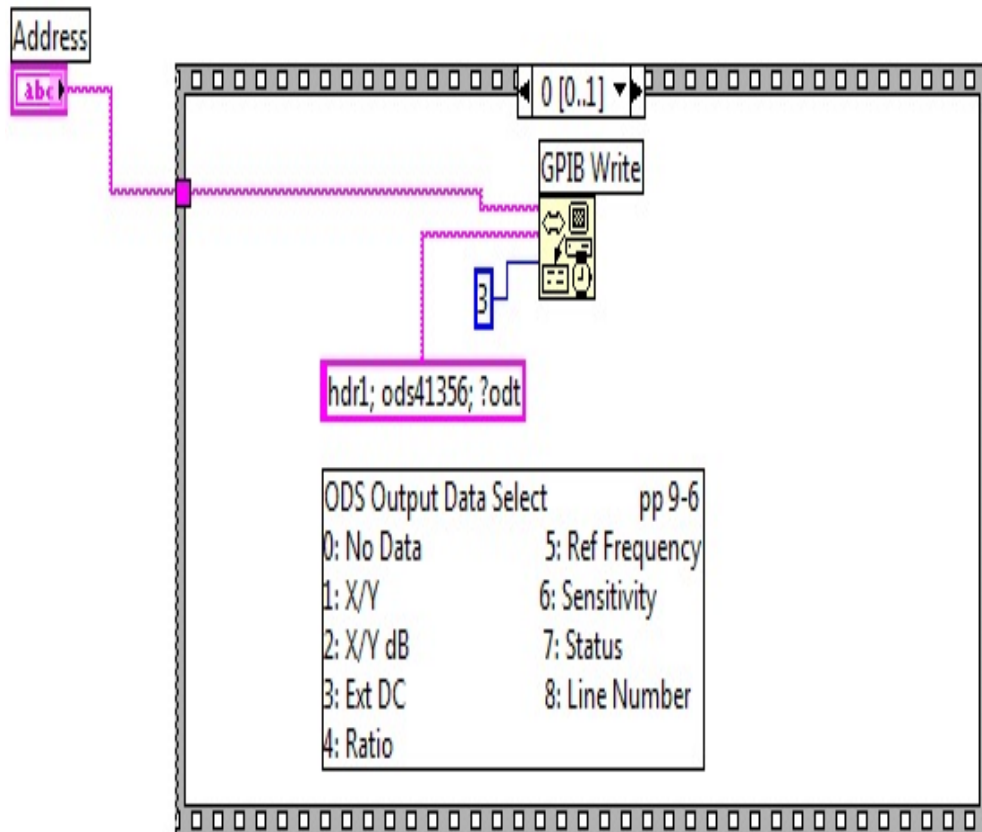


Figure A.8 Writing VI

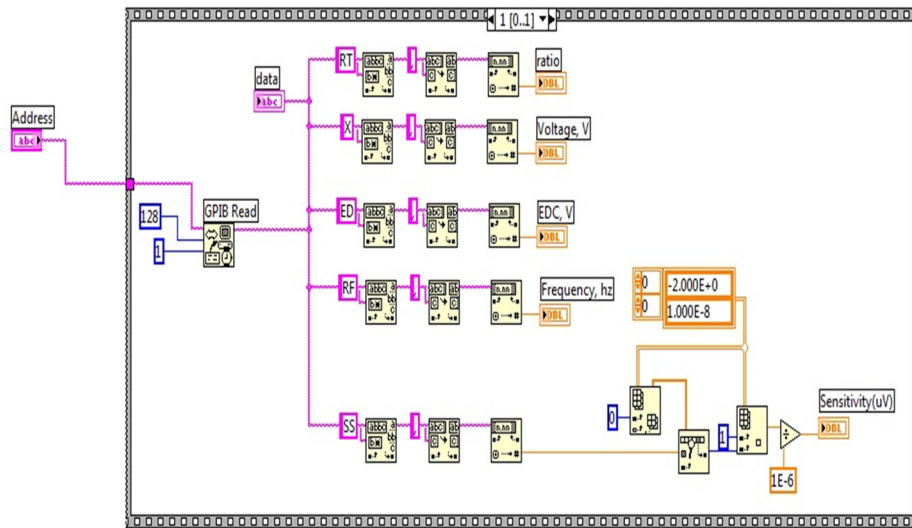


Figure A.9 Reading VI

A.4.2 Motor Control (Motor Cont. VI)

Figure A.10 shows the diagram which is responsible to move the step motor.

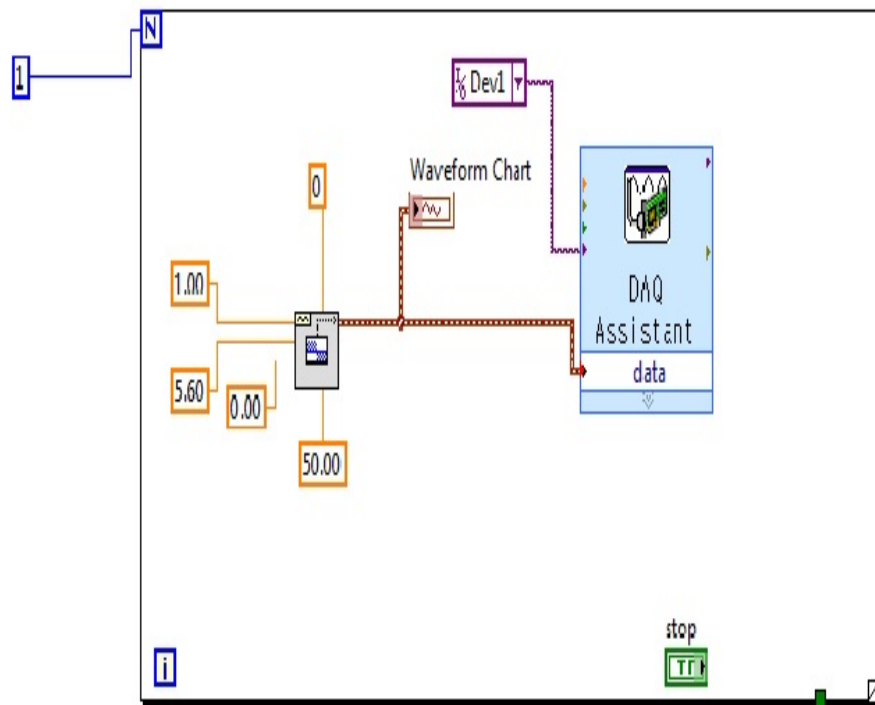


Figure A.10 Motor Cont. VI

In this VI, an Analog Output square wave pulse is generated and sending to the motor driver to make motor one step move. For that purpose we used DAQ Assistant in which we can specify the amplitude (V), waveform type (square), frequency (Hz), duration (ms) and square wave duty cycle (%).

A.4.3 Spectrum Display (Graph.vi)

Acquisition of the spectrum is carried out in real time against micrometer position. Since motor stepping is not repeatable every time, it is necessary to wait until the spectrum has been acquired to record the final micrometer position. Wavenumbers are then calculated using a calibration curve and assigned to each data point in the final spectrum. The individual steps in the VI are shown in Figure A.11.

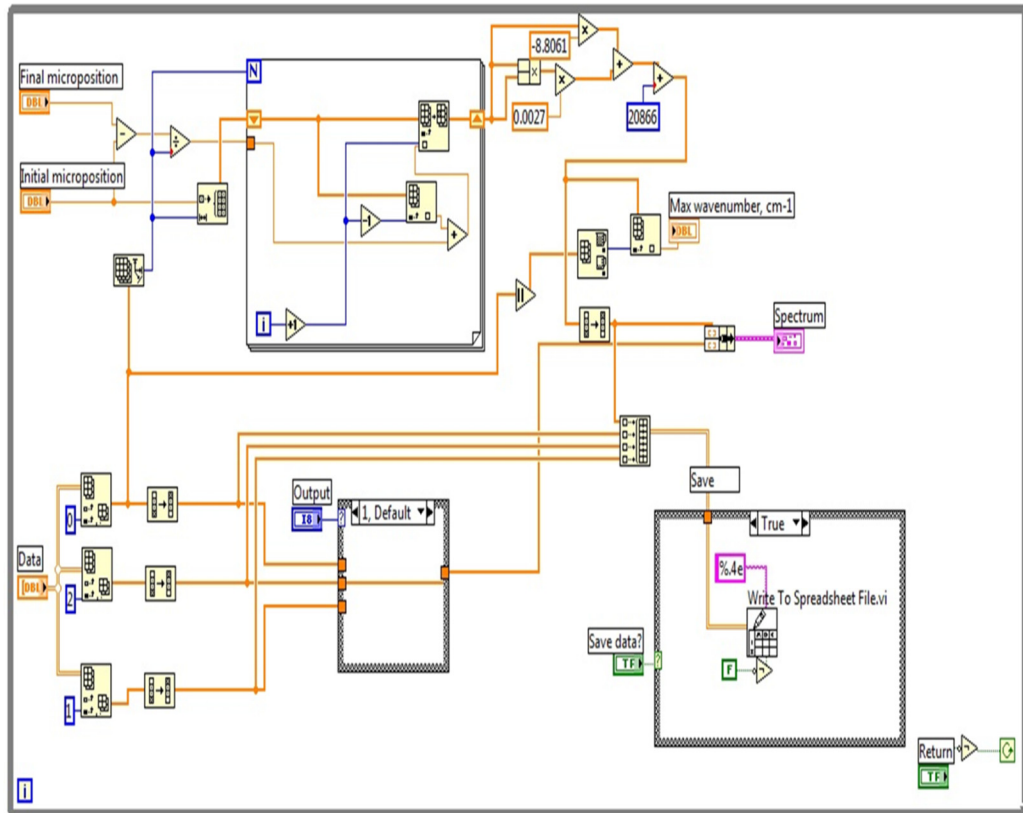


Figure A.11 Graph VI

A.4.4 Spectrum Acquisition (Main VI)

Figure A.12 depicts Main VI diagram in which programming is arranged in two frame sequences. The first, global acquisition contains and executes Get Volts VI, Motor Cont.VI and required time pause which are separately presented in Figure A.8, Figure A.9, Figure A.10 and Figure A.13 respectively. This sequence is repeated in a loop as many times as micrometer positions were calculated from the parameters that were specified in the control panel. When the micrometer reached to the final position and the process of data acquisition is stopped. The spectrum button is pressed to get an accessed to the second frame labeled global display as shown in Figure A.14 which allows seeing the spectrum. Finally, the return button is pressed to deactivate the Graph VI

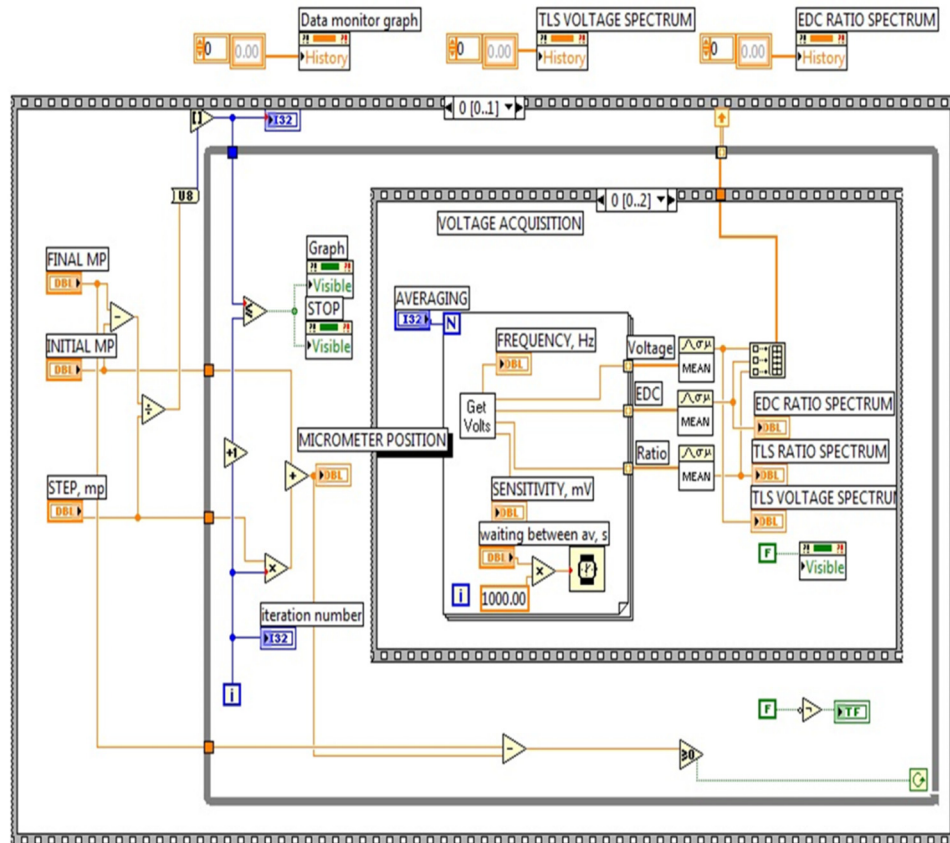


Figure A.12 Main VI

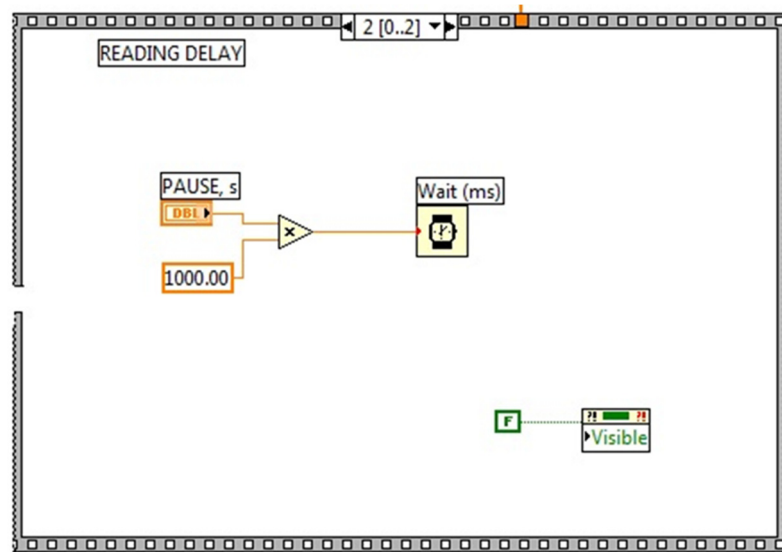


Figure A.13 Pause time VI

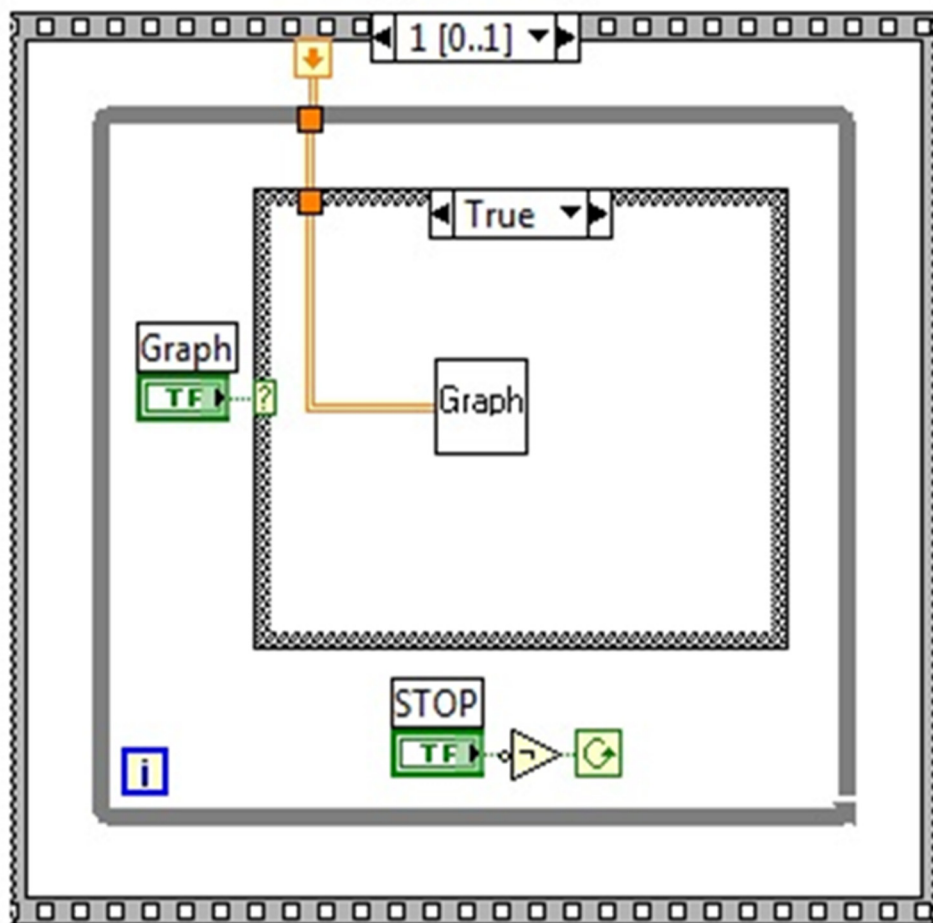


Figure A.14 global display VI

APPENDIX B

B.1 List of Variables

c = Speed of light

f = Modulation frequency

σ = Frequency at peak absorption

α = Absorption cross section

τ = Ring down time

R = Reflectivity of the mirror

L = length of the cavity

Θ = Phase shift angle

B = Rotational constant

I_{abs} = Intensity of absorption

Q_r = Rotational partition function

C_{abs} = Constant depending on the change of the dipole moment

k = Boltzmann constant

J = Total rotational quantum number

N = Rotational angular momentum

S = Spin angular momentum

H = Spin- spin coupling

λ = Spin – spin coupling

γ = Spin-rotation constant

T_e = Electronic energy

ω_e = Harmonic frequency

x_e, y_e, z_e = Anharmonicities

v = Vibrational quantum number

ν = Frequency

$\alpha_e, \gamma_e, \beta_e$ = Vibrational constants

D_v .= Centrifugal distortion constant

α_2 = Absorption cross section for vibrational transition

β_2 = Absorption cross section for electronic transition

C_p = Specific heat capacity

t_c = Thermal characteristic time constant

ρ = Density

w_0 = Radius of the pump laser

n = Refractive index

$\Delta H_{2,m}$ = Enthalpy of melting

T_{2m} = Melting temperature

Γ = Activity coefficient

ϕ = Fugacity

k_{12} = Interaction parameter

ϵ/K_B = Energy of interaction

m = Segment

$\sigma (\text{\AA})$ = Segment diameter

\AA = Armstrong

δ_1 = Solubility parameter for solvent

δ_2 = Solubility parameter for solute

δ_R = Reduced solubility parameter

l_{12} = Interaction constant characteristic of a solvent- solute pair

ΔH^v = Molar enthalpy of vaporization

T_c = Critical temperature

P_c = Critical pressure

V_c = Critical volume

T_R = Reduced temperature

V_R = Reduced volume

V_1 = Molar volume of solvent

V_2 = Molar volume of solute

REFERENCES

1. Berden, G.; Peeters, R.; Meijer, G., Cavity ring-down spectroscopy: Experimental schemes and applications. *International Reviews in Physical Chemistry*. **2000**, *19* (4), 565-607.
2. Herbelin, J. M.; McKay, J. A.; Kwok, M. A.; Ueunten, R. H.; Urevig, D. S.; Spencer, D. J.; Benard, D. J., Sensitive measurement of photon lifetime and true reflectances in an optical cavity by a phase-shift method. *Appl. Opt.* **1980**, *19* (1), 144-147.
3. Anderson, D. Z.; Frisch, J. C.; Masser, C. S., Mirror reflectometer based on optical cavity decay time. *Appl. Opt.* **1984**, *23* (8), 1238-1245.
4. Hallock, A. J.; Berman, E. S. F.; Zare, R. N., Use of Broadband, Continuous-Wave Diode Lasers in Cavity Ring-Down Spectroscopy for Liquid Samples. *Appl. Spectrosc.* **2003**, *57* (5), 571-573.
5. Hallock, A. J.; Berman, E. S. F.; Zare, R. N., Direct Monitoring of Absorption in Solution by Cavity Ring-Down Spectroscopy. *Analytical Chemistry*. **2002**, *74* (7), 1741-1743.
6. Hallock, A. J.; Berman, E. S. F.; Zare, R. N., Direct Monitoring of Absorption in Solution by Cavity Ring-Down Spectroscopy. *Analytical Chemistry*. **2007**, *79* (6), 2596-2596.
7. Kiwanuka, S.-S.; Laurila, T.; Kaminski, C. F., Sensitive Method for the Kinetic Measurement of Trace Species in Liquids Using Cavity Enhanced Absorption Spectroscopy with Broad Bandwidth Supercontinuum Radiation. *Analytical Chemistry*. **2010**, *82* (17), 7498-7501.
8. Xu, S.; Sha, G.; Xie, J., Cavity ring-down spectroscopy in the liquid phase. *Review of Scientific Instruments*. **2002**, *73* (2), 255-258.
9. Engeln, R.; Letourneur, K. G. Y.; Boogaarts, M. G. H.; van de Sanden, M. C. M.; Schram, D. C., Detection of CH in an expanding argon/acetylene plasma using cavity ring down absorption spectroscopy. *Chemical Physics Letters*. **1999**, *310* (5–6), 405-410.
10. Benedikt, J.; Woen, R. V.; van Mensfoort, S. L. M.; Perina, V.; Hong, J.; van de Sanden, M. C. M., Plasma chemistry during the deposition of a-C:H films and its influence on film properties. *Diamond and Related Materials*. **2003**, *12* (2), 90-97.

11. Van de Sanden, M. C. M.; van Hest, M. F. A. M.; de Graaf, A.; Smets, A. H. M.; Letourneur, K. G. Y.; Boogaarts, M. G. H.; Schram, D. C., Plasma chemistry of an expanding Ar/C₂H₂ plasma used for fast deposition of a-C:H. *Diamond and Related Materials.* **1999**, *8* (2–5), 677-681.
12. John, P.; Rabeau, J. R.; Wilson, J. I. B., The cavity ring-down spectroscopy of C₂ in a microwave plasma. *Diamond and Related Materials.* **2002**, *11* (3–6), 608-611.
13. Hoefnagels, J. P. M.; Stevens, A. A. E.; Boogaarts, M. G. H.; Kessels, W. M. M.; van de Sanden, M. C. M., Time-resolved cavity ring-down spectroscopic study of the gas phase and surface loss rates of Si and SiH₃ plasma radicals. *Chemical Physics Letters.* **2002**, *360* (1–2), 189-193.
14. Hoefnagels, J. P. M.; Stevens, A. A. E.; Boogaarts, M. G. H.; Kessels, W. M. M.; van de Sanden, M. C. M., Time-resolved cavity ring-down spectroscopic study of the gas phase and surface loss rates of Si and SiH₃ plasma radicals. *Chemical Physics Letters.* **2002**, *360* (1–2), 189-193.
15. Hippler, M.; Quack, M., Cw cavity ring-down infrared absorption spectroscopy in pulsed supersonic jets: nitrous oxide and methane. *Chemical Physics Letters.* **1999**, *314* (3–4), 273-281.
16. Scherer, J. J.; Paul, J. B.; O'Keefe, A.; Saykally, R. J., Cavity Ringdown Laser Absorption Spectroscopy: History, Development, and Application to Pulsed Molecular Beams. *Chemical Reviews.* **1997**, *97* (1), 25-52.
17. Ito, F.; Nakanaga, T., Jet-cooled infrared spectra of the formic acid dimer by cavity ring-down spectroscopy: observation of the O-H stretching region. *Chemical Physics.* **2002**, *277* (2), 163-169.
18. Ito, F., Jet-cooled infrared spectra of the formic acid dimer by cavity ring-down spectroscopy: Observation of the C–O stretching region and vibrational analysis of the Fermi-triad system. *Chemical Physics Letters.* **2007**, *447* (4–6), 202-207.
19. Czyżewski, A.; Ernst, K.; Franssen, G.; Karasinski, G.; Kmiecik, M.; Lange, H.; Skubiszak, W.; Stacewicz, T., Investigation of kinetics of CH-radicals decay by cavity ring-down spectroscopy. *Chemical Physics Letters.* **2002**, *357* (5–6), 477-482.
20. Atkinson, D. B.; Spillman, J. L., Alkyl Peroxy Radical Kinetics Measured Using Near-infrared CW–Cavity Ring-down Spectroscopy. *The Journal of Physical Chemistry. A.* **2002**, *106* (38), 8891-8902.

21. Tonokura, K.; Koshi, M., Absorption Spectrum and Cross Sections of the Allyl Radical Measured Using Cavity Ring-Down Spectroscopy: The $\tilde{\text{A}} \leftarrow \tilde{\text{X}}$ Band. *The Journal of Physical Chemistry. A.* **2000**, *104* (37), 8456-8461.
22. Tonokura, K.; Ogura, T.; Koshi, M., Near-UV Absorption Spectrum of the Phenoxy Radical and Kinetics of Its Reaction with CH_3 . *The Journal of Physical Chemistry A.* **2004**, *108* (39), 7801-7805.
23. Tonokura, K.; Norikane, Y.; Koshi, M.; Nakano, Y.; Nakamichi, S.; Goto, M.; Hashimoto, S.; Kawasaki, M.; Sulbaek Andersen, M. P.; Hurley, M. D.; Wallington, T. J., Cavity Ring-down Study of the Visible Absorption Spectrum of the Phenyl Radical and Kinetics of Its Reactions with Cl, Br, Cl_2 , and O_2 . *The Journal of Physical Chemistry. A.* **2002**, *106* (24), 5908-5917.
24. Sakamoto, Y.; Yamano, D.; Nakayama, T.; Hashimoto, S.; Kawasaki, M.; Wallington, T. J.; Miyano, S.; Tonokura, K.; Takahashi, K., Atmospheric Chemistry of BrO Radicals: Kinetics of the Reaction with $\text{C}_2\text{H}_5\text{O}_2$ Radicals at 233–333 K. *The Journal of Physical Chemistry. A.* **2009**, *113* (38), 10231-10237.
25. Ito, F., Methyl iodide clusters observed in gas phase by infrared cavity ring-down spectroscopy: The CH_3 bending mode at $8\mu\text{m}$. *The Journal of Chemical Physics.* **2006**, *124* (5), 054309.
26. Atkinson, D. B.; Hudgens, J. W., Chlorination Chemistry. 2. Rate Coefficients, Reaction Mechanism, and Spectrum of the Chlorine Adduct of Allene. *The Journal of Physical Chemistry. A.* **2000**, *104* (4), 811-818.
27. Douin, S.; Gronowski, M.; Lamarre, N.; Phung, V.-T.; Boyé-Pérone, S.; Crépin, C.; Kołos, R., Cavity Ring Down Spectroscopy Measurements for High-Overtone Vibrational Bands of HC_3N . *The Journal of Physical Chemistry. A.* **2015**, *119* (36), 9494-9505.
28. Lu, Y.; Liu, A. W.; Pan, H.; Li, X. F.; Perevalov, V. I.; Tashkun, S. A.; Hu, S. M., High sensitivity cavity ring down spectroscopy of $^{13}\text{C}^{16}\text{O}_2$ overtone bands near 806 nm. *Journal of Quantitative Spectroscopy and Radiative Transfer.* **2012**, *113* (17), 2197-2204.
29. Song, K. F.; Lu, Y.; Tan, Y.; Gao, B.; Liu, A. W.; Hu, S. M., High sensitivity cavity ring down spectroscopy of CO_2 overtone bands near 790 nm. *Journal of Quantitative Spectroscopy and Radiative Transfer.* **2011**, *112* (5), 761-768.
30. Brown, S. S.; Stark, H.; Ravishankara, A. R., Cavity ring-down spectroscopy for atmospheric trace gas detection: application to the nitrate radical (NO_3). *Applied Physics. B.* **2002**, *75* (2), 173-182.

31. Schuster, G.; Labazan, I.; Crowley, J. N., A cavity ring down/cavity enhanced absorption device for measurement of ambient NO₃ and N₂O₅. *Atmos. Meas. Tech.* **2009**, 2 (1), 1-13.
32. Masurenka, M. I.; Fawcett, B. L.; Elks, J. M. F.; Shallcross, D. E.; Orr-Ewing, A. J., 410 nm diode laser cavity ring-down spectroscopy for trace detection of NO₂. *Chemical Physics Letters*. **2003**, 367 (1–2), 1-9.
33. Nakaema, W. M.; Hao, Z.-Q.; Rohwetter, P.; Wöste, L.; Stelmaszczyk, K., PCF-Based Cavity Enhanced Spectroscopic Sensors for Simultaneous Multicomponent Trace Gas Analysis. *Sensors*. **2011**, 11 (2), 1620.
34. McHale, L. E.; Hecobian, A.; Yalin, A. P., Open-path cavity ring-down spectroscopy for trace gas measurements in ambient air. *Optics express*. **2016**, 24 (5), 5523-5535.
35. Maher, D. T.; Santos, I. R.; Leuven, J. R. F. W.; Oakes, J. M.; Erler, D. V.; Carvalho, M. C.; Eyre, B. D., Novel Use of Cavity Ring-down Spectroscopy to Investigate Aquatic Carbon Cycling from Microbial to Ecosystem Scales. *Environmental Science & Technology*. **2013**, 47 (22), 12938-12945.
36. Liu, Y.; Zhang, J., Measurement of aerosol optical extinction using diode laser cavity ringdown spectroscopy. *Chinese Science Bulletin*. **2013**, 58 (20), 2440-2446.
37. Li, L.; Chen, J.; Chen, H.; Yang, X.; Tang, Y.; Zhang, R., Monitoring optical properties of aerosols with cavity ring-down spectroscopy. *Journal of Aerosol Science*. **2011**, 42 (4), 277-284.
38. Engeln, R.; von Helden, G.; Berden, G.; Meijer, G., Phase shift cavity ring down absorption spectroscopy. *Chemical Physics Letters*. **1996**, 262 (1), 105-109.
39. Nyaupane, P. R.; Perez-Delgado, Y.; Camejo, D.; Wright, L. M.; Manzanares, C. E., Cavity Ring Down Absorption of O₂ in Air as a Temperature Sensor for an Open and a Cryogenic Optical Cavity. *Appl. Spectrosc.* **2016**.
40. Lewis, E. K.; Moehnke, C. J.; Navea, J. G.; Manzanares, C. E., Low temperature cell for cavity ring down absorption studies. *Review of Scientific Instruments*. **2006**, 77 (7), 073107.
41. Zalicki, P.; Zare, R. N., Cavity ring-down spectroscopy for quantitative absorption measurements. *The Journal of Chemical Physics*. **1995**, 102 (7), 2708-2717.
42. Busch, K. W.; Busch, M. A. In Cavity-Ringdown Spectroscopy: *An Ultratrace-Absorption Measurement Technique*; ACS Symposium Series. **1999**, 269.

43. Cavity-Ringdown Spectroscopy, Copyright, Advisory Board, Foreword. In *Cavity-Ringdown Spectroscopy*, American Chemical Society. **1999**; Vol. 720, i-vii.
44. Lehmann, K. K.; Romanini, D., The superposition principle and cavity ring-down spectroscopy. *The Journal of Chemical Physics*. **1996**, *105* (23), 10263-10277.
45. Haslam, R. T.; Chappell, E. L., The Measurement of the Temperature of a Flowing Gas. *Industrial & Engineering Chemistry*. **1925**, *17* (4), 402-408.
46. <http://web.mst.edu/~cottrell/ME240/Resources/Temperature/Temperature.pdf>
47. Daniels, G. E., Measurement of Gas Temperature and the Radiation Compensating Thermocouple. *Journal of Applied Meteorology*. **1968**, *7* (6), 1026-1035.
48. Dyne, P. J., Optical Methods for the Determination of Combustion Temperatures. *Journal of the American Rocket Society*. **1953**, *23* (3), 165-169.
49. Hieta, T.; Merimaa, M., Spectroscopic Measurement of Air Temperature. *International Journal of Thermophysics*. **2010**, *31* (8-9), 1710-1718.
50. Zhou, X.; Liu, X.; Jeffries, J. B.; Hanson, R. K., Development of a sensor for temperature and water concentration in combustion gases using a single tunable diode laser. *Measurement Science and Technology*. **2003**, *14* (8), 1459.
51. Wampler, F. B.; Gentry, R. A., Determination of gas temperature and density by measuring ultraviolet gas absorption at two wavelengths. *Journal of Applied Physics*. **1981**, *52* (3), 1583-1583.
52. Rice, W. W.; Oldenborg, R. C.; Wampler, F. B.; Tiee, J. J., Gas temperature and density of UF₆ determined by two-wavelength UV absorption. *Appl. Opt.* **1981**, *20* (15), 2625-2629.
53. Santiago, I.; Muñoz, J.; Calzada, M. D., Self-absorption Effects In Experimental Methods Used To Determine Electron Density And Gas Temperature In An Argon Microwave Plasma (SWP) Generated At Atmospheric Pressure. *AIP Conference Proceedings*. **2008**, *1058* (1), 21-23.
54. Fateev, A.; Clausen, S., In situ Gas Temperature Measurements by UV-Absorption Spectroscopy. *International Journal of Thermophysics*. **2009**, *30* (1), 265-275.

55. Jeffries, J. B.; Schulz, C.; Mattison, D. W.; Oehlschlaeger, M. A.; Bessler, W. G.; Lee, T.; Davidson, D. F.; Hanson, R. K., UV absorption of CO₂ for temperature diagnostics of hydrocarbon combustion applications. *Proceedings of the Combustion Institute.* **2005**, *30* (1), 1591-1599.
56. Amrein, A.; Quack, M.; Schmitt, U., High-resolution interferometric Fourier transform infrared absorption spectroscopy in supersonic free jet expansions: carbon monoxide, nitric oxide, methane, ethyne, propyne, and trifluoromethane. *The Journal of Physical Chemistry.* **1988**, *92* (19), 5455-5466.
57. Shahnam, M; Woodruff, S.D; Celik, I; Logan, R.G. Gas Stream Measurements via Fourier Transform Infrared Spectroscopy. Mechanical and Aerospace Engineering Department West Virginia University, Morgantown.
58. Fleckl, T.; Jäger, H.; Obernberger, I., Experimental verification of gas spectra calculated for high temperatures using the HITRAN/HITEMP database. *Journal of Physics D: Applied Physics.* **2002**, *35* (23), 3138.
59. Rensberger, K. J.; Jeffries, J. B.; Copeland, R. A.; Kohse-Höinghaus, K.; Wise, M. L.; Crosley, D. R., Laser-induced fluorescence determination of temperatures in low pressure flames. *Appl. Opt.* **1989**, *28* (17), 3556-3566.
60. Lee, T.; Bessler, W. G.; Kronemayer, H.; Schulz, C.; Jeffries, J. B., Quantitative temperature measurements in high-pressure flames with multiline NO-LIF thermometry. *Appl. Opt.* **2005**, *44* (31), 6718-6728.
61. Cheskis, S.; Kachanov, A.; Chenevier, M.; Stoeckel, F., Temperature measurements in flames using water molecule overtone spectra detected by intracavity laser absorption spectroscopy. *Applied Physics. B.* **1997**, *64* (6), 713-716.
62. Cheskis, S.; Derzy, I.; Lozovsky, V. A.; Kachanov, A.; Romanini, D., Cavity ring-down spectroscopy of OH radicals in low pressure flame. *Applied Physics. B.* **1998**, *66* (3), 377-381.
63. Ren, W.; Farooq, A.; Davidson, D. F.; Hanson, R. K., CO concentration and temperature sensor for combustion gases using quantum-cascade laser absorption near 4.7 μm. *Applied Physics. B.* **2012**, *107*.
64. Farooq, A.; Jeffries, J. B.; Hanson, R., CO₂ concentration and temperature sensor for combustion gases using diode-laser absorption near 2.7 μm. *Applied Physics. B.* **2008**, *90* (3-4), 619-62.

65. Liu, J. T.; Rieker, G. B.; Jeffries, J. B.; Gruber, M. R.; Carter, C. D.; Mathur, T.; Hanson, R. K., Near-infrared diode laser absorption diagnostic for temperature and water vapor in a scramjet combustor. *Appl. Opt.* **2005**, *44* (31), 6701-6711.
66. Grossmann, B. E.; Cahen, C.; Lesne, J. L.; Benard, J.; Leboudec, G., Intensities and atmospheric broadening coefficients measured for O₂ and H₂O absorption lines selected for DIAL monitoring of both temperature and humidity. *Appl. Opt.* **1986**, *25* (23), 4261-4267.
67. Zyryanov, S. M.; Lopaev, D. V., Measurements of the gas temperature in an oxygen plasma by spectroscopy of the O₂ ($b^1\Sigma_g^+$) → O₂ ($X^3\Sigma_g^-$) transition. *Plasma Phys. Rep.* **2007**, *33* (6), 510-520.
68. Masoud, N.; Martus, K.; Figus, M.; Becker, K., Rotational and Vibrational Temperature Measurements in a High-Pressure Cylindrical Dielectric Barrier Discharge (C-DBD). *Contributions to Plasma Physics*. **2005**, *45* (1), 32-39.
69. Berg, P. A.; Hill, D. A.; Noble, A. R.; Smith, G. P.; Jeffries, J. B.; Crosley, D. R., Absolute CH concentration measurements in low-pressure methane flames: comparisons with model results. *Combustion and Flame*. **2000**, *121* (1–2), 223-235.
70. Rahinov, I.; Ditzian, N.; Goldman, A.; Cheskis, S., NH₂ radical formation by ammonia pyrolysis in a temperature range of 800–1000 K. *Applied Physics. B.* **2003**, *77* (5), 541-546.
71. Werblinski, T.; Mittmann, F.; Altenhoff, M.; Seeger, T.; Zigan, L.; Will, S., Temperature and water mole fraction measurements by time-domain-based supercontinuum absorption spectroscopy in a flame. *Applied Physics. B.* **2015**, *118* (1), 153-158.
72. Fomin, A.; Zavlev, T.; Rahinov, I.; Cheskis, S., A fiber laser intracavity absorption spectroscopy (FLICAS) sensor for simultaneous measurement of CO and CO₂ concentrations and temperature. *Sensors and Actuators B: Chemical*. **2015**, *210* (0), 431-438.
73. Wright, L.M.; Han, J. C. Heat Transfer enhancement for Turbine Blade internal Cooling. ASME Paper No. HT2013-17813, ASME Summer Heat Transfer Conference, Minneapolis, MN, July **2013**.
74. Han, J. C.; Dutta, S.; Ekkad, S. Gas Turbine heat Transfer and Cooling Technology. New York, NY: Taylor and Francis, **2000**.
75. Wright, L. M.; McClain, S. T.; Clemenson, M. D., Effect of Freestream Turbulence Intensity on Film Cooling Jet Structure and Surface Effectiveness Using PIV and PSP. *Journal of Turbomachinery*. **2011**, *133* (4), 041023-041023.

76. Wright, L. M.; McClain, S. T.; Clemenson, M. D., Effect of Density Ratio on Flat Plate Film Cooling With Shaped Holes Using PSP. *Journal of Turbomachinery*. **2011**, *133* (4), 041011-041011.
77. Wright, L. M.; McClain, S. T.; Brown, C. P.; Harmon, W. V. Assessment of a Double Hole, Anti-Vortex Film Cooling Geometry Using S-PIV and PSP. ASME Paper No GT2013-94614, ASME (IGTI) Turbo Expo, San Antonio, TX, June **2013**.
78. Brown, C. P.; Wright, L. M.; McClain, S. T. Comparison of Staggered and In-Line V-shaped Dimple Arrays using S-PIV. ASME Paper No. GT2015-43499, ASME (IGTI) Turbo Expo, Montreal, Canada, June **2015**.
79. Herzberg, G. In Spectra of Diatomic Molecules; Van Nostrand, Ed.; Princeton: New York, **1950**.
80. Jockusch, S.; Turro, N. J.; Thompson, E. K.; Gouterman, M.; Callis, J. B.; Khalil, G. E. The Royal Society of Chemistry and Owner Societies, Photochem. *Photobiol. Sci.* **2008**, *7*, 235-239.
81. Gamache, R. R.; Goldman, A.; Rothman, L. S. *J. Quant. Spectrosc. Radiat. Transfer*. **1998**, *59*, 495-509.
82. Perez- Prez-Delgado, Y.; Manzanares,C. E. *J. Phys. Chem. A*. **2010**, *114*, 7918.
83. Delgado,Y.; Manzanares,C.E. *Applied Physics. B*. **2011**, *106*,971-978.
84. Prez-Delgado, Y.; Lewis, E. K.; Moehnke, C. J.; Salazar, M. C.; Hernazed, A. J.; Manzanarea, C. E. *Mol. Phys.* **2009**, *107*, 1367.
85. Miller, J. H.; Boese, R. W.; Giver, L. P. Intensity Measurements and Rotational Intensity Distribution for the Oxygen A-Band. *J. Quant. Spectrosc. Radiat. Transfer*. **1969**, *9*, 1507-1517.
86. Adams, S. F.; Wu, Y.; Zhang, Z., Oxygen Rotational Temperature Determination Using Empirical Analyses of $C^3\Pi$ ($v' = 2$) $\leftarrow X^3\Sigma$ ($v'' = 0$) Transitions. *Appl. Spectrosc.* **2015**, *69* (9), 1036-1041.
87. Liu, X.; Jeffries, J. B.; Hanson, R. K.; Hinckley, K. M.; Woodmansee, M. A., Development of a tunable diode laser sensor for measurements of gas turbine exhaust temperature. *Applied Physics. B*. **2006**, *82* (3), 469-478.
88. PGOPHER, a Program for Simulating Rotational Structure, C. M. Western, University of Bristol, <http://pgopher.chm.bris.ac.uk>.

89. Macko, P.; Veis, P., Time resolved O₂ (b¹Σ_g⁺) rotational temperature measurements in a low-pressure oxygen pulsed discharge. Simple and quick method for temperature determination. *Journal of Physics. D: Applied Physics.* **1999**, 32 (3), 246.
90. Anderson, C. M.; Samuelson, R. E., Titan's aerosol and stratospheric ice opacities between 18 and 500 μm: Vertical and spectral characteristics from Cassini CIRS. *Icarus.* **2011**, 212 (2), 762-778.
91. Atkinson, D. B., Solving chemical problems of environmental importance using cavity ring-down spectroscopy. *Analyst.* **2003**, 128 (2), 117-125.
92. McKellar, A. R. W., Long-path equilibrium IR spectra of weakly bound complexes at low temperatures. *Faraday Discussions.* **1994**, 97 (0), 69-80.
93. Long, M.; Swofford, R.; Albrecht, A., Thermal lens technique: a new method of absorption spectroscopy. *Science.* **1976**, 191 (4223), 183-185.
94. Kumar, P.; Dinda, S.; Goswami, D., Effect of molecular structural isomers in thermal lens spectroscopy. *Chemical Physics Letters.* **2014**, 601, 163-167.
95. Dovichi, N. J.; Bialkowski, S. E., Thermo-Optical Spectrophotometries in Analytical Chemistry. *C R C Critical Reviews in Analytical Chemistry.* **1987**, 17 (4), 357-423.
96. Harris, J. M. Thermal Lens Effect. In *Analytical Applications of Laser*, Piepmeyer E. H. *Chemical Analysis 87*; Wiley and Sons: New York (1986).
97. Bialkowski, S. E. *Photothermal Spectroscopy Methods for Chemical Analysis* (Wiley, New York, 1996), 390.
98. Fang, H. L.; Swofford, R. L. in *Ultrasensitive Laser Spectroscopy*, ed. By D.S. Klier (Academic Press, New York, 1983), 175.
99. Gordon, J. P.; Leite, R. C. C.; Moore, R. S.; Porto, S. P. S.; Whinnery, J. R., Long-Transient Effects in Lasers with Inserted Liquid Samples. *Journal of Applied Physics.* **1965**, 36 (1), 3-8.
100. Grabiner, F. R.; Siebert, D. R.; Flynn, G. W., Laser induced time-dependent thermal lensing studies of vibrational relaxation: translational cooling in CH₃F. *Chemical Physics Letters.* **1972**, 17 (2), 189-194.
101. Hu, C.; Whinnery, J. R., New Thermo-optical Measurement Method and a Comparison with Other Methods. *Appl. Opt.* **1973**, 12 (1), 72-79.

102. Whinnery, J. R., Laser measurement of optical absorption in liquids. *Accounts of Chemical Research*. **1974**, 7 (7), 225-231.
103. Bialkowski, S. E., Pulsed laser thermal lens spectrophotometry of liquid samples using an optical fiber beam guide with interference orthogonal signal processing. *Analytical Chemistry*. **1986**, 58 (8), 1706-1710.
104. Long, G. R.; Bialkowski, S. E., Pulsed infrared laser thermal lens spectrophotometric determination of trace-level gas-phase analytes: quantitation of parts per billion dichlorodifluoromethane. *Analytical Chemistry*. **1984**, 56 (14), 2806-2811.
105. Sabaeian, M.; Rezaei, H.; Ghalambor-Dezfouli, A., Time-resolved thermal lens spectroscopy with a single-pulsed laser excitation beam: an analytical model for dual-beam mode-mismatched experiments. *Appl. Opt.* **2017**, 56 (4), 999-1005.
106. Swofford, R. L.; Morrell, J. A., Analysis of the repetitively pulsed dual-beam thermo-optical absorption spectrometer. *Journal of Applied Physics*. **1978**, 49.
107. Lui, M; Korte, D; Franko, M. *Journal of applied Physics*. **2012**, 111, 033109.
108. Mawatari, K.; Kubota, S.; Kitamori, T., Circular dichroism thermal lens microscope in the UV wavelength region (UV-CD-TLM) for chiral analysis on a microchip. *Analytical and Bioanalytical Chemistry*. **2008**, 391 (7), 2521-2526.
109. Liu, M.; Franko, M., Thermal Lens Spectrometry: Still a Technique on the Horizon? *International Journal of Thermophysics*. **2016**, 37 (7), 67.
110. Twarowski, A. J.; Kliger, D. S., Multiphoton absorption spectra using thermal blooming. *Chemical Physics*. **1977**, 20 (2), 259-264.
111. Twarowski, A. J.; Kliger, D. S., Multiphoton absorption spectra using thermal blooming. *Chemical Physics*. **1977**, 20 (2), 253-258.
112. Dovichi, N. J.; Nolan, T. G.; Weimer, W. A., Theory for laser-induced photothermal refraction. *Analytical Chemistry*. **1984**, 56 (9), 1700-1704.
113. Nolan, T. G.; Weimer, W. A.; Dovichi, N. J., Laser-induced photothermal refraction for small volume absorbance determination. *Analytical Chemistry*. **1984**, 56 (9), 1704-1707.
114. Vyas, R.; Monson, B.; Nie, Y. X.; Gupta, R., Continuous wave photothermal deflection spectroscopy in a flowing medium. *Appl. Opt.* **1988**, 27 (18), 3914-3920.

115. Vyas, R.; Gupta, R., Photothermal lensing spectroscopy in a flowing medium: theory. *Appl. Opt.* **1988**, 27 (22), 4701-4711.
116. Niemann et.al, *Nature*. **2005**, 438, 779.
117. Raulin, F., Planetary science: Organic lakes on Titan. *Nature*. **2008**, 454 (7204), 587-589.
118. Stofan, E. R.; Elachi, C.; Lunine, J. I.; Lorenz, R. D.; Stiles, B.; Mitchell, K. L.; Ostro, S.; Soderblom, L.; Wood, C.; Zebker, H.; Wall, S.; Janssen, M.; Kirk, R.; Lopes, R.; Paganelli, F.; Radebaugh, J.; Wye, L.; Anderson, Y.; Allison, M.; Boehmer, R.; Callahan, P.; Encrenaz, P.; Flamini, E.; Francescetti, G.; Gim, Y.; Hamilton, G.; Hensley, S.; Johnson, W. T. K.; Kelleher, K.; Muhleman, D.; Paillou, P.; Picardi, G.; Posa, F.; Roth, L.; Seu, R.; Shaffer, S.; Vetrella, S.; West, R., The lakes of Titan. *Nature*. **2007**, 445 (7123), 61-64.
119. Tam, A. C.; Patel, C. K. N.; Kerl, R. J., Measurement of small absorptions in liquids. *Opt. Lett.* **1979**, 4 (3), 81-83.
120. Tam, A. C.; Patel, C. K. N., Ultimate corrosion-resistant optoacoustic cell for spectroscopy of liquids. *Opt. Lett.* **1980**, 5 (1), 27-29.
121. Franko, M.; Tran, C. D., Thermal lens effect in electrolyte and surfactant media. *The Journal of Physical Chemistry*. **1991**, 95 (17), 6688-6696.
122. Lorenz, H. A. *Wied. Ann.* **1880**, 9, 641.
123. Lorenz, H. A. *Wied. Ann.* **1880**, 11, 70.
124. Heller, W., Remarks on Refractive Index Mixture Rules. *The Journal of Physical Chemistry*. **1965**, 69 (4), 1123-1129.
125. Valkai, S.; Liszsi, J.; Szalai, I., Temperature dependence of the refractive index for three chloromethane liquids at 514.5 nm and 632.8 nm wavelengths. *The Journal of Chemical Thermodynamics*. **1998**, 30 (7), 825-832.
126. Waxler, R. M.; Weir, C. E. *J. Res. Natl. Bur. Stand. A Phys. Chem.* **1963**, 67A, 163.
127. de Cominges, B. E.; Piñeiro, M. M.; Mosteiro, E.; Mascato, E.; Mato, M. M.; Iglesias, T. P.; Legido, J. L., Temperature dependence of thermophysical properties of octane+1-butanol system. *Journal of Thermal Analysis and Calorimetry*. **2002**, 70 (1), 217-227.
128. Coker, A. K., Ludwig's Applied Process Design for Chemical and Petrochemical Plants, Volume 1 (4th Edition). Elsevier.

129. Assael, M. J.; Ramires, M. L. V.; Nieto de Castro, C. A.; Wakeham, W. A., Benzene: A Further Liquid Thermal Conductivity Standard. *Journal of Physical and Chemical Reference Data*. **1990**, *19* (1), 113-117.
130. Atkins, P.; DePaula, J. in Physical chemistry, 9th edn. Vol. 1 (Freeman, New York 2010), 926.
131. Diez-y-Riega, H.; Camejo, D.; Manzanares, C. E., Thermal lens detection of one and two-color laser excitation of benzene in cryogenic liquid solutions. *Journal of Raman Spectroscopy*. **2015**, *46* (8), 716-721.
132. Patel, C. K. N.; Tam, A. C., Pulsed optoacoustic spectroscopy of condensed matter. *Reviews of Modern Physics*. **1981**, *53* (3), 517-550.
133. Peralta, S. B.; Mandelis, A., Optical saturation in the photothermal spectroscopy of fluorescent materials. *Appl. Phys. A*. **1990**, *50* (4), 353-356.
134. Li, B.; Gupta, R., Optical saturation in continuous-wave photothermal deflection spectroscopy: quantitative investigation of fundamental and harmonic components. *Appl. Opt.* **2001**, *40* (9), 1563-1569.
135. Ramis-Ramos, G.; Baeza Baeza, J. J.; Simó Alfonso, E. F., A model for optical saturation thermal lens spectrometry. *Analytica Chimica Acta*. **1994**, *296* (1), 107-113.
136. De Stefani, V.; Baba-Ahmed, A.; Richon, D., A review of experimental methods for solid solubility determination in cryogenic systems. *Cryogenics*. **2004**, *44* (9), 631-641.
137. Rest, A. J.; Scurlock, R. G.; Wu, M. F., The solubilities of nitrous oxide, carbon dioxide, Aliphatic ethers and alcohols, and water in cryogenic liquids. *The Chemical Engineering Journal*. **1990**, *43* (1), 25-31.
138. Gao, T.; Shen, T.; Lin, W.; Gu, A.; Ju, Y., Experimental Determination of CO₂ Solubility in Liquid CH₄/N₂ Mixtures at Cryogenic Temperatures. *Industrial & Engineering Chemistry Research*. **2012**, *51* (27), 9403-9408.
139. Tokano, T., Thermal structure of putative hydrocarbon lakes on Titan. *Advances in Space Research*. **2005**, *36* (2), 286-294.
140. Cordier, D.; Mousis, O.; Lunine, J.I.; Lebonnois, S.; Rannous, P.; Lavvas, P.; Lobo, L.Q.; Ferreira, A.G.M. *Planetary and Space Science*. **2012**, *61*, 99-107.
141. Cordier, D.; Barnes, J. W.; Ferreira, A. G. *International Journal of Solar System Studies*. **2013**.

142. McKay, C. P., Elemental composition, solubility, and optical properties of Titan's organic haze. *Planetary and Space Science*. **1996**, *44* (8), 741-747.
143. Brown, R. H.; Soderblom, L. A.; Soderblom, J. M.; Clark, R. N.; Jaumann, R.; Barnes, J. W.; Sotin, C.; Buratti, B.; Baines, K. H.; Nicholson, P. D., The identification of liquid ethane in Titan's Ontario Lacus. *Nature*. **2008**, *454* (7204), 607-610.
144. Turtle, E. P.; Perry, J. E.; Hayes, A. G.; Lorenz, R. D.; Barnes, J. W.; McEwen, A. S.; West, R. A.; Del Genio, A. D.; Barbara, J. M.; Lunine, J. I.; Schaller, E. L.; Ray, T. L.; Lopes, R. M. C.; Stofan, E. R., Rapid and Extensive Surface Changes Near Titan's Equator: Evidence of April Showers. *Science*. **2011**, *331* (6023), 1414-1417.
145. Turtle, E. P.; Del Genio, A. D.; Barbara, J. M.; Perry, J. E.; Schaller, E. L.; McEwen, A. S.; West, R. A.; Ray, T. L., Seasonal changes in Titan's meteorology. *Geophysical Research Letters*. **2011**, *38* (3).
146. Cordier, D.; Mousis, O.; Lunine, I. J.; Lavvas, P.; Vuitton, V. An estimate of the chemical composition of titan's lakes. *The Astrophysical Journal Letters*. **2009**, *707*(2).
147. Tan, S. P.; Kargel, J. S.; Marion, G. M., Titan's atmosphere and surface liquid: New calculation using Statistical Associating Fluid Theory. *Icarus*. **2013**, *222* (1), 53-72.
148. Kurdziel, M.; Szczepaniec-Cieciak, E.; Watorczyk, M.; Dabrowska, B., Solubility of Solid 2-Methyl-1,3-butadiene (Isoprene) in Liquid Argon and Nitrogen at the Standard Boiling Points of the Solvents. *Journal of Solution Chemistry*. **2004**, *33* (5), 453-464.
149. Preston, G. T.; Funk, E. W.; Prausnitz, J. M. *The Journal of Physical Chemistry*. **1971**, *75*, 2345-2352.
150. Dabrowska, B., The solubility of selected halogen hydrocarbons in liquid nitrogen at 77.4 K. *Cryogenics*. **1984**, *24* (5), 276-277.
151. Szczepaniec-Cieciak, E.; Krzeczkowska, M., Solubility of 1-Pentene Ice in Liquid Nitrogen and Argon at the Standard Boiling Points of the Solvents. *Journal of Solution Chemistry*. **1998**, *27* (6), 485-494.
152. Szczepaniec-Cieciak, E.; Nagraba, K., The solubility of solidified toluene in liquid nitrogen. *Cryogenics*. **1978**, *18* (10), 601-603.

153. Kurdziel, M.; Szczepaniec-Cieciak, E.; Dąbrowska, B.; Nitek, W.; Paliś, K.; Ślusarska, E., Solubility of Solid 2,3-Dimethylbutane and Cyclopentane in Liquid Argon and Nitrogen at the Standard Boiling Points of the Solvents. *Journal of Solution Chemistry*. **2003**, 32 (7), 601-615.
154. Szczepaniec-Cieciak, E. In Solubility of Solids and Liquids in Cryogenic Liquids; Hefter, G. T., Tomkins, R. P. T. Eds.; The experimental Determination of Solubilities. *John Wiley & Sons*. **2003**, 6, 557-593.
155. Cohen-Adad, R.; Cohen-Adad, M. T. In Solubility of Solids in Liquids; Hefter, G. T., Tomkins, R. P. T., Eds.; The Experimental Determination of Solubilities. *John Wiley & Sons*. **2003**, 6, 257-314.
156. Bulanin, M. O.; Zelikina, G. Y. In Clark, R. J. H., Hester, R. E., Eds.; Molecular Cryospectroscopy in Advances in Spectroscopy; *Wiley*. **1995**, 23, 22.
157. Nabiev, S. S.; Klimov, V. D.; Khodjiev, B. S., IR-Cryospectroscopy as a method for trace analysis of molecular impurities in inorganic fluorides. *Journal of Fluorine Chemistry*. **1992**, 58 (2–3), 293.
158. Zelikina, G. Y.; Meister, T. G.; Mamchenko, T. B., Spectroscopic determination of the solubility of several substances in liquefied gases according to electronic absorption bands. *J Appl Spectrosc*. **1980**, 32 (4), 348-352.
159. Bulanin, M. O., Spectroscopy of molecules in liquid noble gases. *Journal of Molecular Structure*. **1995**, 347, 73-82.
160. Peng, Jingping.; Mina-Camilde, Nairmen.; Manzanares I, C. *Vibrational Spectroscopy*. **1995**, 8, 319-330.
161. Peng, Jingping.; Cedeno, L. David.; Manzanares I, C. *Journal of Molecular Structure*. **1998**, 440, 265-288.
162. Ya. M. Kimel'fel'd, "Spectroscopy of Molecules and Molecular Complexes Dissolved in Liquefied Gases: Structure and Reactivity", *Usp. Khim.* **1988**, 57(8) 1273–1296.
163. Manzanares I, C.; Blunt, Victor M.; Peng, Jingping. *J. Phys. Chem.* **1993**, 97, 3994-4003.
164. Van der Veken, B. J., Infrared Spectroscopy in Liquefied Noble Gases. In Low Temperature Molecular Spectroscopy, Fausto, R., Ed. Springer Netherlands: **1996**, 483, 371-420.

165. Lai, E. P.; Jurgensen, A.; Voigtman, E.; Winefordner, J. D., Low-temperature Photoacoustic Spectroscopy of Polynuclear Aromatic Hydrocarbons in Shpol'skii Matrices at 77 K. *Appl. Spectrosc.* **1982**, *36* (5), 589-592.
166. Manzanares I., C.; Mina-Camilde, N.; Brock, A.; Peng, J.; Blunt, V. M., Piezoelectric detection of vibrational overtones at cryogenic temperatures. *Review of Scientific Instruments*. **1995**, *66* (3), 2644-2651.
167. Vinyard, A.; Hansen, K. A.; Byrd, R.; Stuart, D. A.; Hansen, J. E., Design of a Simple Cryogenic System for Ultraviolet-Visible Absorption Spectroscopy with a Back-Reflectance Fiber Optic Probe. *Appl. Spectrosc.* **2014**, *68* (1), 118-123.
168. Kathrin Lang, E.; Knox, K. J.; Signorell, R., Phase behavior of propane and n-pentane aerosol particles under conditions relevant to Titan. *Planetary and Space Science*. **2013**, *75*, 56-68.
169. Cordier, D.; Barnes, J. W.; Ferreira, A. G. "On the chemical Composition of Titan's Dry Lakebed Evaporites". *Lcrus.* **2013**, *226*, 1431-1437.
170. Cordier, D.; Cornet, T.; Barnes, J. W.; Mackenzie, S. M.; Le Bahers, T.; Nna_Mvondo, D.; Rannou, P.; Ferreira, A. G. "Structure of Titan's Evaporites". *Icarus*. **2016**, *270*, 41-56.
171. Poling, B. E.; Prausnitz, J. M.; O'Connell, J. The properties of Gases and Liquids, 5Th ed; New York: McGraw-Hill Education, **2007**.
172. Gross, J.; Sadowski, G. " Perturbed-Chain SAFT: AN Equation of State Based on a Perturbation Theory for Chain Molecules". *IND. Eng. Chem. Res.* **2001**, *40*, 1244-1260.
173. Tihic, A.; Kontogeorgis, G. M.; Von Solms, N.; Michelsen, M. L.; Constantinou, L. "A Predictive Group-Contributin Simplified PC-SAFT Equation of State: Application to Polymer Systems". *Ins. Eng. Chem. Res.* **2008**, *47*, 5092-5101.
174. Preston, G. T.; Prausnitz, J. M., Thermodynamics of Solid Solubility in Cryogenic Solvents. *Industrial & Engineering Chemistry Process Design and Development*. **1970**, *9* (2), 264-271.
175. Yaws, C. L. Thermophysical Properties of Chemicals and Hydrocarbons, 2nd ed; New York: Elsevier, **2014**.
176. Amamchyan, R. G. " A study of phase equilibria at low temperatures by infrared spectroscopy. 2: Diecetylene and acetylene homologues in liquid argon". *Zhur. Fiz. Khim.* **1974**, *48*, 2678-2679.

178. Nyaupane, P. R.; Diez-y-Riega, H.; Cordier, D.; Manzanares, C. E., C–H Absorption and Solubility of Ethylene, Propyne, 2-methyl-2-butene, and 2-methyl-1, 3-butadiene (Isoprene) in Liquid Argon Solutions. *Appl. Spectrosc.* **2017**, 0003702817702387.